Investigation of the coarse grained heat-affected zone microstructure and hardness of multipass welded X65 linepipe steel

by

Wilco Zuidema

to obtain the degree of Master of Science in Materials Science and Engineering
at the Delft University of Technology,
to be defended on Thursday September 17, 2015 at 14:00 PM.

Student number:	4334019	
Project duration:	December 1, 2014 – September 17, 2015	
Thesis committee:	Prof. dr. ir. L. A. I. Kestens,	TU Delft, supervisor
	Dr. ir. M. J. M. Hermans,	TU Delft
	Dr. A. J. Böttger,	TU Delft
	Dr. ir. B. Hu	Allseas Engineering

This thesis is confidential and cannot be made public until September 10, 2016.

TU Delft Delft University of Technology

Allseas

[This page intentionally left blank]

Abstract

In this thesis the effect of single and multipass welding on the microstructure and hardness of X65 linepipe steel of four different chemical compositions was investigated. The welding was simulated for three different heat inputs and two second pass peak temperatures. The thermal simulation has been achieved by simulating the CGHAZ with a Gleeble® thermal-mechanical simulator, peak temperatures used for this simulation were derived from dilatometer experiments. Significant overheating of 50 °C above Ac1 was observed at high heating rates, comparable heating rates of welding. The peak temperature of the first weld cycle was 1350 °C and the second cycle either 810 °C or 860 °C. The overall hardness of the samples was measured as was the micro hardness of M-A constituents. The microhardness of M-A constituents was found to be significantly lower than in previous research, 310 Hv versus 800 Hv. The hardness of the single pass CGHAZ was parametrized for the cooling rate and the chemical composition with an R^2 value 0.98. The parametrization shows increased hardenability due to increased Ni content. The CGHAZ microstructures were examined by optical and scanning electron microscopy as well as EBSD, revealing microstructures consisting of martensite, lower bainite, upper bainite, granular bainite, acicular ferrite and M-A constituents. A number of samples were quantitatively described by use of the IQ distribution from EBSD measurements and the M-A constituents were quantified by Lepera's etchant for all multipass welded samples. A fraction of M-A constituents was found to be higher than 1.6 %all reheated CGHAZ samples and the fraction is found to be dependent on the heat input and hardenability of the steel. It was found that Lepera's etchant reveals a higher fraction of M-A constituents than what is observed by EBSD measurements. The M-A constituents as revealed by Lepera's etchant were found to not completely consist martensite and austenite in the steels considered in this research. Therefore the M-A constituents are suspected to be of less importance for the fracture toughness than discussed in previous research.

Acknowledgements

First of all I would like to thank the supervisors of my gratuation project. First of all Bin Hu for assigning this project to me, his ideas and our weekly talks about the progess of my work and Prof. Kestens for his scientific guidance, support and help with my thesis writing. Furthermore I would like to thank Allseas engineering and especially the innovation department for giving me the opportunity to work on this project.

For the experimental work I have performed I would like to thank Sander van Asperen for his help with metallography, Sepideh Ghodrat and Ghadi Pirgazi for their help with the EBSD measurements, Hans Hofman for his guidance in the use of the Gleeble and Nico Geerlofs for the performing of the dilatometer experiments. Furthermore I would like to thank Liang for his help with the finite element simulations and Hans Drop for teaching me how to machine my own samples.

During my work I had great help from my fellow students sharing the same office, whom pleasantly distracted me from the sometimes stressful activity of thesis writing, which I would like to thank them for. An honourable mention goes out to Ewout, whom profided me with much needed coffee by bringing his very own coffee machine to the office.

Nomenclature

AF	Acicular Ferrite
API	American Petroleum Institute
B_s	Bainite transformation start temperature
BF	Bainitic Ferrite
CCT	Continuous Cooling Transformation
CGHAZ	Coarse Grained Heat Affected zone
CI	Confidence Index
CR	Cooling Rate
EBSD	Electron Backscatter Diffraction
EBSP	Electron Backscatter Pattern
F	Ferrite
FGHAZ	Fine Grained Heat Affected Zone
GB	Granular bainite
GF	Granular Bainitic Ferrite
GMAW	Gas Metal Arc Welding
hagb	high angle grain boundaries
HAZ	Heat Affected Zone
HHI	High Heat Input
HI	Heat Input
HR	heating rate
HSLA	High Strength Low Alloy
IC SGHAZ	Intercritical Coarse Grained Heat Affected Zone
IHAZ	Intercrittical
IHI	Intermediate Heat Input
IQ	Image Quality
K-S	Kurdjumov-Sachs
lagb	low angle grain boundaries
LB	Lower Bainite
LHI	Low Heat Input
LM	Lath Martensite
M	Martensite
M-A	Martensite-Austenite (or martensitic-austenitic) constituents
MF	Massive Ferrite
N-W	Nishiyama-Wasserman

P	Pearlite
PF	Polygonal Ferrite
PT1	Peak temperate first cycle
PT2	Peak temperature second cycle
QT	Quenced and Tempered
S CGHAZ	Sub Critical Coarse Grained Heat Affected Zone
SAWL	Longitudinally submerged arc welded
SC CGHAZ	Super Critical Coarse Grained Heat Affected Zone
SMLS	Seamless
SMYS	Specified Minimum Yield Stress
TMCP	Thermo-Mechanical Controlled-Process
TSAW	Tandem Submerged Arc Welding
U CSHAZ	Unaltered Coarse Grained Heat Affected Zone
UOE	U-ing O-ing and Expading
UTS	Ultimate Tensile Strenght
YS	Yield Strenght

α	BCC ferrite
α'	BCT ferrite (martensite)
γ	FCC ferrite (austenite)
$\Delta t_{8/5}$	Cooling time between 800 °Cand 500 degrees
η	Weld efficiency
θ	Misorientation angle
Ac1	Austenite transformation start temperature
Ac2	Curie temperature
Ac3	Austenite transformation end temperature
d	Average indent diameter
H_b	Hardness of bainite
H_m	Hardness of martensite
H_{fp}	Hardness of polygonal ferrite
I	Weld current
M_s	Martensite transformation start temperature
P	Applied load for Vickers Hardness measurement
U	Weld voltage
v	Weld speed

Contents

Chapter 1

Introduction

Allseas Engineering is an offshore company specialized in pipe-laying, especially the s-lay system. These pipes are used to transport oil or gas from production platforms to either onshore or offshore processing facilities. In order to lay long pipes on the floor of a sea or ocean using the s-lay pipe-lay technique, multiple sections (40 ft or 12 m long) of steel pipes are welded together.

The pipes are made of high-strength low-alloy steel and graded according to the API 5L standard[1] and contain a carbon content which normally does not exceed 0.1 wt%. This steel is used because of its relatively high strength but good weldability.

Pipelines are welded using a multi-pass welding technique. During this welding, multiple welds are used to connect the smaller pipe segments. The number of weld cycles can be upwards of 10 but as low as two. These multiple welds cause the material in the heat-affected zone of the weld (HAZ) to go through several successive heating and cooling cycles. These cycles cause the HAZ to undergo overall changes in the microstructure, which will in turn cause a change in mechanical behaviour of the material[2].

At Allseas engineering it has been found that for some welding procedures and chemical compositions of the steel, the heat-affected zone shows a deterioration in fracture toughness. Due to various reasons one might expect this deterioration to occur at low weld heat inputs and relatively high carbon contents in the steel. It is however found that toughness deterioration occurs at high heat inputs and a relatively low carbon content (0.04 wt%). This change in fracture toughness is often related to a hard and brittle phase in the HAZ. In order to understand this degradation in toughness, a clear understanding of the HAZ microstructure must thus be in place.

In this thesis the temperature cycle of the HAZ will be physically simulated for three different weld heat inputs, after which the microstructure is investi-

gated using optical microscopy, electron microscopy and electron backscatter diffraction (EBSD). The goal is to describe the microstructures of the simulated HAZ and relate this to the hardness of the HAZ.

In the following chapters the theoretical background and the relevant research will be discussed, the methods used will be explained, the results will be shown and discussed and conclusions will be drawn.

Chapter 2

Background and literature review

2.1 Line pipe steel and steel production

Pipelines for offshore use are produced by multiple different processes, of which two will be discussed in this thesis, longitudinally submerged arc-welded pipes (SAWL) and seamless pipes (SMLS). The steel from which pipelines are made is often called linepipe steel.

The steel for SAWL pipes is produced by a thermo-mechanical controlled-process (TMCP), which is a hot rolling process in which the temperature of the steel and the deformation are precisely controlled in order to achieve the desired mechanical properties. SAWL pipes are produced by bending the plate of steel into a pipe, after which the longitudinal ends of the plate are welded together. A last step expands the pipe with hydrostatic pressure to guarantee a smooth shape. This process is illustrated in figure 2.1. Seamless pipes are hot formed from ingots,blooms or billets of steel (pierce rolled) and thus no welding is taking place to form the pipe. After pierce rolling, the pipes are quenched and tempered (QT). The QT process concerns a heating step into the austenitic phase after which it is first quenched using oil, water, brine, a cooling gas or using another cooling medium and subsequently tempered at an elevated temperature. The QT process is used because a TMCP process cannot be applied when the steel is pierce rolled. This makes the production process significantly different from that of SAWL pipes resulting in a different final microstructure and the need for a different chemical composition.

A standard generally used for the specification of linepipe steel is the standard created by the American Petroleum Institute (API) which is designated API 5l. The linepipe steel is designated according to its minimum specified yield strength in ksi, X52 thus stand for a line pipe steel with a specified minimum

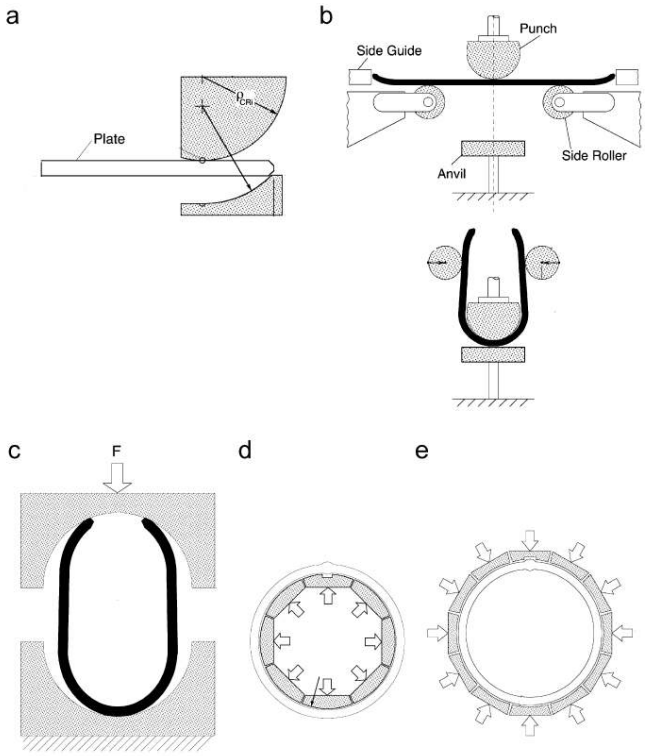

Figure 2.1: Schematic overview of UOE pipeline production [3]

yield strength (SMYS) of 52 ksi (358 MPa). The yield strength and ultimate tensile strength requirements according to the API 5l standard are shown in table 2.1.

Grade	Min. YS (MPa)	Max. YS (MPa)	Min. UTS (MPa)	Max. UTS (MPa)
X65	448	600	531	758
X70	483	621	565	758
X80	552	690	621	827

Table 2.1: Mechanical properties for line pipe steels as specified by API 5L. "Min/Max. YS" = Minumum/Maximum Yield Strenght, "Min/Max UTS" = Minimum/Maximum Ultimate Tensile Strength

2.2 Chemical composition of linepipe steel

In the past (several decades ago) plain carbon steel were used for linepipe, which are of a low carbon content up to 0.3 wt% and have a yield strength ranging from 207 to 358 MPa (30 to 52 ksi).[4].

In order to achieve higher strengths of the linepipe steel, microalloying is applied. These steels are denoted as High-Strength Low-Alloy (HSLA) steels. Table 2.2 shows the maximum alloying elements of HSLA linepipe steels according to the API 5l standard[1].

Table 2.2: Maximum alloying contents in wt% according the the API 5L specification for linepipe steels of different grades and manufacturing processes. (a) The sum of V, Nb and Ti may not exceed 0.15 wt% (b) For a reduction of 0.01 wt% of carbon content, an increase of 0.05 wt% above the maximum specified Mn content is allowed. With a maximum of 1.65 wt% for grades between X56 to X65 and a maximum of 2.00 wt% for X70 grade steel.

Manufacturing process	Grade	C	Mn$^{(b)}$	P	S	Ti	Other
Welded	X56,X60	0.26	1.40	0.030	0.030	0.04	(a)
	X65	0.26	1.45	0.030	0.030	0.06	(a)
	X70	0.26	1.65	0.030	0.030	0.06	(a)
Seamless	X56,X60,X65	0.28	1.40	0.030	0.030	0.04	(a)
	X70	0.28	1.40	0.030	0.030	0.06	(a)

Additionally, the standard by certification body DNV provides extra limitations to the chemical composition of the steel depending on the pipe manufacturing process, which is shown in table 2.3. Where the process is denoted as N for normalised pipes, Q for quenched and tempered, and M for thermomechanical rolled or formed. As well as the maximum values shown in table 2.3, the Cu, Cr, Ni, and Mo content must not exceed 0.5 wt% and the B content must not exceed 0.0005 wt %.

Table 2.3: Maximum wt% of alloying alloying elements as prescribed by the DNV-OS-F101 certification[5].

Grade	C	Si	Mn	P	S	V	Nb	Ti	other
X65 (N,Q)	0.16	0.45	1.65	0.020	0.010	0.09	0.05	0.06	*
X65 (M)	0.12	0.45	1.65	0.020	0.010	0.08	0.08	0.06	*

2.2.1 Alloying elements

The effect of (micro)alloying with certain elements is shown in table 2.4. [6] [7].Sage [4] made a clear overview of some of the alloying elements in table 2.4 when used for linepipe steel. This overview is shown in figure 2.2.

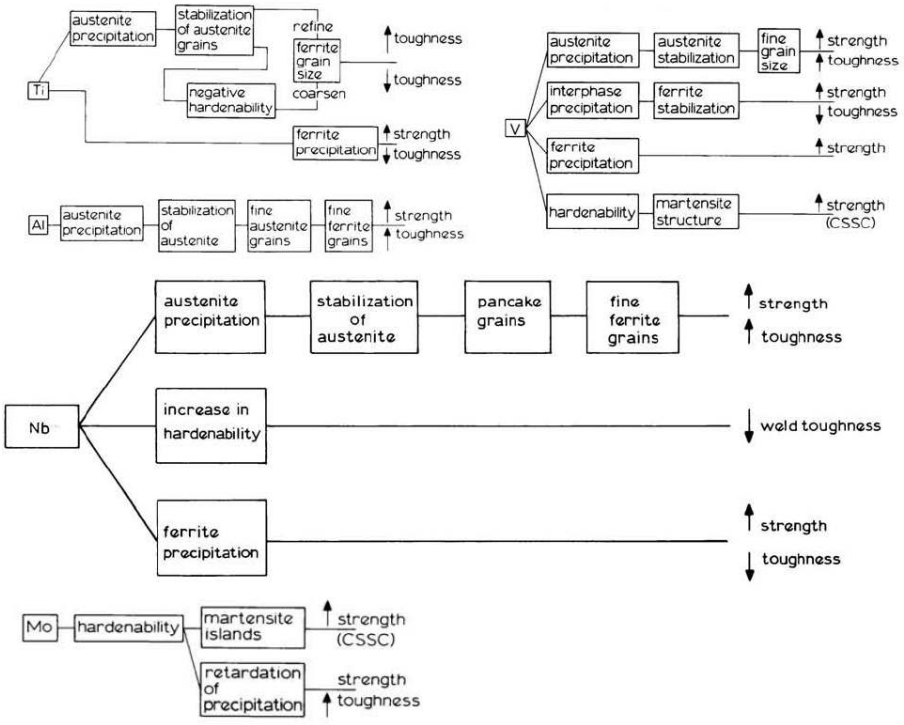

Figure 2.2: The effect of alloying elements on line pipe steels as discussed by Sage [4]

2.2.2 Through thickness change in linepipe chemical composition and microstructure

During plate and pipeline production several processes take place which change the microstructure and chemical composition of the linepipe steel in the thickness direction. The change in chemical composition in the thickness direction, is called macro segregation and takes place during the solidification of the steel slab, before it is rolled into a plate. One notable segregation is centreline segregation, in which there is an increase in alloying elements along the centreline of the plate [8]. Centreline segregation may take place due to the rejection of solute atoms from the solid during solidification, which is due to the higher solubility in the liquid phase. As the middle of the slab is the last to solidify,

Table 2.4: The effect of alloying elements in steel[6;7].

Element	Effect
Cu	Forms pure copper precipitates, leading to age hardening.
Mn	Lowers pearlite transformation temperature. Forms carbides and MnS. Retards and slows pearlite transformation. Increase solid solution strength and hardenability.
Ni	Lowers the minimum austenitising temperature (equation (2.2)). Forms Ni_3X phases with Mo, Ti and Al leading to precipitation hardening. Retards the pearlite transformation, increasing hardenability. Does not form carbides.
Al	Forms AlN precipitates at grain boundaries. Forms intermetallic compounds. Forms alumina inclusions. Does not form carbides.
Cr	Forms nitrides and carbides. Forms intermetallics including the detrimental sigma phase Improves hardenability.
Mo	Forms carbides Mo_2C, Mo_3Fe_3C and Fe_2MoC Forms intermetallic compounds and stabilizes sigma phase. Highly efficient at improving hardenability at low concentrations. Secondary hardening due to carbide precipitation during tempering.
B	High strengthening effect at very low concentrations (10-30 ppm). Segregates to grain boundaries. Highly improves hardenability Causes intergranular embrittlement in excessive amounts.
Si	Effect small at fractions up to 0.35%. Forms silicon dioxide inclusions during deoxidation of steel.
V	Forms highly stable carbides, nitrides and carbonitrides (MX type). Forms intermetallics and stabalizes sigma phase. High austenizing treatments are required to dissolve secondary carbides. Improves hardenability and generates secondary hardening during tempering. Causes strengthening by grain refinement. Strengthens ferrite by carbide precipitation at low temperatures.
Ti, Nb	Forms highly stable carbides, nitrides and carbonitrides (MX type). Removes carbon from solution. Raises the martensite transformation start temperature. Generates secondary hardening during tempering. Strengthens ferrite by interphase precipitation at low temperatures.

this is the part which contains the most solute atoms, the complete mechanism is somewhat more complex and beyond the scope of this work.

Trough-thickness change in microstructure in a linepipe steel plate is commonly observed and is due to the difference in cooling rate between the center and the edge of the plate or pipe. During a TMCP process, the temperature and cooling rates cannot be uniformly controlled throughout the thickness of the plate, which can cause a gradient in cooling rate.

2.3 $\alpha \rightarrow \gamma$ transformation

This section discusses the transformation from a low temperature ferrite (bcc) or martensite (bct) phase to austenite (fcc).

When steel is heated from room temperature, or any other temperature below Ac1 it starts to transform from the low temperature phase (either bcc ferrite or bct martensite) to austenite at temperature Ac1. The transformation is complete at the temperature Ac3, where the steel is fully austenitic. The temperatures are defined as in figure 2.3, which shows the iron-carbon phase diagram. Several empirical formulas have been suggested in order to calculate Ac1 and Ac3, Andrews[9] found the equations most cited in literature:

$$A_1(^\circ\mathrm{C}) = 723 - 10.7Mn - 3.9Ni + 29Si + 16.7Cr + 290As + 6.38W \quad (2.1)$$

$$A_3(^\circ\mathrm{C}) = 910 - 230C^{0.5} - 15.2Ni + 44.7Si + 104V + 31.5Mo + 13.1W \quad (2.2)$$

These temperatures are applicable only for systems in equilibrium and in reality will be dependent on heating rate. The heating rate in welding may be upwards of 500 °C/s, which can certainly not be considered an equilibrium situation. At high heating rates, significant overheat may occur and the transformation from ferrite to austenite is shifted to a higher temperature.

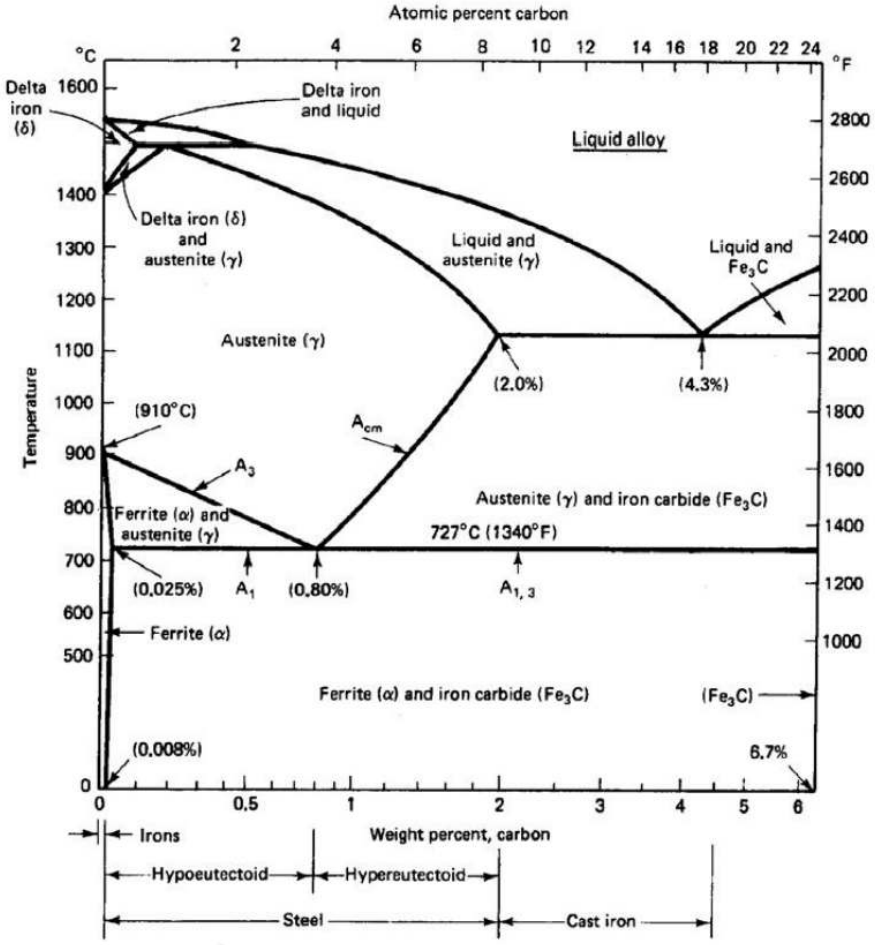

Figure 2.3: Iron-Carbon phase diagram adapted from Pollack[10]

2.4 $\gamma \rightarrow \alpha$ transformation

This section discusses the transformation from austenite to the different microstructures upon cooling, which is dependent on cooling rate, austenite grain size and chemical composition.

2.4.1 Orientation relationships.

When the transformation from austenite to ferrite is considered, two mechanisms of transformation are often distinguished, a displacive mechanism (or military) and a diffusive mechanism (or civilian). As the name suggests, a

diffusive mechanism involves the diffusion of solute atoms over relatively large distances, where a displacive transformation entails a minimum movement of solute atoms. When a displacive transformation occurs from austenite (γ) to the bcc or bct phase (α or α'), an orientation relation is present between the austenite and the transformation product. Bain and Dunkirk[11] have proposed a displacive transformation mechanism from austenite to martensite, which is now called the Bain transformation. An overview of this mechanism is shown in figure 2.4. The overall result of this transformation is that the unit cell is contracted 20 % in the z direction and expanded by 12 % in the x and y directions. This transformation concerns minimum atom movements and the deformation in the unit cell results in the following relationships between crystal directions in the two phases, which can easily be seen in figure 2.4:

$$(111)_\gamma \rightarrow (011)_{\alpha'}$$

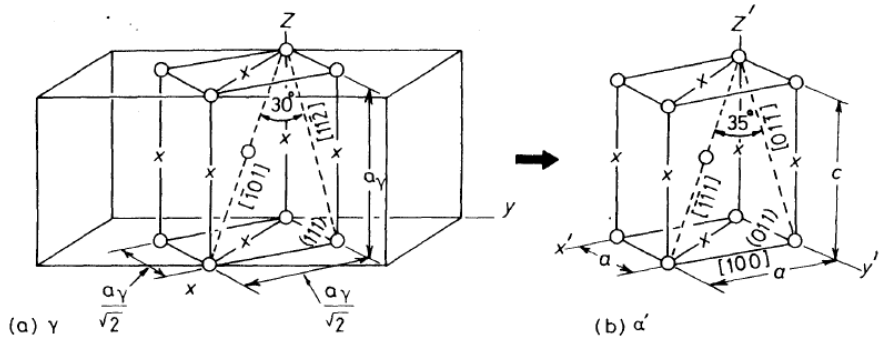

Figure 2.4: The transformation mechanism as proposed by Bain and Dunkirk[11]. Figure adapted from Porter et al.[12].(a) Two fcc γ unit cells with the part relevant for the Bain transformation highlighted. (b) The bct α' phase.

This transformation corresponds to a 45° rotation about the $< 001 >$ axis. Table 2.5 lists more precise orientation relationships which have been found in steels[6], which are slight adjustments of the bain relation (section 2.4.1) and are called Kurdjumov-Sachs (K-S) and Nishiyama–Wasserman (N-W). Because of this relation between fcc and bcc, there will also be an orientation relationship between the bcc orientations. These relationships are shown as axis angle pairs in table 2.6[13].

2.4.2 Transformation mechanisms.

Depending on the cooling rate and chemical composition the transformation from austenite to ferrite exhibits different mechanisms. At low cooling rates, the carbon has time to diffuse from the austenite to separate areas of cementite,

Table 2.5: Orientation relations between γ and α.

Name	Orientation relation between crystal directions	Orientation relation between crystal planes	Axis angle pair
Kurdjumov-Sachs (K-S)	$(111)_\gamma \parallel (001)_{\alpha'}$	$[0\bar{1}\bar{1}]_\gamma \parallel [1\bar{1}\bar{1}]_{\alpha'}$	$< 112 > 90$ °
Nishiyama–Wasserman (N–W)	$(111)_\gamma \parallel (101)_{\alpha'}$	$[1\bar{2}1]_\gamma \parallel [10\bar{1}]_{\alpha'}$	$< 362 > 95.3$ °

Table 2.6: Axis angle pair orientation relationships between ferrite grains transformed from one austenite grain. Tables adapted from Landheer [13]

Kurdjumov-Sachs (K-S)

Angle (°)	U	V	W	Angle (°)	U	V	W
10.5	1	1	0	49.5	1	-1	1
10.5	-1	1	-1	50.5	11	-12	18
14.9	6	1	16	50.5	-5	20	16
20.6	-11	-6	11	51.7	-6	11	11
20.6	0	-5	16	57.2	20	-17	10
21.1	-9	0	20	57.2	17	20	7
47.1	7	-15	17	60	1	1	0
49.5	1	1	0	60	1	-1	1

Nishiyama–Wasserman (N-W)

Angle (°)	U	V	W
13.8	1	12	12
19.5	0	0	1
50.0	-17	13	-17
53.7	-18	-19	6
60	1	1	0

which is visible in pearlite (section 2.5.2). Pearlite will nucleate on austenite grain boundaries and if the pearlite growth starts with the formation of ferrite, this will have the N-W orientation relation with one of the austenite grains. If the nucleation starts with the formation of cementite, the cementite will also have a specific orientation relation with one of the austenite grains. The pearlite will grow into the austenite grains surrounding the nucleation site. [6] [12]. In low carbon steels, at a sufficiently low cooling rate, the carbon will diffuse from the austenite into pearlite regions or separate cementite areas and the remaining austenite will transform to polygonal ferrite.

Bainitic ferrite is formed by a displacive transformation from austenite. Bainite nucleates on the austenite grain boundaries and grows into one of the two austenite grains and has the K-S or N-W orientation relation with the austenite

grain in which it grows. Inspection of the transformed surface shows the transformation is accompanied by a strain in the lattice, which suggests a displacive transformation. The rate of transformation is however determined by the diffusion rate of carbon. It has been found that acicular ferrite also has the K-S orientation relation with the parent austenite.[12] [14].

Martensite is formed at higher cooling rates than bainite and concerns a displacive transformation from austenite to martensite. No redistribution of solute atoms takes place during this transformations, the local chemical composition of the martensite is thus the same as that of the parent austenite. Due to the completely displacive nature, martensite transformation is very fast with speeds up to 1100 m/s[12].

Both bainite and martensite laths are grouped into blocks, which have the same or nearly the same orientation. And the blocks grouped into packets, which have the same orientation relation with austenite[15].

2.4.3 Transformation start temperature

The highest temperature at which the formation of a certain microstructural constituent can take place, when cooled from austenite, is called the transformation start temperature. In this section some variables controlling the transformation start temperature of bainite and martensite will be discussed.

Austenite grain size

As the prior austenite grain boundaries often are a nucleation point for various microstructural features, the austenite grain size is of great influence on the microstructure after cooling[16]. The austenite grain growth is dependent on alloying elements, as precipitates and solid solution atoms exert a drag (Zener drag) on the the grain boundary movement and slow down the grain growth[17].

For steel containing $0.15 <$ wt% C < 0.41 Lee and Lee[18] proposed an Arrhenius type equation (equation (2.3)) for the austenite grain growth with different amounts of Ni, Cr and Mo (in micrometer and the concentrations in weight percent). This was however not correlated for low austenizing times and low carbon contents.

$$d = 76671 \exp\left(\frac{-89089 + 3581C + 1211Ni + 1443C + 4031Mo}{RT}\right) t^{0.211} \quad (2.3)$$

Martensite transformation start temperature

The starting temperature of martensite tranformation is found to be depend on the prior austenite grain size and chemical composition.

Andrews[19] found an empirical formula for the martensite start temperature depending on the chemical composition (in wt%) of the steel:

$$M_s(^\circ\mathrm{C}) = 539 - 453C + 15Cr - 16.9Ni - 9.5Mo + 217C^2 - 715(C)(Mn) - 67.6(C)(Cr) \tag{2.4}$$

Yang and Bhadeshia[20] found a relation between the martensite-start temperature and the austenite grain size:

$$M_s^0 - T = \frac{1}{b} \ln \left[\frac{1}{\alpha V_\gamma} \left\{ \exp - \frac{\ln(1-f)}{m} - 1 \right\} + 1 \right] \tag{2.5}$$

Where a and b are fitting parameters, and in the case of the steels considered in this paper were found to be 1.57×10^{-21} μm^3 and 0.253 respectively. M_s^0 is the martensite start temperature for infinite austenite grain size, f is the fraction of martensite, m is the aspect ratio of martensite plates and V_γ is the average volume of the austenite grains. It can be seen that the martensite transformation start temperature increases with smaller austenite grain size.

Bainite start temperature

Lee[21] proposed an empirical formula for the bainite formation start temperature dependent on the chemical composition (equation (2.6)). In the determination of this formula however, the typical content of carbon and other alloying elements of linepipe steels were not considered. The bainite transformation start temperature found, using this formula, for the X65 steel discussed by Davis and King[22] (section 2.8.2) is 626 °C, which does seem reasonable when compared to other literature[14].

$$B_s(^\circ\mathrm{C}) = 745 - 110C - 59Mn - 39Ni - 68Cr - 106Mo + 17MnNi + 6Cr^2 + 29Mo^2 \tag{2.6}$$

2.5 Microstructure nomenclature

Different microstructure descriptions haven been suggested over time and this has been subject of debate, the goal of this section is to give an overview of the appearance of microstructures found in low carbon steels as described by several sources. After this overview, a nomenclature choice will be made for this thesis.

2.5.1 Polygonal, Equiaxed, Polyhedral or Primary Ferrite

When the cooling rate is lowest and at the highest temperatures (above 650 °C), polygonal ferrite is formed, which is dubbed Primary Ferrite by the International Institute of Welding (IIW). The IIW makes a distinction between the ferrite which nucleates on the austenite grain boundaries or on inclusions in the interior of the grain. These Ferrites are identified by a very low dislocation density and the absence of substructures. On the scale of a light microscope, the grain boundaries look smooth and continuous. When the material is not fully transformed to ferrite, the ferrites give an outline of the prior austenite grain boundaries. A typical micrograph of this microstructure is shown in figure 2.5. [23] [24] [25].

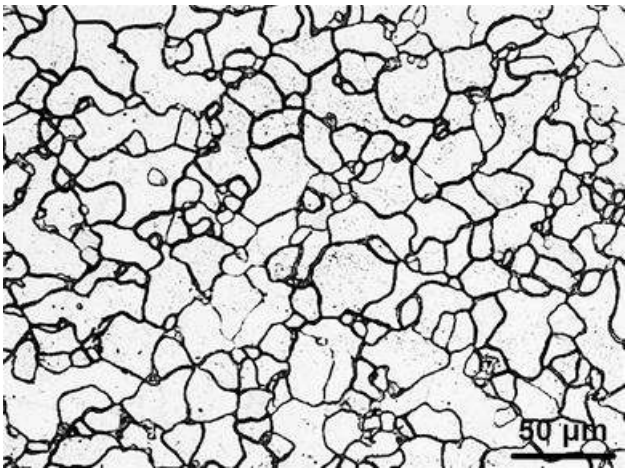

Figure 2.5: An optical micrograph of Polygonal, Equiaxed, Polyhedral or Primary Ferrite. Figure taken from Sun et al. [26]

2.5.2 Pearlite

Pearlite is composed of colonies of laminar regions of alternating cementite and ferrite. The transformation usually starts at austenite grain boundaries or at inclusions. The lamellae can be so tightly spaced that they are indistinguishable under a light microscope, in this case electron microscopy is necessary in order observe the lamellae. [23]. A typical micrograph of this microstructure is shown in figure 2.6.

2.5.3 Widmanstätten Ferrite or Ferrite side plate

Widmanstätten Ferrite or ferrite side plate consists of coarse elongated crystals of ferrite, and appears white when etched with nital, with no evidence of substructures. Widmanstätten Ferrite can either grow from austenite grain bound-

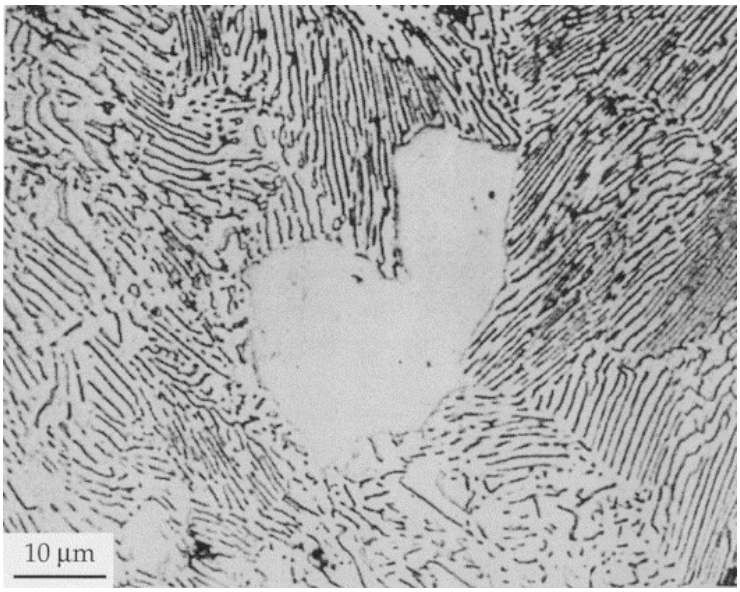

Figure 2.6: A optical micrograph of pearlite surrounding a recrystalized austenite grain. Figure taken from Jacot et al.[27]

aries or inclusions, which is called primary Widmanstätten Ferrite or from other ferrites, which is called secondary Widmanstätten Ferrite. The ferrite plates are usually of a high aspect ratio (∼10:1) in parallel arrays[23] [24]. A typical micrograph of this microstructure is shown in figure 2.7.

Figure 2.7: A optical micrograph of widmanstätten ferrite (elongated white grains). Figure taken from Krauss and Thompson[24]

2.5.4 Quasi Polygonal ferrite or Massive ferrite

At large enough cooling rates, when the austenite cannot be transformed to polygonal ferrite, it is possible to form grains of ferrite directly from austenite grains with the same composition. Quasi polygonal ferrite differs from polygonal ferrite in that it consists of smaller crystals, curved high angle grain boundaries, a substructure of slightly disoriented blocks and a higher dislocation density. Quasi polygonal ferrite has also been shown to sometimes contain Martensite-Austenite (M-A) constituents (discussed in section 2.7.4). Note that this microstructure is not mentioned by the IIW[25] [24]. A typical micrograph of this microstructure is shown in figure 2.8.

Figure 2.8: A optical micrograph of quasi polygonal ferrite. Figure taken from Krauss and Thompson[24]

2.5.5 Acicular ferrite.

According to Matrosov et al.[25], acicular ferrite is sometimes called bainitic ferrite, low carbon bainite, quasi polygonal ferrite or granular bainite and appears as racks or plates of ferrite, not as needles as the name 'acicular' suggests. These plates or racks are found to nucleate on inclusions, within austenite grains (mainly Titanium oxides) or during the solidification of weld metal.[28] [29] [30] [14]. The acicular ferrite as defined here is shown in figure 2.9. For linepipe steels however, a different nomenclature is often used for acicular ferrite. It is defined as a highly substructured non-equiaxed ferrite, formed at a temperature range slightly higher than upper bainite[28] [32] [33] [34]. This definition of acicular ferrite is similar to that of quasi polygonal ferrite discussed in section 2.5.4 an optical micrograph of this microstructure is shown in figure 2.10. Tang and Stumpf[35] found that the microstructure identified by most authors as completely acicular

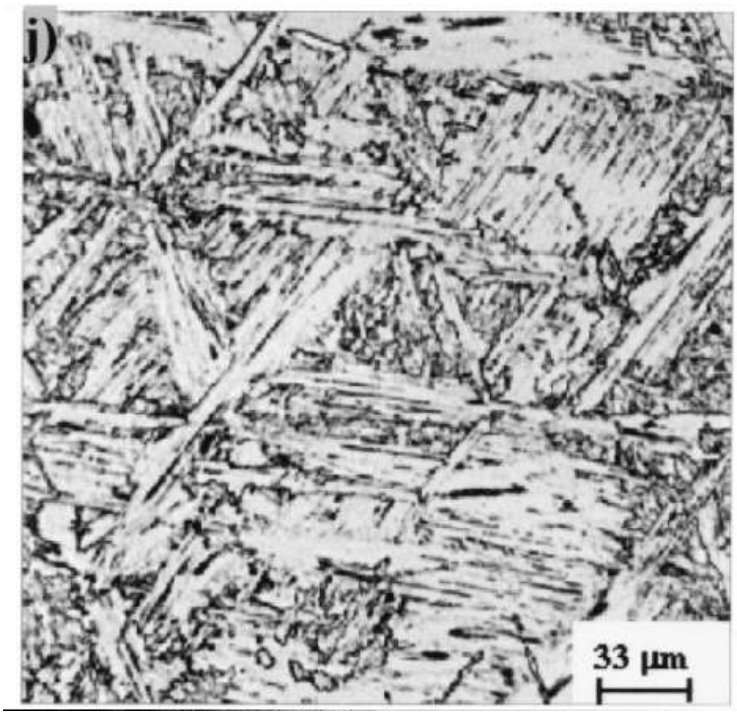

Figure 2.9: A optical micrograph of acicular ferrite. Figure adapted from Diaz-Fuentes et al.[31]

ferrite, is actually a combination of acicular ferrite and polygonal ferrite. This was determined by an apparent etching difference between acicular ferrite and polygonal ferrite. Acicular ferrite is etched more by Nital than polygonal ferrite due to the internal striations and was distinguished from bainite by the absence of carbides within the ferrite.

2.5.6 Bainitic microstructures

The bainite transformation takes place at low temperatures where diffusion is slow and it grows as parallel arrays or sheaves. Two separate microstructures are often distinguished: upper and lower bainite. In upper bainite carbon partitions into the residual austenite during cooling and precipitates as cementite between the bainitic ferrite bundles or sheaves. In lower bainite, the ferrite becomes super saturated with carbon and some carbide precipitation occurs within the bainitic ferrite as well as in between them. The terms "lower" and "upper" are used due to the fact that the transformation temperature of upper bainite is higher than that of lower bainite. Lower bainite thus requires a higher undercooling, which means a higher cooling rate.[6] [14]. A schematic overview of the difference between upper and lower bainite is shown in figure 2.11 and figure 2.12 shows

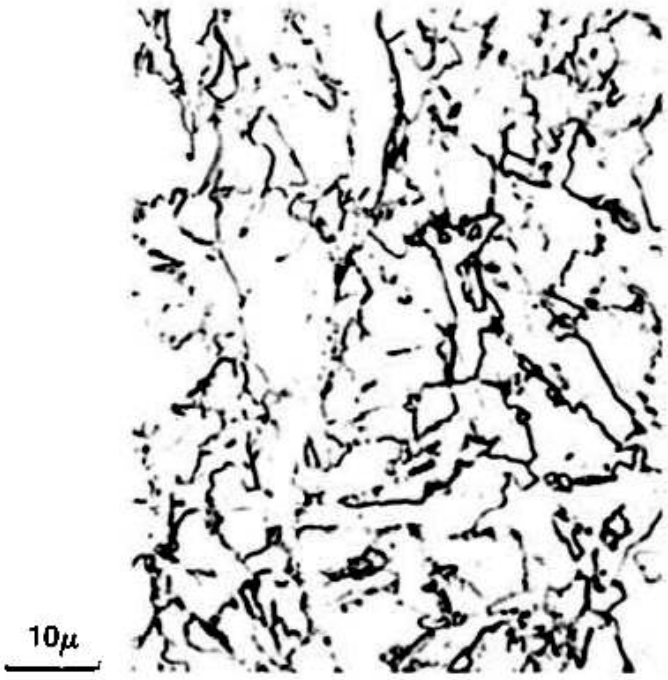

Figure 2.10: A optical micrograph of acicular ferrite. Figure adapted from Coldren and Mihelich[34]

an optical micrograph of upper bainite in linepipe steel.

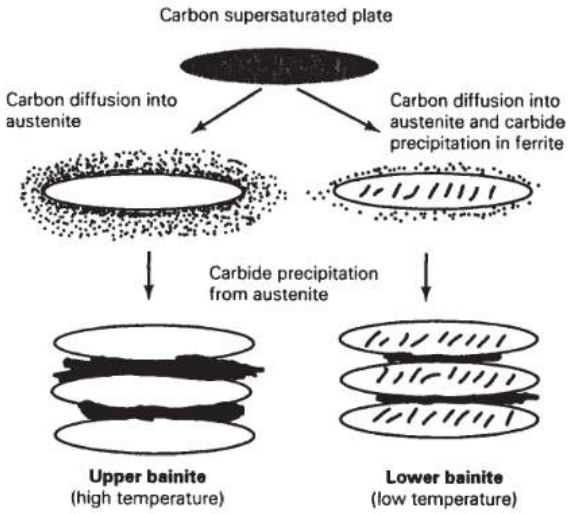

Figure 2.11: A schematic overview of the difference between upper and lower bainite. Figure adapted from Bhadeshia and Honeycombe[14]

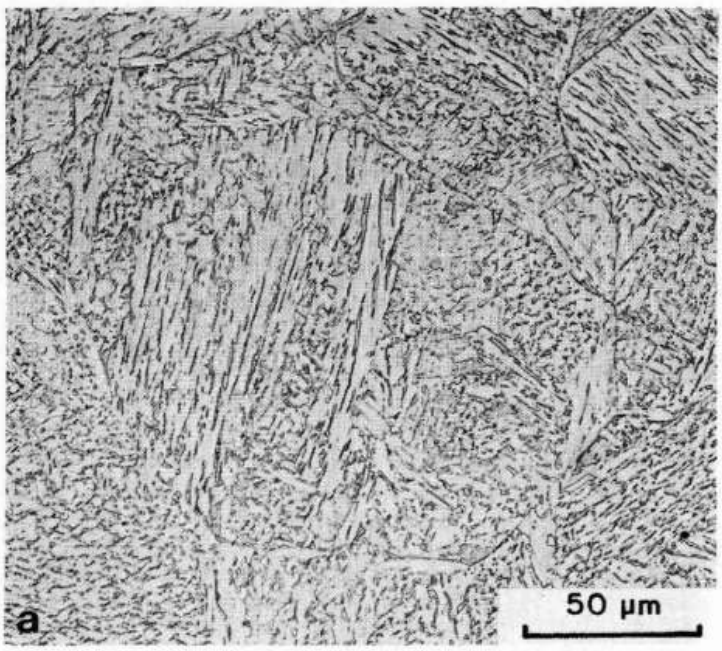

Figure 2.12: A optical micrograph of upper bainite. Figure adapted from Collins et al.[36]

2.5.7 Martensite

When steel is cooled from the austenite phase at a high enough rate, the transformation is completely displacive and the resulting microstructure is called martensite. In low carbon steel the martensite will grow into needles or laths. Martensite is highly substructured and has a high dislocation density (crystal imperfection), making it a hard an potentially brittle microstructure. Martensite is etched by Nital and appears dark [14] [12].

2.5.8 Conclusion

An overview of the microstructures formed at different temperatures and cooling rates is shown in figure 2.13. For this thesis, it is important to choose what nomenclature to use for certain microstructures, especially acicular ferrite as it is used for two notably different morphologies. In this thesis, the non-equiaxed ferrite with rough borders will be called acicular ferrite. An overview of the nomenclature which is chosen, is shown in figure 2.14 which is a nomenclature often used in literature concerning linepipe steel and pipeline welding.

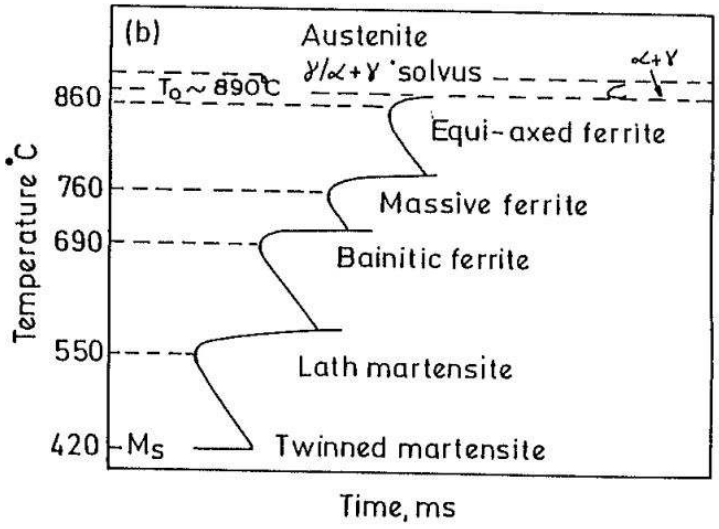

Figure 2.13: A TTT diagram of the some of the microstructures discussed in this section. Taken from Wilson [37]

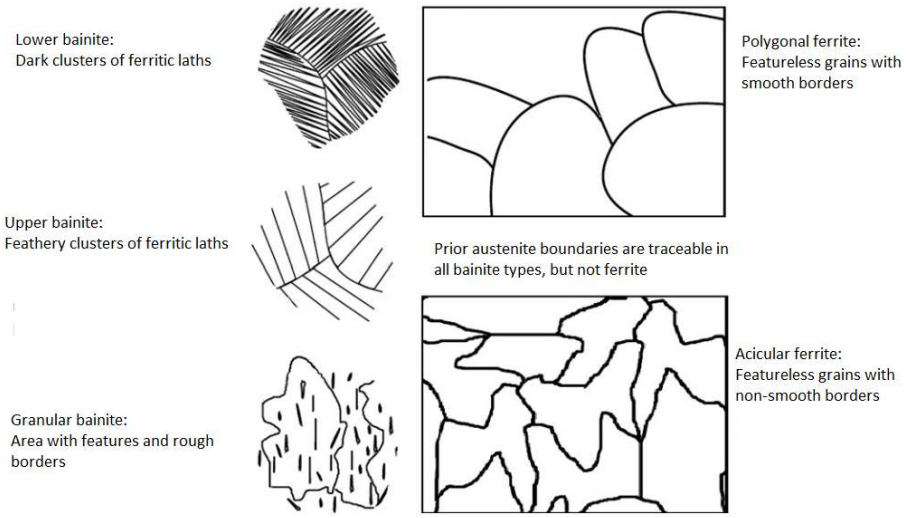

Figure 2.14: An overview of the nomenclature used for the microstructures in this thesis. Figure adapted from Mohammadi et al.[38]

2.6 Hardness

The hardness is often found to be a good parameter for estimating the yield strength and ultimate tensile strength of a material, as well as the possible brittleness. There are several methods for measuring the hardness of steel, the method used in this thesis will be Vickers hardness. Vickers hardness is measured by pressing a pyramid shaped diamond into the material with a known load. Afterwards the size of this indent is measured and this determines the hardness value. A schematic overview of this process is shown in figure 2.15. The Vickers hardness is now expressed as (X) Hv(Y) where (X) is the hardness value given by equation (2.7) and (Y) is the applied load in Kg. For example: 200 Hv1 is a measured Vickers hardness of 200 with a load of 1 Kg.

$$\text{Hv} = 1.8544 \times \frac{P}{d^2} \text{ where } d = \frac{d_1 + d_2}{2} \tag{2.7}$$

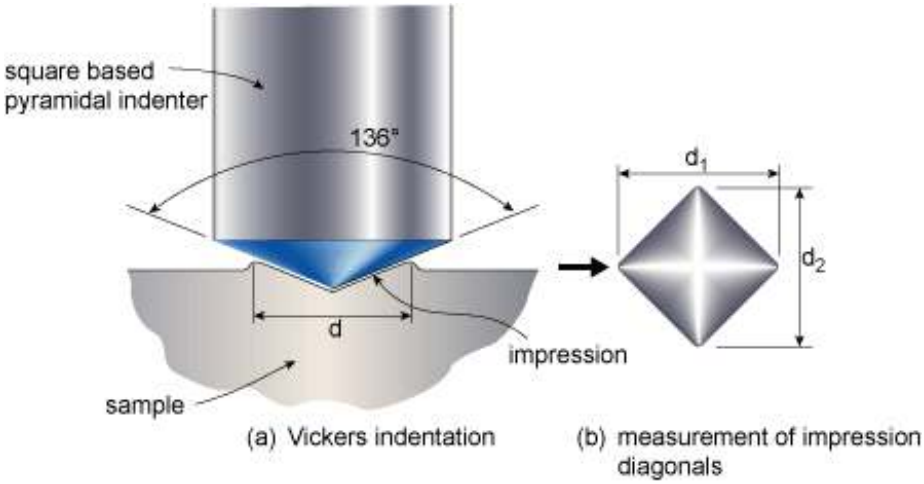

Figure 2.15: Schematic overview of the vickers hardness testing method. Figure adapted from reference [39]

The overall hardness of the HAZ is dependent on the hardness of the microstructural constituents present. Blondeau et al. [40] present formulas for the hardness of microstructural constituents depending on the chemical composition and cooling rate.

$$H_m = 127 + 949C + 27Si + 11Mn + 8Ni + 16Cr + 21 \log V' \tag{2.8a}$$

$$\begin{aligned} H_b = &-323 + 185C + 330Si + 153Mn + 65Ni + 144Cr + 191Mo \\ &+ (98 + 53C - 55Si - 22Mn - 10Ni - 20Cr - 33Mo) \log V' \end{aligned} \tag{2.8b}$$

$$\begin{aligned} H_{fp} = &42 + 223C + 53Si + 30Mn + 12.6Ni + 7Cr + 19Mo \\ &+ (10 - 19Si + 4Ni + 8Cr + 130V) \log V' \end{aligned} \tag{2.8c}$$

Where the Hardness is the Vickers hardness, the composition is in wt% and V' is the cooling rate at 700 ° C. The overall hardness is given by $H = H_m V_m + H_b V_b + H_{fp}$ where H_m, H_b, and H_{fp} are the hardness of the martensitic, bainitic an pearlitic-ferritic constituents and V_m, V_b and V_{fp} their respective volume fraction. Kasuya et al. [41] also gave a equation for the hardness of a fully martensitic steel:

$$\mathrm{H_m} = 884C \times (1 - 0.3C^2) + 294 \tag{2.9}$$

Where H_m is the hardness and C is the carbon content in wt %. Kasuya et al.[41] presented an empirical equation for the hardness of the heat-affected zone (which is discussed in section 2.7.2):

$$HV = 442C + 99CE_{II} + 206 + (402C + 90CE_{II} + 80) \times \arctan(x) \tag{2.10a}$$

$$x = \frac{\log(t_{8/5}) - 2.3CE_I - 1.35CE_{III} + 0.882}{1.15CE_I - 0.673CE_{III} - 0.601} \tag{2.10b}$$

$$CE_I = C + \frac{Si}{24} + \frac{Mn}{6} + \frac{Cu}{15} + \frac{Ni}{12} + \frac{Cr}{8} + \frac{Mo}{7} \tag{2.10c}$$

$$CE_{II} = C + \frac{Si}{24} + \frac{Mn}{5} + \frac{Cu}{10} + \frac{Ni}{18} + \frac{Cr}{5} + \frac{Mo}{2.5} + \frac{V}{3} + \frac{Nb}{5} \tag{2.10d}$$

$$CE_{III} = C + \frac{Mn}{3.6} + \frac{Cu}{20} + \frac{Ni}{9} + \frac{Cr}{5} + \frac{Mo}{4} \tag{2.10e}$$

Where the fractions are in wt%. Nolan et al.[42] suggested an improved empirical equation for the hardness of the heat-affected zone:

$$\text{Pcm} = C + \frac{Si}{30} + \frac{Mn + Cu + Cr}{20} + \frac{Ni}{60} + \frac{Mo}{15} + \frac{V}{10} + 5B \tag{2.11a}$$

$$CE_N = 2P_{cm} - 0.092 \tag{2.11b}$$

$$HV = (-1.3893t_{8/5}^2 + 11.681t_{8/5} + 239.58)\ln(CE_N) + (-2.4286t_{8/5}^2 + 15.543t_{8/5} + 645.6) \tag{2.11c}$$

Where HV is the vickers hardness in the HAZ and $t_{8/5}$ is the cooling time from 800 °C to 500 °C. Hashemi[43] did a statistical correlation between the hardness found in a SAWL API X65 graded pipeline, for the weld metal, heat-affected zone and base metal. The following relations were found:

$$\text{YS} = 2 \times \text{HV} + 105 \tag{2.12}$$

$$\text{UTS} = 1.3 \times \text{HV} + 344 \tag{2.13}$$

Where YS and UTS are the yield strength and ultimate tensile strength of the steel, respectively, and HV is the vickers hardness of the steel when using a 10 kg load. This was correlated for one chemical composition only, which was (wt%) 0.071C, 0.209Si, 1.515Mn, 0.018Cu, 0.011Ni, 0.003Mo, 0.044Nb, 0.042V, 0.017Ti.

To every offshore, subsea pipeline system the Offshore standard DNV-OS-F101 applies, which prescribes maximum hardness values for both the base metal and the HAZ[5]. The maximum allowed hardness of the base metal for an X65 pipeline is 270 HV10 and the maximum allowed hardness in the HAZ zone is 300 HV10. This maximum hardness is given due to the HAZ being more susceptible to cold cracking at higher hardness values[44].

2.7 Pipeline Welding

2.7.1 Welding procedures

In order to lay long pipes (in the order of kilometers) on the sea or ocean floor, smaller sections are welded together. A typical length of these smaller sections is 12.1 m (40 ft.) which means a lot of welds are required in order to span a large distance. Furthermore the pipelines often have a wall thickness of up to 40 mm which causes that pipe sections cannot be welded together using one weld pass. In order to weld the pipes together, multiple weld passes on top of each other are thus needed.

The amount of energy which is used in a certain welding process is expressed in the quantity of heat input. This quantity is defined as:

$$HI = \frac{U \times I}{v} \times \eta \left[\frac{kJ}{mm}\right] \tag{2.14}$$

Where U is the welding voltage, I is the welding current, v is the welding speed an η is the arc efficiency. The arc efficiency is the fraction of the energy of the arc which is not lost due to radiation or convection.

In order to weld pipe sections, Allseas engineering employs two different welding procedures. These processes are a Tandem Submerged Arc Welding (TSAW) process, in which the pipe is rotated under the welding station and a Gas Metal Arc Welding (GMAW) process which is an automated process in which the welding station moves around the pipe.

TSAW is a welding process where the arc is shielded by a layer of shielding powder which works both as flux for the welding process and stops heat from escaping from the weld. This shielding effect makes that an SAW has a high arc efficiency of about 0.95. The TSAW is called double joint welding, as it welds on both the inside and the outside of the pipe with a high heat input. This process is typically of a high heat input (from 1.5 up to 2.5 kJ/mm) and is achieved by using two weld electrodes, hence the name 'tandem'.

GMAW is a welding process in which a gas (a noble gas or nitrogen) is used to shield the weld. Therefore the weld will lose heat due to both convection an radiation, which causes an arc efficiency of around 0.85.

2.7.2 Weld Heat-Affected Zone

Various zones are generally identified in steel welds:

- The fusion zone, in which the molten metals from both the filler wire and the base metal mix.
- The mushy zone, in which the base metal is partly melted.

- The coarse grained heat affected zone (CGHAZ). In this region the metal has not molten but the peak temperature during welding was high enough for the steel to completely austenize and cause significant austenite grain growth, this temperature is usually defined as being greater than 1100 °C.
- The fine grained heat affected zone (FGHAZ). In this region the metal has not molten but the peak temperature during welding was high enough for the steel to completely austenize but no significant grain growth occurs, this peak temperature is usually defined as in between Ac3 and 1100°C.
- The intercritical heat affected zone (IHAZ) In this region the steel has only partially transformed to austenite, in this zone the peak temperature which is reached is between Ac1 and ac3.

An overview of these HAZ regions are shown in figure 2.16.

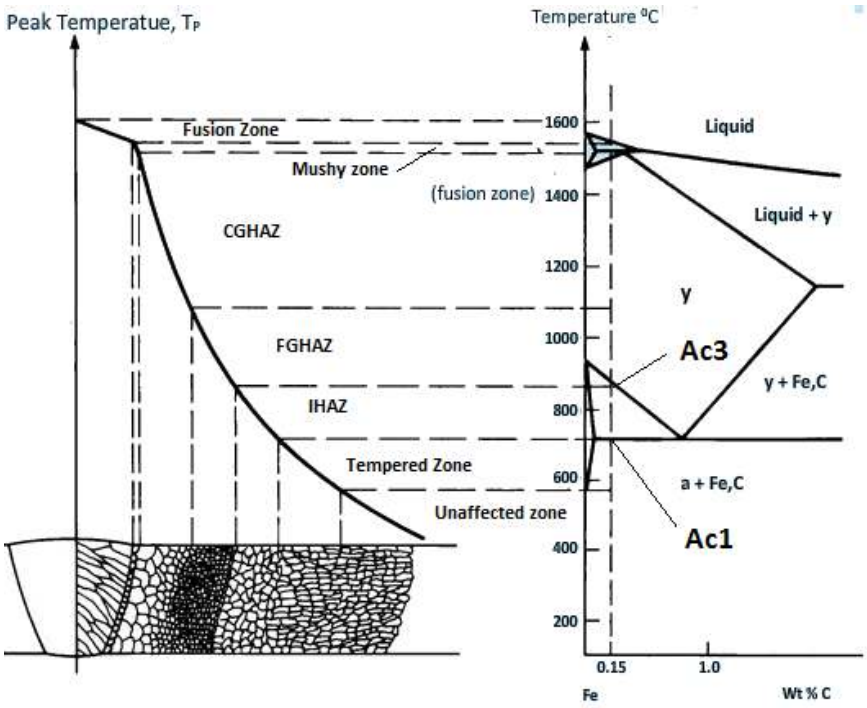

Figure 2.16: An overview of the different HAZ regions of a weld on a steel plate together with the relavent parts of the Iron-Carbon phase diagram, the lines are drawn for a carbon content of 0.15 wt%. Figure adapted from NPTEL[45]

When multipass welding is now considered, extra zones are identified with respect to the CGHAZ:

- The unaltered CGHAZ (U CGHAZ)which has been defined as the zone in which the CGHAZ has been reheated to a temperature above 1100 ˚C.
- The supercritically reheated CGHAZ (SC CGHAZ), which has been defined as the zone in which the CGHAZ has been reheated to a temperature between Ac3 and 1100˚C.
- The intercritically reheated CGHAZ (IC CGHAZ) which has been defined as the zone in which the CGHAZ has been reheated to a temperature between Ac1 and Ac3.
- The subcritically reheated CGHAZ (S CGHAZ) which has been defined as the zone in which the CGHAZ has been reheated to a temperature below Ac1.

A schematic overview of these zones is shown in figure 2.17.

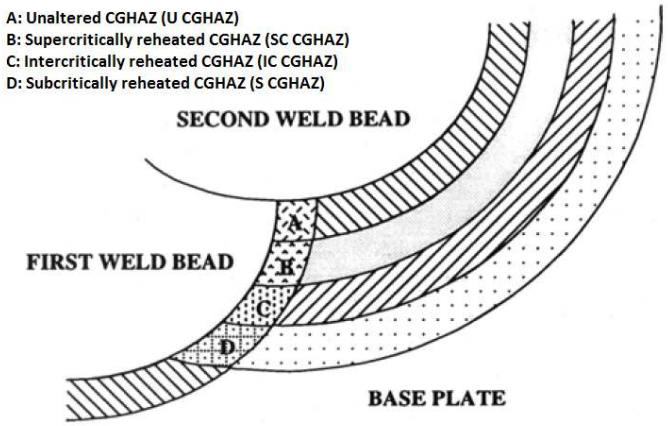

Figure 2.17: Schematic diagram of a multipass weld[46]

2.7.3 Cooling rates in the weld heat affected zone.

In order to perform a proper physical simulation of the weld CGHAZ, the cooling rates need to be known. In previous work the cooling rates in the CGHAZ have often been calculated using theoretical two-dimensional models, which gives quite some spread in cooling rates as illustrated by table 2.7 and is highly dependent on the geometry of the welded parts. Moreover, the cooling rates in the CGHAZ in the second weld cycle is often assumed to be the same as in the first cycle, this is employed by all authors of the papers quoted in table 2.7 except for Hu et al.[47]. All of the papers quoted in table 2.7 have done the research on API 5l graded linepipe steel, but none use a model to predict cooling rates in a pipeline. These facts make it impossible to relate the heat input and geometry considered in this research to the ones in previous research.

Table 2.7: Cooling times and rates according to various sources.

HI (kJ/mm)	$\Delta t_{8/5}$(s)	Cooling rate (°C/s)	Source
0.9	5	60	Li et al.[48]
1	10	30	Shome et al.[49]
1	10	30	Andia et al.[50]
1	20	15	Poole et al.[51]
1.5	20	15	Zhao et al.[2]
2.35	38.5	7.79	Zhu et al.[52]
2.5	13	23	Kiran et al.[53]
2.5	56	5.35	Zhao et al.[2]
2.6	20	15	Hu et al.[47]

The notion that the cooling rate in the HAZ at low temperatures (between 800 and 500 °C)is independent from the distance is confirmed by simulations done by Zhang et al.[54]. Modelling done by Deng and Murakawa[55] and by present writer and Allseas engineering however shows that this is not the case and that the cooling rate in the HAZ will be lower further removed from the weld centreline.

2.7.4 M-A constituents

If the CGHAZ is intercrittically reheated, some partial transformation to austenite takes place, creating reverted austenite (austenite which grows from prior austenite grain boundaries). This reverted austenite has a relatively high carbon content due to the high solubility of carbon in austenite and can transform to martensite or remain present as retained austenite, if the carbon content and cooling rate is high enough. In the case of (locally) a high carbon content, the martensite start temperature can be lower than room temperature and the high temperature austenite will remain as retained austenite. The areas within the matrix consisting of a mixture of Martensite and retained austenite, are often called M-A constituents. The M-A constituents are hard and brittle due to the inherent hardness and brittleness of martensite. The island shaped M-A constituents which form along the prior austenite grain boundaries are often named blocky M-A, where the long lath shaped M-A constituents, called stringer M-A are formed within the prior austenite grains.You et al.[56] used EBSD to investigate an area of reverted austenite by using the K-S orientation relation. It was found that the reverted austenite regions consisted of large areas of bainite and smaller areas of M-A constituents. The fact that the M-A constituents are harder than the surrounding matrix and not uniformly distributed, makes them a candidate for crack initiation[56;57] of which the mechanisms will be discussed in section 2.8.3.Bonnevie et al.[57] found that for X80 linepipe steel the maximum M-A fraction was generated when reheating to A_{c1} + 20-50K.

Mohseni et al.[58] have found that the hardness of the M-A constituents is

within the range of 600-1000 Hv. The carbon content of these constituents was found to be 0.6-1.1 wt % with a cooling rate of 20 °/s. Whereas Li et al.[59] found an average carbon content of 0.75-0.79 wt% at a cooling rate of 15.3 °/s and 6.8 °/s for the first and the second heating cycle, respectively.

The M-A constituents are often revealed by using Lepera's etchant[60], which is a tinting etchant consisting of equal parts of a 1% sodium metabisulfite aqueous solution (sometimes a higher concentration is used) and 4% picric acid dissolved in ethanol. This etchant colours the M-A constituents white, ferrite is coloured tan and bainite appears black. Using this etchant, image analysis can be used more easily to obtain the fraction and morphology of the M-A constituents.

2.8 Previous research

2.8.1 Relation between cooling rate, chemical composition and microstructure.

In the following section multiple continuous cooling transformation diagrams (CCT diagrams) are presented. In these diagrams several abbreviation for microstructures will be used. The meaning of these abbreviations is listed in table 2.8.

There is some uncertainty about the exact definition of various microstructure components. For instance, acicular ferrite can be called granular bainite or quasi-polygonal ferrite. Whereas Xiao et al.[28] consider it to be a mixture of massive ferrite and bainitic ferrite[28] these considerations are discussed in section 2.5.

The resulting microstructure might be dependent on the amount of austenite grain growth, which is not considered in the following sections. In all CCT diagrams, the steel is austenized for an amount of time which is much higher than is to be expected for the welding discussed in this thesis.

Abbreviation	Meaning
BF	Bainitic Ferrite
AF	Acicular Ferrite
MF	Massive Ferrite
PF	Polygonal Ferrite
GF	Granular Bainitic Ferrite
P	Pearlite
M	Martensite
LM	Lath Martensite
GB	Granular Bainite
F	Ferrite
LB	Lower Bainite
M-A	Martensitic Austenitic

Table 2.8: Meaning of abbreviations used in CCT diagrams

The pipeline steels which will be discussed are all of the low carbon type with a carbon content of around 0.05 wt%. Zhao et al.[32] have measured several CCT diagrams for steels with a chemical composition shown in table 2.9, after austenizing at 1100°C for 10 minutes and 950°C for 3 minutes. These diagrams (figure 2.18) show that, depending of the constant cooling rate, the microstructure of the low carbon steels will either transform to a bainitic ferrite, acicular ferrite, polygonal ferrite or pearlitic microstructure. Note that there is no differentiation made between different morphologies of bainite. It was found that steel containing 0.045wt% Carbon, never transformed to a bainitic ferrite microstructure, independent of the cooling rate. In contrast to this, a pipeline steel with composition C from table 2.9 transforms to a bainitic ferrite microstructure for most cooling rates. It is concluded that the alloy additions such as Mn, Nb, Ti and Mo promote the formation of acicular ferrite, which can be concluded for steel A and B but this does not hold for steel C.

Xiao *et al.* did the same an analysis of steel of the same composition as steel C in table 2.9[61]. They found a different microstructure was identified at lower cooling rates, as shown in figure 2.19.

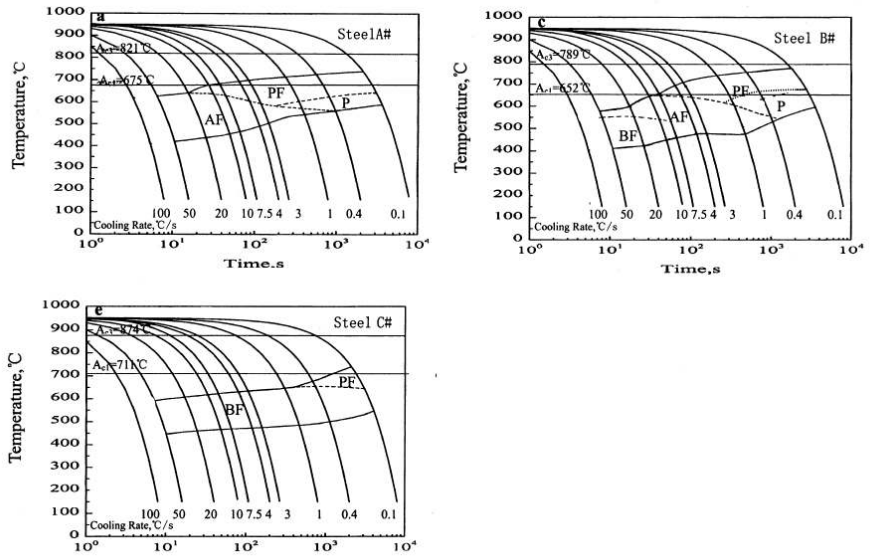

Figure 2.18: CCT diagrams for the different steel compositions shown in table 2.9[32].

Steel	C	Si	Mn	Nb	V	Ti	Mo	O	N
A	0.045	0.3	1.94	-	-	-	-	0.0011	0.003
B	0.077	0.25	1.28	0.045	0.053	0.027	-	0.0011	0.0018
C	0.025	0.24	1.56	0.04	0.02	-	0.32	0.0043	0.0062

Table 2.9: Chemical composition in wt% of the steels considered by Zhao *et al.*[32]

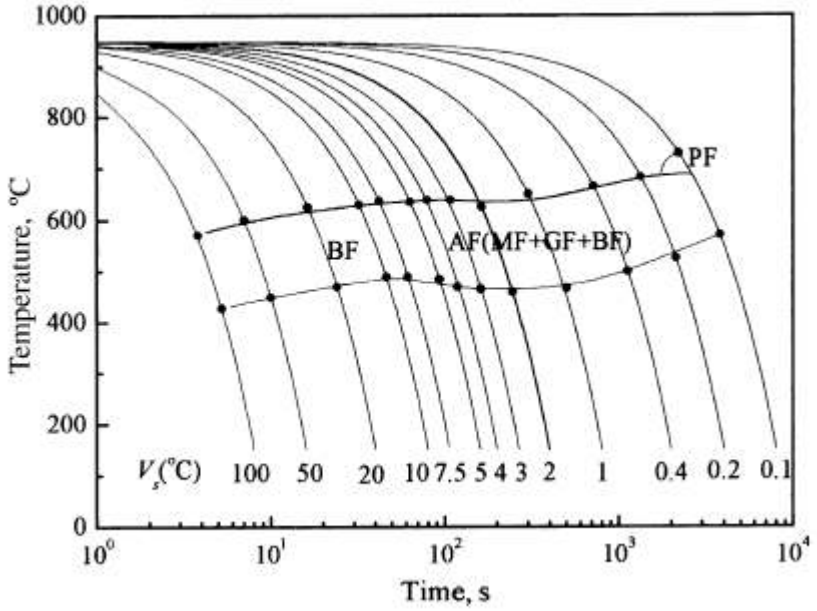

Figure 2.19: CCT diagram of steel of the same composition as steel C shown in table 2.9[61].

Similar measurements were done by Zhang et al.[62] on steel containing significant amounts of Cr (2.1 wt%) and V(0.09 wt%) the results are shown in figure 2.20. Here it was concluded that the addition of Cr and V moves the temperature of austenite to ferrite transformation up to higher temperatures and lowers the bainite transformations start temperature. Zhang *et al.* also found formation of a martensite fraction at cooling rates above 50 °C/s.

C	Si	Mn	P	S	Mo	Cr	V	N	Al
0.048	0.25	1.6	<0.008	< 0.002	0.12	2.1	0.09	0.03	0.02

Table 2.10: Chemical composition in wt% of the steel discussed by Zhang et al.[62].

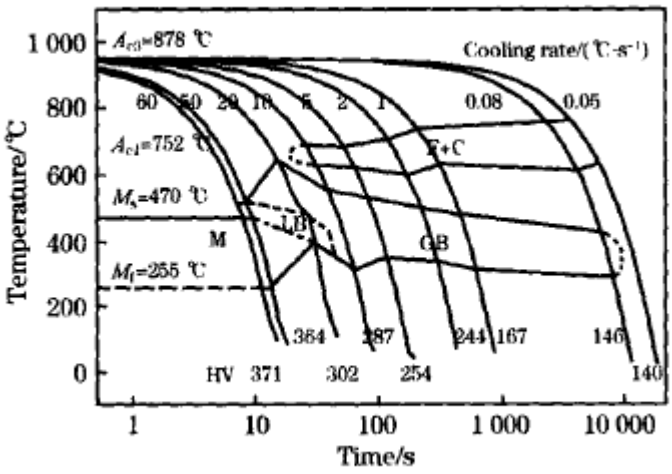

Figure 2.20: CCT diagram for the steel composition shown in table 2.10[62].

Zhang et al.[63] did a microstructural evaluation of steels with the composition shown in table 2.11 for several cooling rates ranging from 2 ˚C/s to 28 ˚C/s . The CCT diagrams found by the same author for the same steel compositions in a different article are shown in figure 2.21. Steel without Nb showed a microstructure dominated by lath bainite and ferrite. The fraction of lath bainite increased with higher cooling rate but no martensite was observed. When a small amount of Nb is added, the primary microstructure is lath and granular bainite with an increasing amount of granular bainite with higher cooling rates. At the highest cooling rate, some lath martensite was observed.

Kong and Qiu[64] also investigated steel with added Nb, they found the CCT diagram shown in figure 2.22 and essentially observed the same microstructures, though different nomenclature is used. It was also found that the hardness decreased as the amount of granular ferrite increased. The maximum hardness was found at the highest cooling rate of about 295 HV.

Steel	C	Si	Mn	Ni+Cr+Mo	V	Nb	Ti
Without Nb	0.073	0.21	1.34	0.37	0.042	-	0.012
With Nb	0.074	0.23	1.41	0.36	0.044	0.026	0.01

Table 2.11: Chemical composition in wt% of the steel discussed by Zhang *et al.*[63]

.

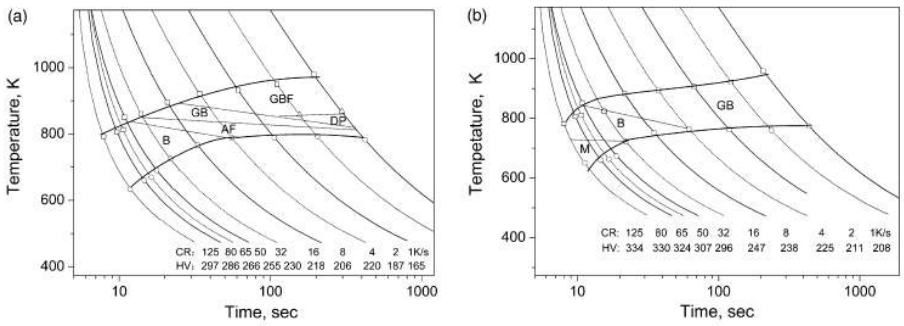

Figure 2.21: CCT diagram for the steel composition shown in table 2.11 [65].

C	Si	Mn	Nb	V	Ti	B	Cr, Mo, Ni
0.053	0.27	1.35	0.027	0.03	0.025	12 $\times 10^{-6}$	0.85

Table 2.12: Chemical composition in wt% of the steel discussed by Kong *et al.* [64]

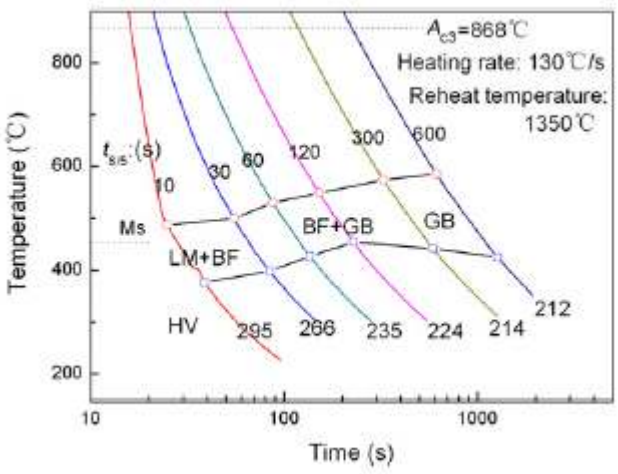

Figure 2.22: CCT diagram for the steel composition shown in table 2.12 [64]

When a very small amount of B is added to the steel (15 ppm) the formation of quasi polygonal ferrite and pearlite is suppressed and the cooling rate for the formation of ferritic bainite is lowered [66]. This effect is shown in figure 2.23 for the steel composition in table 2.13.

Steel	C	Si	Mn	Ti+Nb	Mo+Ni+Cr	N	B
A	0.053	0.25	1.90	0.067	1.1	37	0
B	0.051	0.25	1.92	0.067	1.1	40	15

Table 2.13: Chemical composition in wt% (N and B in ppm) of the steel discussed by Jun *et al.*[66].

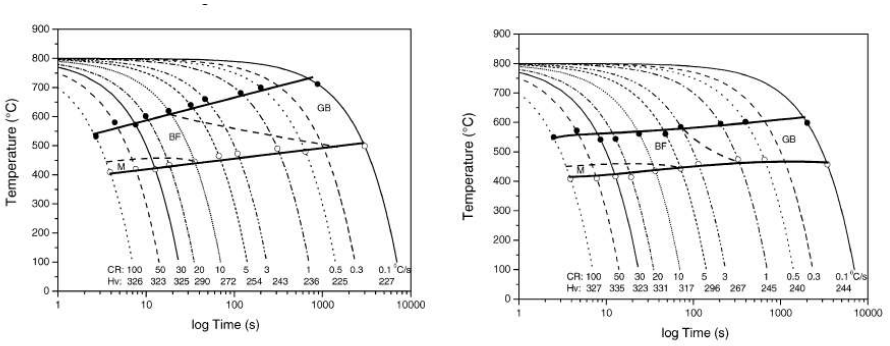

Figure 2.23: CCT diagram for the steel composition shown in table 2.13[66].

2.8.2 Multipass welding

Zhu et al.[52] simulated two thermal cycles for three types of X70 steel using a gleeble thermal-mechanical simulator. The chemical compositions of the steel considered are shown in table 2.14 and the thermal profile is shown in figure 2.24, which was calculated using a Rykalin 2d model. The heat inputs for the first and second weld were 2.34 kJ/mm and 2.46 kJ/mm respectively. The cooling time $\Delta t_{8/5}$ is mentioned to be 38.5 seconds for the first pass, and was taken the to be the same in the second pass.

The general microstructure of the steel after the subsequent thermal cycles consisted of a mixture of bainitic ferrite and granular bainite. Significant amounts of blocky M-A constituents were found, which is thought to give rise to a higher hardness in the reheated HAZ. A fraction of stringer M-A was found dispersed throughout the microstructure. The M-A constituents were revealed by etching with Lepera's etchant. The change in hardness is shown in figure 2.25, which also shows that the simulated HAZ gives a good result for the determination of the hardness. A correlation between the Ti/N ratio and the fraction and morphology of the M-A constituents, which was also investigated, was not found.

Zhu et al.[67] also investigated the effect of the peak temperature of the second thermal cycle on the microstructure of steel of the composition of steel 2 in table 2.14. The same cooling rate was investigated as in the previously discussed

article in this section, and as intercritical second cycle peak temperatures 813, 838 and 868 ˚C were chosen. The general microstructure when reheated to 813 ˚C was found to consist of mostly bainitic ferrite lath's and when reheated to 838 and 868 ˚C the main microstructure was an equiaxed ferrite phase. The fraction of M-A constituents was found to decrease significantly with increasing reheat temperature. The hardness was found to increase with increasing M-A fraction and thus decrease with increasing reheat temperature. The charpy impact energy was found to increase with increasing reheat temperature and thus a correlation between hardness and toughness seems possible. The results found by Zhu et al.[67] are shown in table 2.15 and figures 2.26 and 2.27 .

Steel no	C	Si	Mn	P	S	Cr	Mo	Ni	Al
1	0.05	0.24	1.57	0.01	0.0015	0.0287	0.15	0.21	0.035
2	0.05	0.23	1.62	0.01	0.0015	0.017	0.14	0.20	0.042
3	0.05	0.22	1.56	0.01	0.0015	0.026	0.15	0.20	0.043

Steel no.	B	Ca	Cu	Nb	V	Ti/N
1	0.0001	0.0015	0.15	0.058	0.026	2.44
2	0.0001	0.0027	0.15	0.055	0.023	3.22
3	0.0001	0.0021	0.15	0.055	0.024	4.88

Table 2.14: Chemical composition in wt% of the steel discussed by Zhu et al.[52]

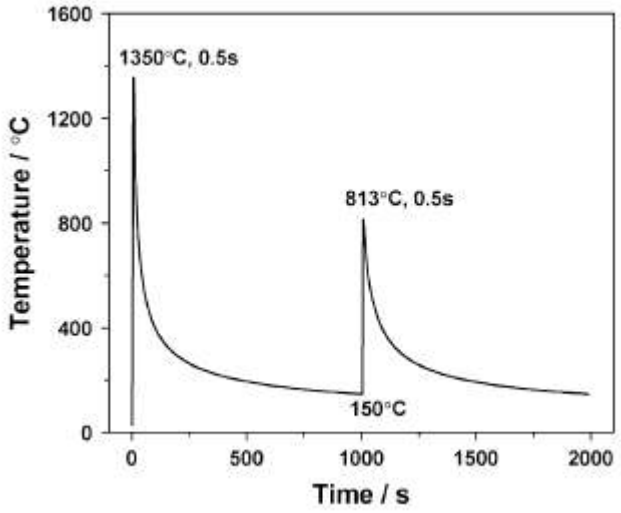

Figure 2.24: Temperature profile used by Zhu et al.[52]

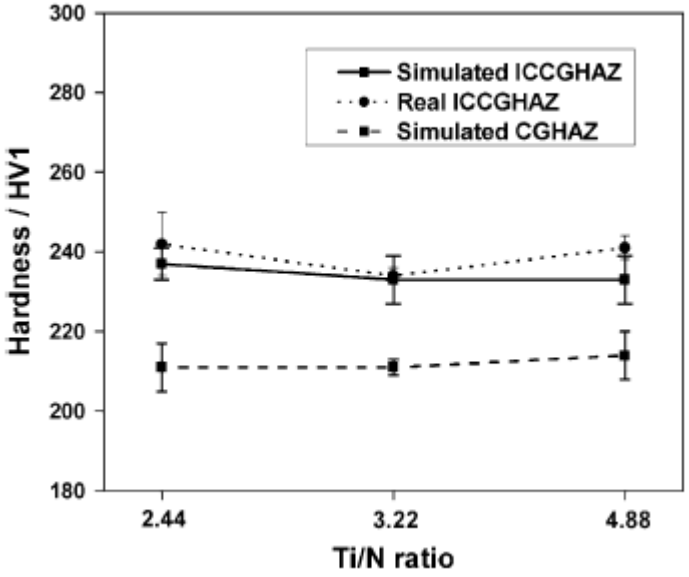

Figure 2.25: The vickers hardness found for the steels discussed by Zhu et al.[52]

Reheat temperature (°C)	813	838	868	CGHAZ
Fraction M-A (%)	6.6	5.3	1.5	1.6

Table 2.15: The M-A fractions found by Zhu et al.[67] for different reheat temperatures and the CGHAZ.

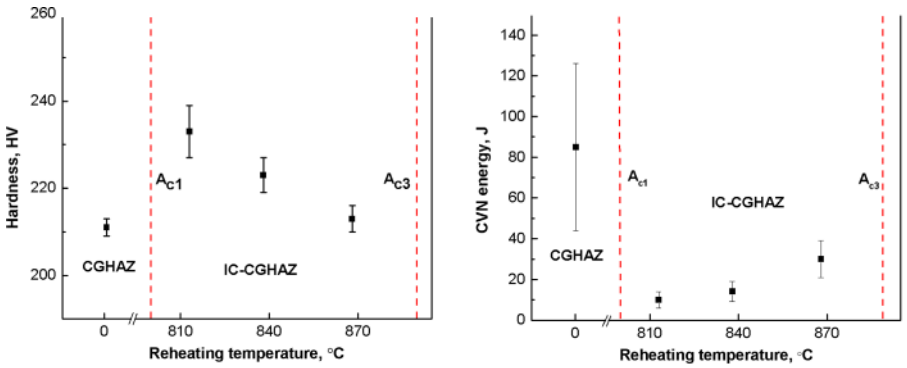

Figure 2.26: The hardness and charpy absorbed energy (at -20°C) found by Zhu et al.[67].

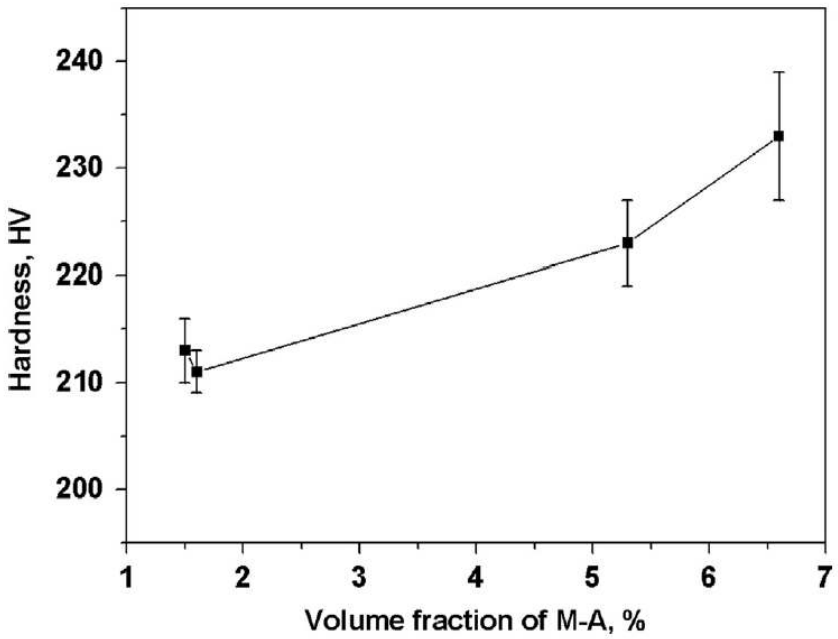

Figure 2.27: Hardness found by Zhu et al.[67] as a function of reheat temperature.

Li et al.[48] also discussed the influence of reheating on the CGHAZ in X70 steel of the composition shown in table 2.16. For this, gleeble simulations were performed using the temperature profiles shown in figure 2.28. The reheat cycles are characterized by a fairly high cooling rate of 60°C/s. The equilibrium transformation temperature as given by equation (2.1) was assumed for Ac1. The vickers hardness after the reheat cycle was measured for the 4 different peak temperatures and the microstructure was examined using optical microscopy. It was found that the microstructure mainly consisted of granular bainite and lath bainite, depending on the peak temperature. The microstructure did not change when the steel was reheated into the sub-critical range. Some fraction of M-A constituents was also found, the fraction was however relatively small, which is attributed to the effect of accelerated cooling. The morphology of the M-A constituents was found to be elongated and parallel in both the CGHAZ and the IC CGHAZ and only a small deterioration in charpy impact toughness was found in the IC CGHAZ. The hardness was measured for the different peak temperatures , which are shown in figure 2.29. No reason for the hardness change is given. It should be noted that, whereas the measurement error in vickers hardness is significant, the error in measured charpy absorbed energy is taken to be zero which would not be the case.

C	Si	Mn	S	P	Cr	Mo
0.05	0.26	1.48	0.003	0.012	0.027	0.17
Cu	V	Ni	Ti	Nb	C_{eq}	
0.22	0.052	0.15	0.016	0.05	0.404	

Table 2.16: Chemical composition in wt% of the steel discussed by Li et al.[48]

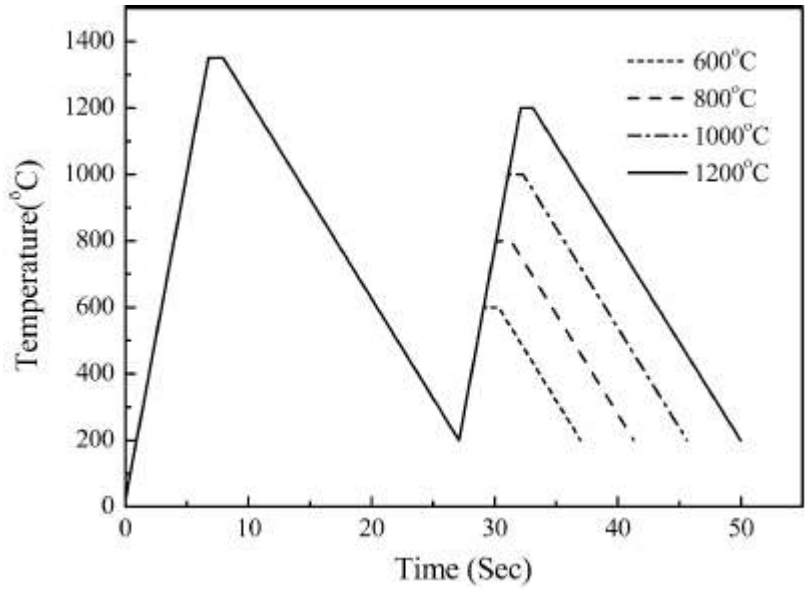

Figure 2.28: Temperature profile used by Li et al.[48]

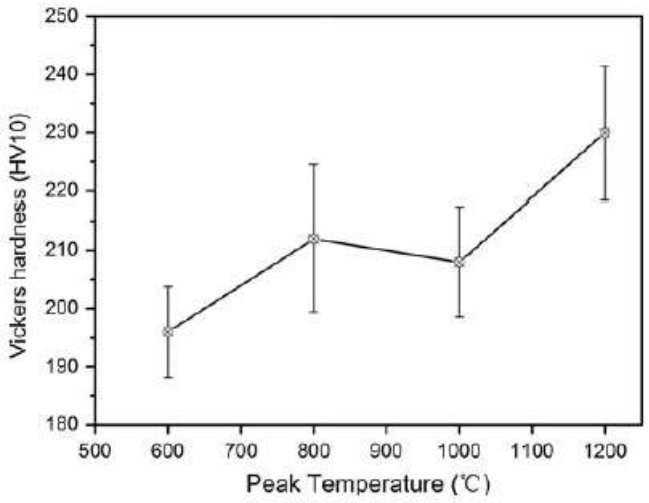

Figure 2.29: Hardness found by Li et al.[48] for different reheat peak temperatures

Davis and King[22] discussed the effect of cooling rate and reheat peak temperature on the toughness and microstructure in a X65 linepipe steel with the composition shown in 2.17 by simulating the heating cycles. For cooling times $t_8/5$ of 5, 30 and 300s (using a similar temperature profile as in figure 2.24 with an interpass temperature of 200°C) the microstructure was investigated for various reheat peak temperatures between 666 and 820°C with four of the peak temperatures within the intercritical zone. The equilibrium transformation temperature as given by equation (2.1) was assumed for Ac1. Hardness measurements were done for the different peak temperatures and the results are shown in figure 2.30. Also the difference in microhardness between the grain boundary, and the grain center were measured for the three different cooling rates at a single intercritical peak temperature, giving an increasing hardness with cooling rate in the grain boundary and a constant hardness in the grain center. It was noted that the microhardness indentations were bigger than the particles at the grain boundaries resulting in a only a estimated value of the hardness.

M-A constituents were found on the bainite lath boundaries and the prior austenite grain boundaries, which gives the reason for the difference in hardness between the center of a grain and the boundaries. The fraction and morphology of M-A constituents changed with reheat temperature which is summarized in figure 2.31. It was found that the toughness was worst when the M-A phase were a nearly connected phase at the prior austenite grain boundary.

C	Si	Mn	P	S	Cr	Mo
0.083	0.3	1.23	0.012	0.004	0.12	0.11
Ni	Al	N	Nb		Ti	V
0.49	0.038	0.007	<0.005		0.011	0.05

Table 2.17: Chemical composition in wt% of the steel discussed by Davis and King[22]

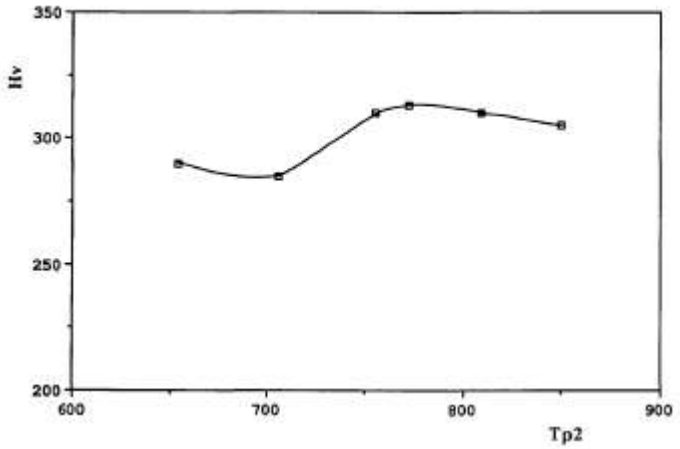

Figure 2.30: Hardness measurements done by Davis and King[22] with a load of 50g on steel with the composition shown in table 2.17 for different reheat peak temperatures, at a cooling $t_{8/5}$ of 30s.

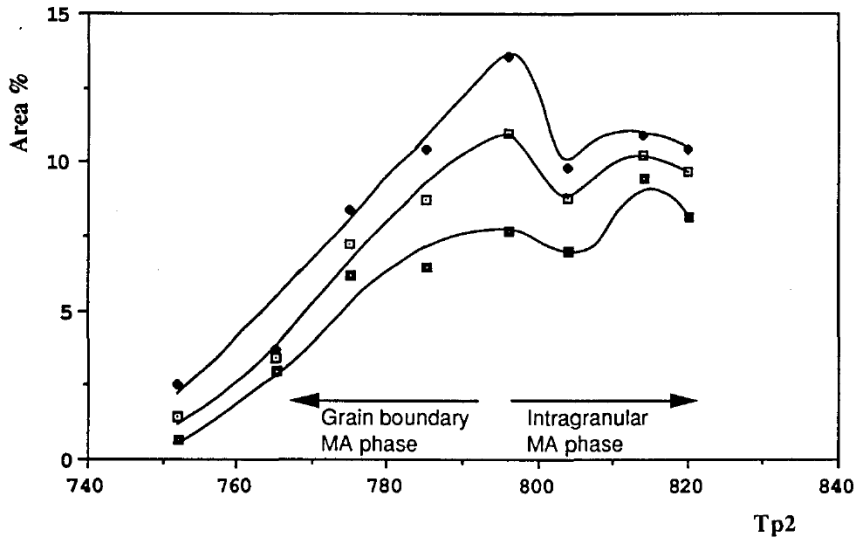

Figure 2.31: The fraction of M-A constituents found by Davis and King[22] as a function of reheat temperature

Li et al.[68] studied the effect of the addition of Vanadium and Niobium to low alloy steels, on the microstructure and mechanical properties of the IC CGHAZ by simulating the heating cycles. The compositions of the steel discussed are shown in table 2.18. The characteristic cooling time $\Delta t_{8/5}$ is 24s for both the temperature cycles, which is the cooling time for submerged arc welded plates of 25mm thickness, with a heat input of 3.6 kJ/mm. Two (possibly) intercrittical reheat temperatures are discussed, 750 and 800 °C.

The effect of added V and Nb on the hardness, toughness and CTOD was measured and the microstructure constituents were studied. A notable result is that the plain carbon steel (without added Nb or V) CGHAZ was found to be softer after the second weld pass. This effect became less with added V, and only when Nb was added, the IC CGHAZ had a higher hardness than the CG-HAZ. As the steel discussed byZhu et al.[52](in section 2.8.2) contained Nb, the hardness increased after the second weld pass, confirming this effect. Overall the hardness increased with added alloying elements. The change in toughness found could not be directly related to the change in hardness.

The microstructure of the CGHAZ in the vanadium steels consisted of numerous polygonal ferrite grains while grain boundary ferrite was the main constituent in the steel without V. The Intragranular M-A of the Vanadium steel was much finer with increased fractions of acicular ferrite and a reduced bainite fraction, and very few coarse ferrite side-plates, which was common in the plain steel. Steel with added Nb contained fewer grain boundary ferrite, but an increased

fraction of ferrite side-plate. After intercritical reheating, these microstructure features were still present . The fraction of M-A was found to change with the reheat peak temperature, but the scatter of results was too big draw conclusions. Added V increased the area fraction, average and maximum size of M-A constituents, the same effect of V addition was found by Chen et al.[69] for the CGHAZ. Addition of Nb increased the fraction size of the M-A phase even more than V. The effect of adding Nb to the microstructure after one weld pass was shown by Zhang et al.[63] and Kong and Qiu[64] and confirms the increased amount of M-A constituents with added Nb. The toughness values were found to be worst for steel with added Nb.

Steel	C	Si	Mn	P	S	Al	N	Nb	V	B
C	0.092	0.20	1.41	0.005	0.004	0.039	0.067	<0.005	<0.005	<0.0005
LV	0.084	0.21	1.42	0.005	0.002	0.031	0.047	<0.005	0.05	<0.0005
V	0.094	0.21	1.44	0.005	0.003	0.029	0.052	<0.005	0.10	<0.0005
Nb	0.100	0.19	1.40	0.005	0.002	0.031	0.040	0.031	<0.005	<0.0005

Table 2.18: Chemical composition in wt% of the steel discussed by Li et al.[68]

2.8.3 Microstructure and toughness

A fair number of papers have been written on the decrease in fracture toughness in the CGHAZ and the reheated CGHAZ of low carbon HSLA steels. This section gives a summary of the findings of several papers on the reason for this decrease in fracture toughness, both related to M-A constituents and the overall microstructure.

Davis and King[46] list four mechanisms with which M-A consitutuents influence fracture toughness. These mechanisms are:

- M-A constituents are brittle crack readily and initiate cleavage in surrounding ferrite. Noting that elongated particles do crack whereas the blocky particles do not.
- Residual stress in the ferrite matrix induced by the transformation assists cleavage fracture.
- M-A particles generate stress concentrations due to the yield strenght difference with the matrix causing debonding, which assists fracture. This effect is greater for M-A particles which are more closely spaced.
- A microcrack forms at the boundary between M-A and matrix through interfacial decohesion. This crack initiates cleavage fracture by linking microcracks at multiple M-A particles.

Figure 2.32 shows a schematic overview of these mechanisms.

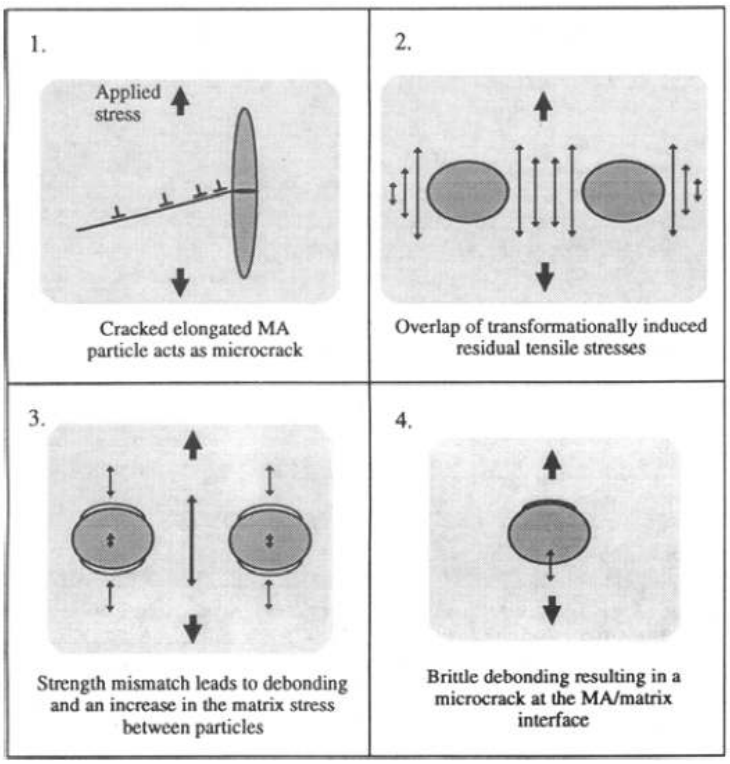

Figure 2.32: The four fracture initiation mechanisms as discussed by Davis and King[46].

It is concluded that cleavage fracture arises from the second an third mechanism (determined by the local stress state[70]) which are possible for closely spaced blocky M-A particles and than the fraction of M-A is less important. The presence of M-A will not, by itself, give rise a lower toughness. This effect of M-A distribution on the fracture toughness was confirmed by Zhu et al.[67]. The occurrence of cleavage fracture by the second and third mechanism was also confirmed by Mohseni et al.[58].

Lan et al.[71] found that the maximum size of the M-A constituents increases for higher heat input which resulted in a toughness deterioration caused by the debonding mechanism discussed by Davis and King[46]. Hu et al.[47] discuss that the toughness degradation is due to microcrack formation, which are larger for bigger M-A particles.

Li and Baker[72] noted that the deterioration in fracture toughness of the ICG-HAZ is primarily due to M-A constituents. At high stresses, cracking of blocky M-A particles was found to be important, and at low stress values decohesion of stringer M-A particles.

Yokoyama and Nagumo[73] concluded that brittle fracture in the CGHAZ arises from the increased inhomogeneity and found cracks to initiate on the boundary between bainitic ferrite and (quasi-)polygonal ferrite, due to strain localization in the microstructures of lower strength. No effect of M-A consituents was discussed.

Lambert-Perlade et al.[70]; Lan et al.[74] found that the the presence of coarse upper bainite structures is also detrimental to the fracture toughness, where a fine bainite structure, with high angle grain boundaries between the packets, arrests crack propagation. Lambert-Perlade et al.[70] also fitted theoretical models to measured data which is beyond the scope of this work.

Mohseni et al.[58] did find twinned martensite at cleavage initiation sites using transmission electron microscopy. Confirming M-A to be possible initiation sites for fracture. Whereas Ohya et al.[75] concluded, from charpy impact experiments, that M-A, of which a fraction of 10-12 %was present during the experiments, were most likely not responsible for cleavage initiation but rather the interfaces between bainitic and quasi polygonal ferrite. Zhao et al.[2] Also found the presence of coarse bainitic structures to be detrimental to the fracture toughness.

2.9 Conclusions

Even though significant work has been performed on pipeline welding and its influence on the microstructure of linepipe steel, the results of these studies cannot be directly applied to the pipeline welding of Allseas engineering. The main focus of recent research has been on linepipe steel graded above X70, which is concering microstructures and chemical compositions different from the X65 linepipe steels mainly used by Allseas engineering. Furthermore, because of the inconsistency in cooling rates related to heat input, the weld processes simulated by previous research cannot be easily related to weld processes used by Allseas engineering. For these reasons, there is a need for seperate research regarding steels and weld processes used by Allseas engineering.

In order to perform this research, linepipe steel of four different compositions will be subjected to a CGHAZ temperature profile, after which the microstructure will be examined by both optical microscopy and electron microscopy, as well as electron backscatter diffraction. The microstructural features will be linked to fracture toughness assessments done in previous research.

Chapter 3

Methods and equipment.

3.1 Steels considered

For this research, three SAWL pipeline steels were considered and one SMLS pipeline steel. The chemical composition of these steels which are considered in this research are shown in table 3.1, the composition of the steels shown here is as measured by optical emission spectroscopy. The plate (pipe wall) thickness of steel A is 36.6 mm, C and D have a thickness of 39mm and D a thickness of 30 mm. A,B and C are steels from a SAWL pipeline and D from a SMLS pipeline. The longitudinal weld in the SAWL pipes was not considered in this research, due to inhomogeneity in microstructure and chemical composition in this part.

Table 3.1: Chemical composition (in wt %) and Pcm of the steels considered in this research. As measured by optical emission spectroscopy.

Steel	C	Mn	Cr	Si	Mo	Nb	Al	Ti	Cu
A	0,041	1,33	0,26	0,31	0,19	0,030	0,023	0,011	0,012
B	0,034	1,51	0,15	0,20	0,01	0,041	0,031	0,015	0,019
C	0,068	1,27	0,02	0,23	0,18	0,035	0,022	0,014	0,203
D	0,053	1,34	0,26	0,29	0,22	0,002	0,033	0,011	0,018

Steel	Ni	V	B	Pcm
A	0,009	0,0046	0,0002	0,146
B	0,015	0,0069	0,0002	0,126
C	0,376	0,0487	0,0002	0,174
D	0,079	0,0586	0,0002	0,167

3.2 Dilatometry

In order to find the non-equilibrium transformation temperatures of the steels involved at high heating rate, dilatometer experiments were carried out. A dilatometer measures the size of a sample with high accuracy at a certain temperature, giving the thermal expansion of the sample. Because the lattice parameter of Austenite is smaller than that of Ferrite, a shrinkage of the sample will occur at the transformation temperature. A typical measurement graph for the steels considered is shown in figure 3.1. Various methods can be considered to evaluate these curves and find the transformation temperature, these methods are shown in figures 3.2 to 3.7. Figure 3.2 shows the part of the dilatometer measurement curve which is used to illustrate the evaluation methods. This part is the transformation from ferrite to austenite and is the most relevant part considered in this research. The method shown in figure 3.3 gives Ac1 and Ac3 by extrapolating the part of the curve when the steel is fully ferritic and the part where the steel is fully austenitic, which is an almost linear part of the curve (Method I). The transformation temperatures are the points at which the curve start to deviate from these linear parts, for which a minimum angle can be defined. Figure 3.4 shows essentially the same method, but now considering the small linear part just before the transformation(method II). This method is dependent on the material is still fully ferritic in this section. Figures 3.5 and 3.6 (method III and IV) show another method involving a third tangent at the part of the curve where the transformation occurs and the sample shrinks. The transformation temperatures are now the intersections between the tangents. The method shown in 3.7 is a method similar to that in fig. 3.3 and 3.4 but more quantitative by differentiating the curve and defining a critical deviation from the linear part (method V). For the analysis of the dilatometer results for the current research, Ac1 was taken as the point where the curve was lower than the minimum value in the linear part, which is denoted in figure 3.7.

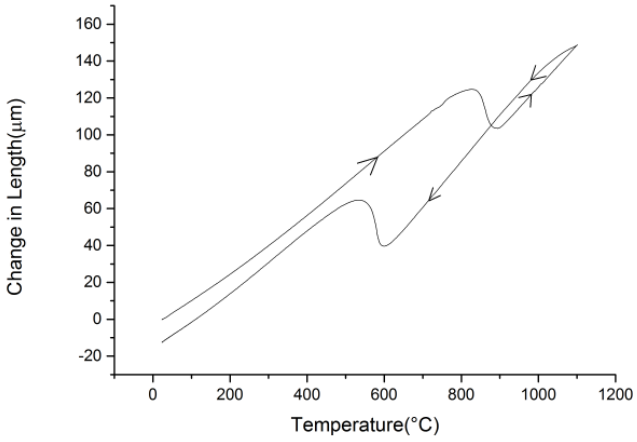

Figure 3.1: Typical dilatometer measurement curve, the arrows indicate heating and cooling sections.

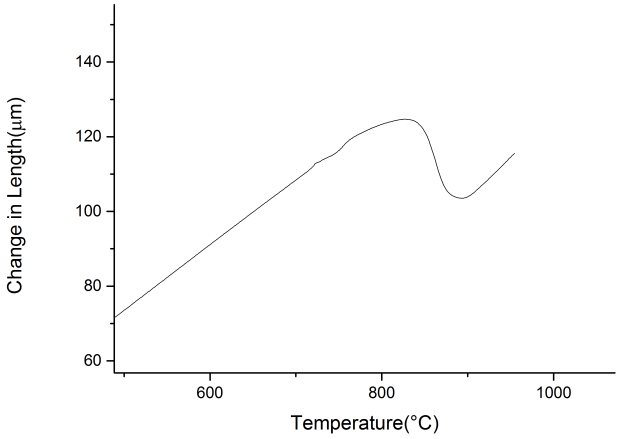

Figure 3.2: Dilatometer measurement in close to the austenite transformation.

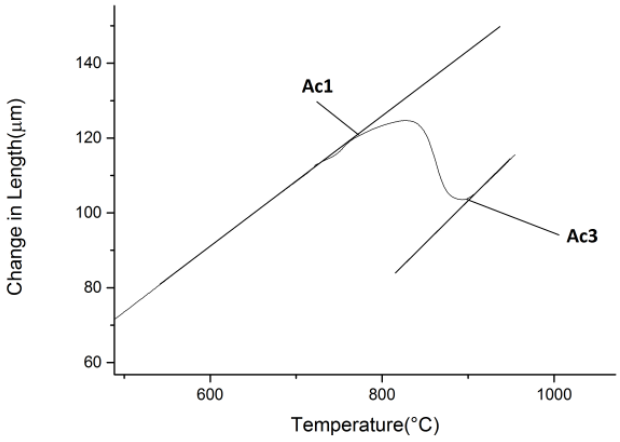

Figure 3.3: Determination of the transformation temperatures using extrapolation of the linear parts of the curve.

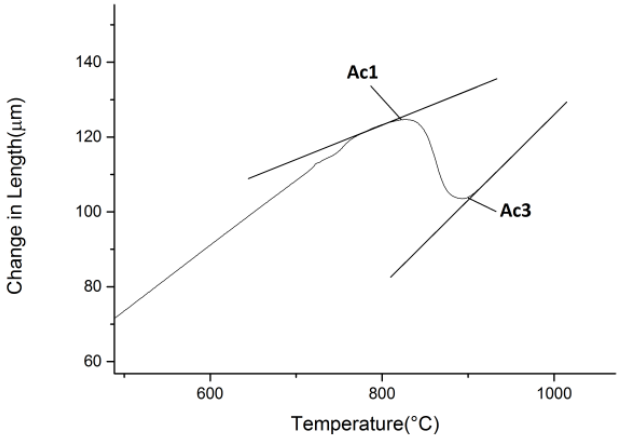

Figure 3.4: Determination of the transformation temperatures using extrapolation of the linear parts of the curve(different from figure 3.3).

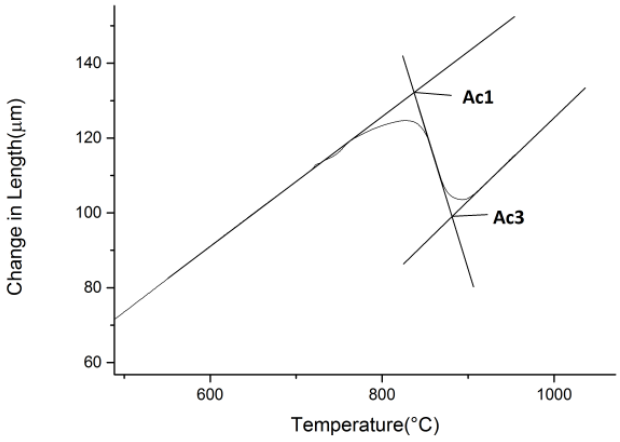

Figure 3.5: Determination of the transformation temperatures using a three tangent method.

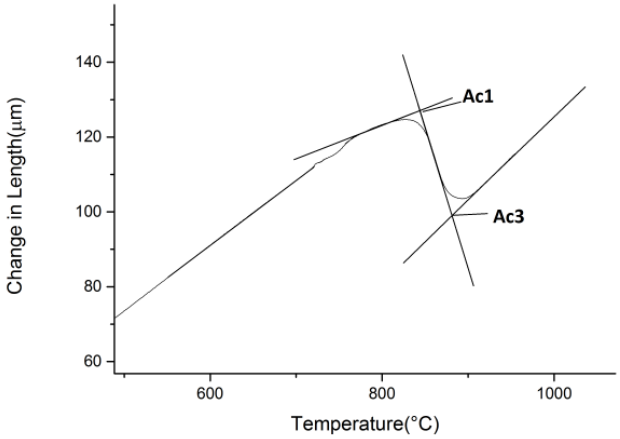

Figure 3.6: Determination of the transformation temperatures using a three tangent method.

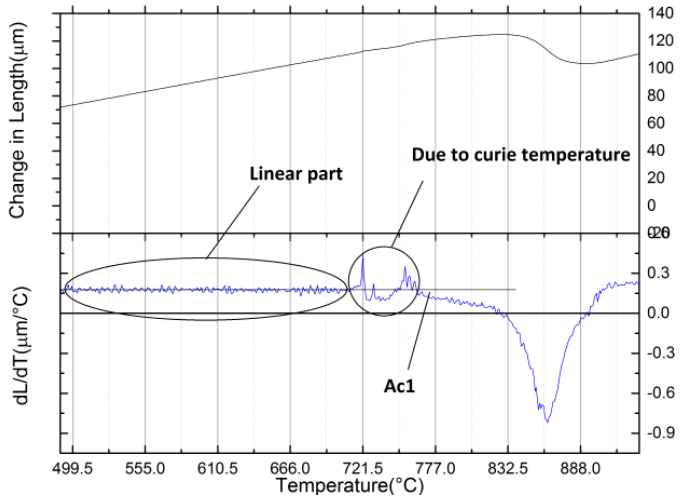

Figure 3.7: Determination of the transformation temperatures using the derivative of the measurement curve.

The experiments were carried out using a TA instruments Dil 805 A/D dilatometer. This dilatometer heats the samples by means of a high frequency current generator, of which the magnetic field induces eddy currents within the (conducting) sample. The sample heats up by Joule heating due to the induced currents. Ferromagnetic samples are also subject to heating from magnetic hysteresis. The dilatation is measured by placing the sample between two small fused silica tubes, of which the thermal expansion is accounted for by the controlling software. Samples with the dimension of 10x4x1 mm were cut from the pipe wall by precision cutting using a struers secotom-10 cut-off machine. A schematical drawing of the setup is shown in fig. 3.8.

The samples were heated at a rate of 50 °C/s to 1150°C(the maximum operation temperatures of the fused silica holders) and subsequently quenched using helium gas. The input power was measured during the heating, which will see a significant increase at the curie point on account of the loss of hysteresis heating. When considering steel A from table table 3.1, the thermal cycle was repeated on the same sample to check the dependence of the transformation temperatures on the base metal microstructure.

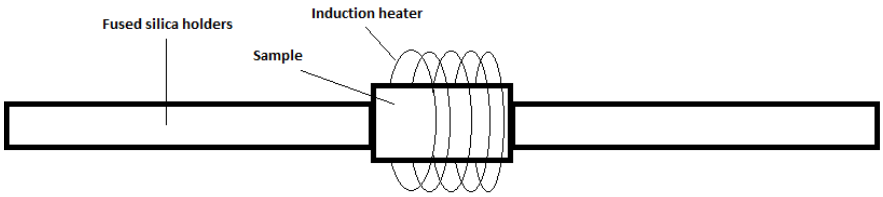

Figure 3.8: Schematic overview of of the dilatometer setup.

3.3 Gleeble® simulations.

In order to simulate the microstructure change due to multipass pipeline welding, the cooling and heating rates were determined using computer simulations of the welding process. These simulations were done by using both Abaqus finite element analysis (fea) and Simufact.welding for two extremes of the heat input used for pipeline welding by allseas engineering, these simulations will not be discussed in more detail. The thermal cycles found with these simulations were simplified in order to get a good thermo-mechanical simulation. The controlling parameter for the cooling transformation herein was taken to be the cooling rate between 800 °C and 500 °C. The designed thermal cycles are shown in figure 3.9 and table 3.2. The values given in figure 3.9 are constant for all experiments, the rest are given in table 3.2. The table gives the heat input for which the cycle was designed (HI), the holding time at both peak temperatures (HT), the cooling rates between 800 °C to 150 °C (CR2) and PT2 to 150 °C (CR3) and the second peak temperature (PT2). For the experiments the designations shown in table 3.2 will be extended by putting the letter of the steel, shown in table 3.1, in front of the designation. For example, steel B subjected to temperature profile IHI-810 will be designated B-IHI-810.

Note that the cooling rates in the first and the second cycle are not the same, which is a direct result of the computer simulations and is opposite from a big part of previous research which often make use of over-simplified theoretical models [52] [48] [76].

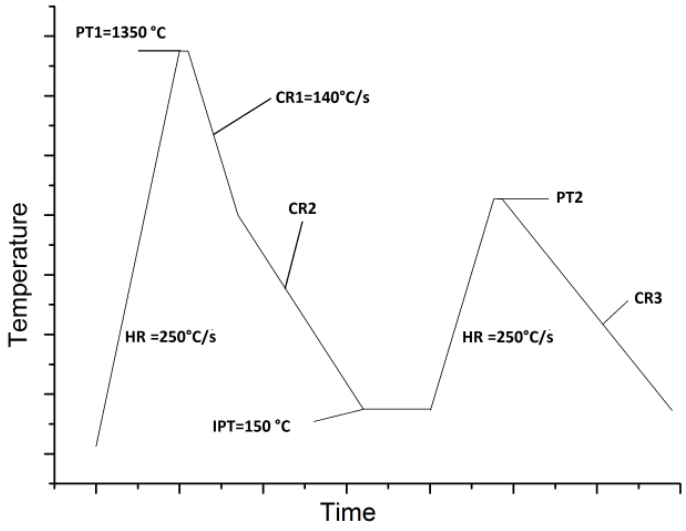

Figure 3.9: Overview of the thermal cycles, the values not mentioned in the table are shown in 3.2

Table 3.2: Overview of the parameters for the designed thermal cycles.

Designation	HI (kJ/mm)	HT (s)	CR2 (°C/s)	PT2 (°C)	CR3 (°C/s)
LHI-810	0.5	0.5	80	810	65
LHI-860	0.5	0.5	80	860	65
IHI-810	-	1	50	810	35
IHI-860	-	1	50	860	35
HHI-810	2.5	2	25	810	13
HHI-860	2.5	2	25	860	13
LHI	0.5	0.5	80		
IHI	-	1	50		
HHI	2.5	2	25		

The thermal cycles of the welding process were investigated using a Gleeble® 1500 thermal-mechanical simulator. The Gleeble®uses joule heating to heat the samples by passing a high current trough the sample. The temperature was controlled using a type K thermocouple. A cylindrical shaped sample, with a diameter of 6mm and a length of 100mm, was machined, by lathing, from the pipe steel in the rolling direction of the pipe. This rod was clamped between

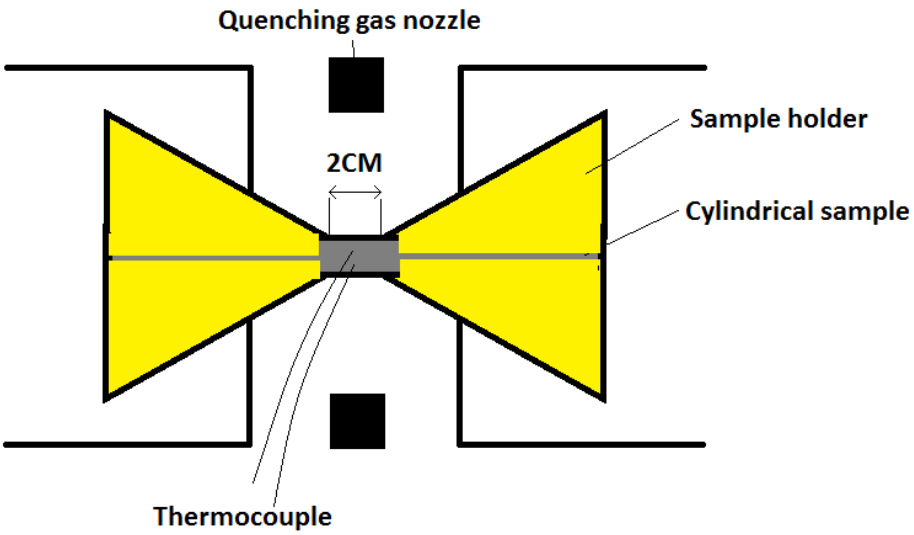

Figure 3.10: Schematical overview of the Gleeble®experimental setup.

two copper holders and a free span of 2 cm was kept between the holders. The thermocouple was spot welded to the sample in the middle between the two holders, as shown in figure 3.10. The temperature was controlled by the Gleeble®using a sampling rate of 50Hz. In cooling phase of the LHI temperature profiles, the sample was cooled using Helium gas in order to get sufficient cooling, for the other profiles Nitrogen gas was used. In the HHI-810 and HHI-860 temperature profiles, no cooling gas was used to reach the cooling rate of 13 ˚C/s.

3.4 Optical microscopy.

In order to investigate the microstructure of the base metals and Gleeble samples, optical microscopy was performed. From the base metals a sample was cut in the rolling direction-normal direction plane, the gleeble samples were cut within 1.5 mm from the attached thermocouple. All samples were embedded in resin and ground using sandpaper with ISO designations and particle size : P80 (201 µm), P180 (82 µm), P320(46.2µm), P800 (21.8 µm), P1200 (15.3 µm),P2000 (10.3 µm). After grinding, the steel was polished using diamond polish with particle sizes 3 µm and 1 µm. After polishing the samples were cleaned with some soap and a stream of water, and secondly with ethanol.

For revealing the microstructure, two different etchants were used. The first one is nital, which is a solution of nitric acid in alcohol (in this case a 2g/l solution). Nital etches ferrite grain boundaries and may etch ferrite lightly de-

pending on the crystal orientation of the ferrite grain[7]. The second etchant is known as 'Lepera's etchant', which is a 1:1 mixture of picric acid in alcohol (a 4g/l solution) and sodium metabisulfite in distilled water(1g/l solution). This etchant was developed for use on dual phase steel, it etches ferrite brownish tan, bainite black and does not etch martensite. A stock solution of this etchant cannot be kept and the two parts need to be mixed just before etching and it can be used only once.[60]. Depending on the etching result, the samples were submerged in the etchant for 10-30s. The etched samples were investigated using a Keyence VHX-5000 microscope.

After microscopy of the Lepera etched samples, the photos made were analyzed using ImageJ image processing software. In some cases the contrast which was achieved by etching with the Lepera's etchant, was not sufficient for visualization or do fraction analysis, the contrast was therefore enhanced using ImageJ. The M-A constituents were analyzed by doing a particle analysis.

3.5 Electron Backscatter Diffraction

As optical microscopy is not a quantative method of describing microstructure, electron backscatter diffraction (EBSD), which is sometimes called backscatter Kikuchi diffraction, was also employed. EBSD is configured by letting a stationary electron beam in a scanning electron microscope (SEM) hit a tilted sample, which creates patterns by diffraction on the crystal lattice. These patterns, which are called electron backscatter patterns (EBSP) are projected upon a phosphorus screen and can be analysed in order to get the crystal orientation and phase. An overview of a typical setup is shown in figure 3.11.[77;78].

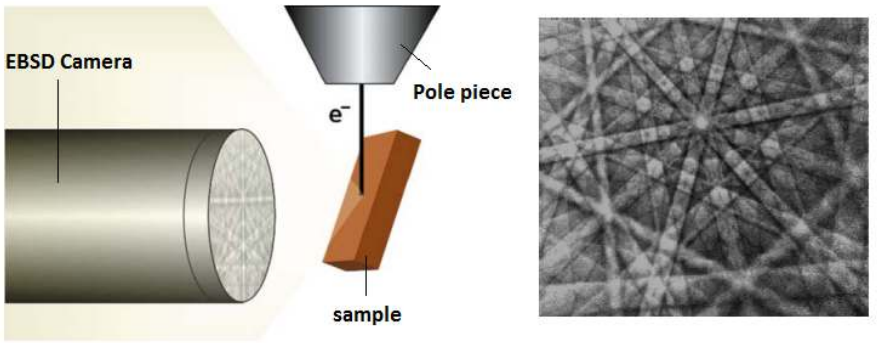

Figure 3.11: (left) an overview of the setup used for EBSD measurements (right) a typical EBSP. Taken from: Schwartz et al.[78]
.

When the beam is now scanned across the surface with a predefined distance between measurement points (the step size), a map of crystal orientations and

phase is obtained. This map gives detailed information about phase, crystal orientations, texture and grain size. The image quality (IQ) of every EBSP is the amount of blurriness in the optained EBSP and is caused by point defects, dislocations, lattice strains or a superposition of diffraction patterns. Due to the dependence of the IQ on dislocation density, a differentiation can be made between the more dislocation dense martensite or bainite and ferrite. This differentiation is impossible to make by only using the crystal orientation and phase, as the bct structure of martensite and de bcc structures of bainite and ferrite are indistinguishable.[79;80].

A method for the quantification of microstructure constituents was purposed by Wu et al.[81] and assumes that every microstructural constituent in steel generates a Gaussian IQ distribution. If a microstructure consists of multiple microstructures, the IQ distribution will thus be a summation of the separate constituents. In order to find the best fit a sum of Gaussian curves to the IQ data, the "curve fitting toolbox" in mathworks MATLAB® was used. In order to use this properly, first an assumption was made about the number of microstructural constituents present in the scan.

When a measurement point is indexed, a confidence index (CI) is calculated for the indexation according to equation 3.1.

$$CI = \frac{V_1 - V_2}{V_{tot}} \tag{3.1}$$

Every detected EBSP can give several orientations through the image processing routine, and the appropriate orientation and phase is appointed using a voting scheme. In equation 3.1 V_1 an V_2 are the orientations with the highest and second highest number of votes and V_{tot} is the total number of votes given. The CI scale thus runs from 0 to 1, but is not linear with the change of an indexation being correct, as is illustrated by 3.12, which show the correctness of an indexation as a function of the CI. An illustration of the voting process is shown in figure 3.13[82]. The CI will be low at grain boundaries because of the crystal structure of both the grains interfering.

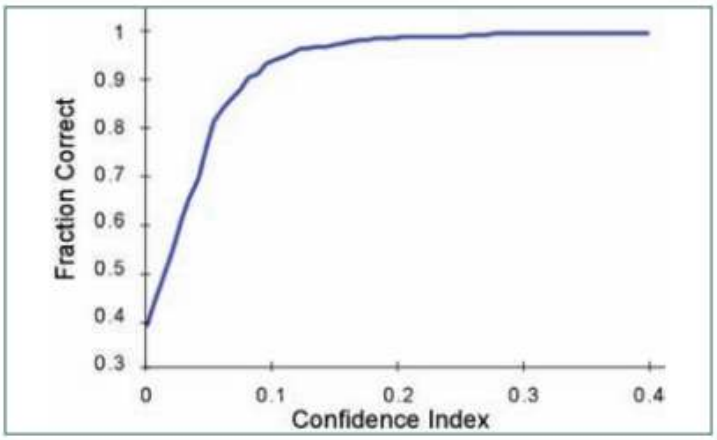

Figure 3.12: Graphical representation of the relation between correctly indexed orientations and the Confidence Index. [82]

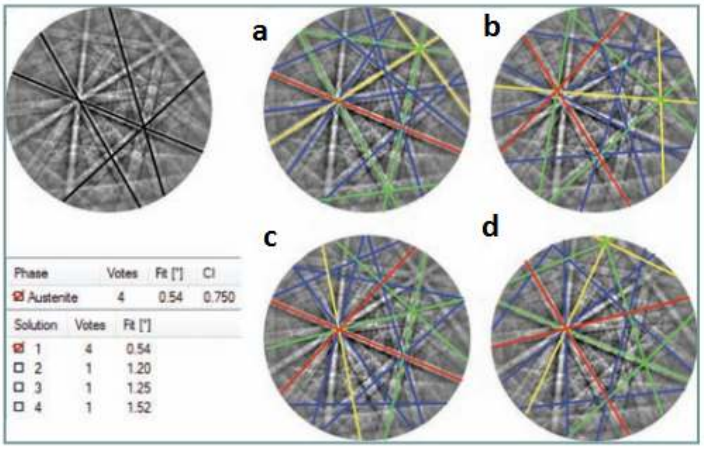

Figure 3.13: Illustration of the voting system used to find the correct orientation and phase. The fit in (a) gets 4 votes, (b)-(d) all get 1 vote. [82]

The sample preparation for ebsd measurements is the same as that for optical microscopy discussed in section 3.4 but as EBSD is very sensitive to surface deformation, an extra polishing step with small abbrasive particles, chemical polishing or electrolytic polishing is needed in order to remove the remaining surface deformation (mostly scratches). For this research an extra polishing of 30 minutes with Streuers OP-S was performed, which is an alkaline (pH=9.8) suspension of Colloidal silica with a particle size of 0.04 µm.

In the current research, a FEI quanta 450®microscope with field emission gun was used equipped with an EDAX DigiView®EBSD camera. The sample is tilted 70˚ with respect to the pole piece and the acceleration voltage of the SEM is set to 25kV and a working distance of 18mm was used. Depending on the measurement, a step size of either 0.1 µm, 0.15 µm or 0.20 µm was used, which from optical microscopy results should be sufficient to detect small microstructural details.

For the analysis of the EBSD results, both MTEX (matlab toolbox) and OIM Analysis were used. For the calculation of phase fractions the minimum grain size was set to 3 measurement points and the minimum CI was 0.05.

For the figures to be displayed, a grain dilation cleanup was performed. Grain dilation cleanup takes all measurement points which are not attributed to a grain (for which the minumum grain size was set to 2 measurement points) and assigns these to the biggest nearest grain or a grain at random. This process is iterated until every point is part of a grain. This cleanup is needed because points with a low confidence index, for which the indexation is probably wrong, are otherwise appointed their own grain. These points are mostly located along grain boundaries, which creates grain boundaries which are not well defined and which will not or falsely satisfy any orientation relationship. The process used for differentiating M-A constituents from the rest of the microstructure does not allow for this type of cleanup and this is done without.

3.6 Electron microscopy

Secondary electron microscopy and backscatter electron microscopy was performed on A-LHI-810 in order to gain more understanding of the M-A constituents. Sample preparation was the same as the nital etched light microscopy samples but now a shorter etch of about 5 seconds was used. An acceleration voltage of 15 kV was used for the imaging.

The contrast generated by secondary electron imaging is the relief generated by etching. Points which are closer to the detector generate a higher brightness and thus are less etched. The contrast for backscatter electron microscopy is generated by the difference in density, where a higher density generates a higher brightness.

3.7 Hardness measurements.

Vickers hardness measurements were performed using a Struers DuraScan hardness tester. Before testing, the material was polished up to a particle size of 3 µm, in order to get good automated measurements. For macroscopic measurements a force of 500g was chosen in to get a sufficiently large area but also

an indent which can be easily removed by grinding. When the diagonal of the indent is larger than 25 µm the vickers hardness value is usually scalable upward to higher forces[83]. The depth of a vickers indentations is $\frac{1}{7}$ of the diagonal[84].

Micro hardness measurements were done on the M-A constituents using a load of 10g in order to keep the indent as small as possible with the DuraScan hardness tester.

Chapter 4

Results

4.1 Dilatometry

Dilatometer curves were obtained for all steels listed in table 3.1, and the curves were analyzed by the methods described in section 3.2. The results of the dilatometer experiments when analysed by the various methods are shown in table 4.1, as well as the equilibrium temperatures calculated by equations (2.1) and (2.2). A characterstic of the dilatometer curves was that there was a change in thermal expansion just around the curie point. This is illustrated by figure 4.1, where the dilatometer curve is plotted together with the power needed for the heating. At the curie point, the heating by hysteresis heating is no longer present and more power is needed in order to heat up the sample. The curie point is found to be around 760 °C for all samples. Due to this effect, the first deviation from the linear value was not taken into account when the curves were analysed using method V.

Table 4.1: Delatometer results for the five different methods described in table 4.1 and the equilibrium transformation temperatures, $Ac1_{eq}$ and $Ac3_{eq}$. Temperature are given in °C.

Steel	Ac1(I)	Ac1(II)	Ac1(III)	Ac1(IV)	Ac1(V)	Ac3	$Ac1_{eq}$	$Ac3_{eq}$
A	778	820	840	848	779	937	721	910
B	776	816	840	851	775	911	715	903
C	761	790	792	-	765	889	714	906
D	766	783	810	-	775	918	719	911

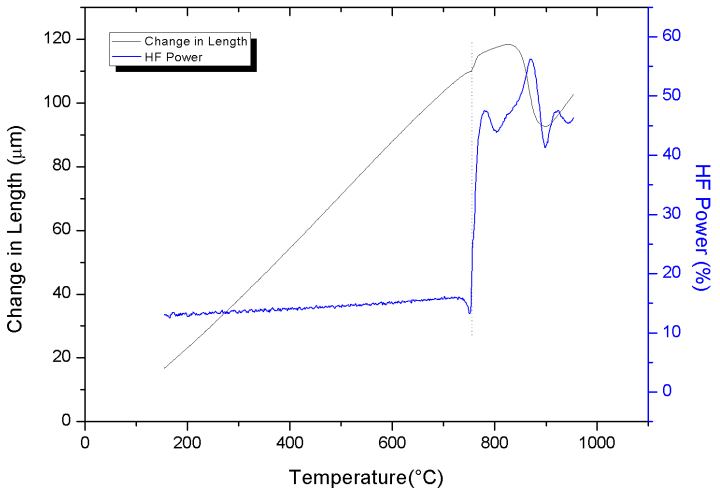

Figure 4.1: An example of dilatometer curves found with the apparent change in thermal expansion at the curie point.

4.2 Gleeble HAZ simulations.

Gleeble HAZ simulations were done as described in section 3.3. Some deviation from the temperature profiles chosen (table 3.2) were noted. At the low heat input temperature profiles (LHI,LHI-810 and LHI-860) the measured cooling rate deviates from the imposed cooling rate, as shown in figure 4.2.

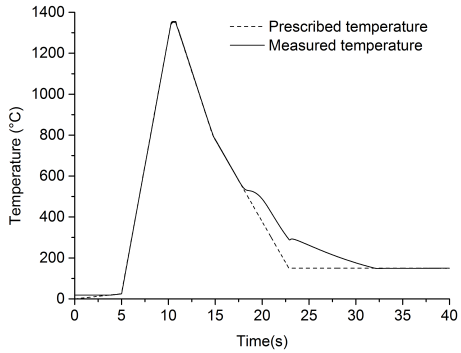

Figure 4.2: Curve showing the measured cooling rate and the prescribed cooling rate.

Some overshoot of the peak temperatures also occurred during the thermal simulations. The highest overshoot for the first cycle peak temperature was 10 ˚Cand for the second cycle 8 ˚C. As exception to these overshoots, a peak temperature of 2550 ˚C was measured for first thermal cycle of the D-LHI-810 sample. No melting was however visual on the sample after the simulation.

4.3 Optical microscopy

4.3.1 Base metal

The microstructure of the steels as examined by optical microscopy will be discussed in this section. The microstrucucture and especially the grain size differ significantly from the inner side (full thickness) of the pipe wall to the half thickness. This difference is best visible at the outer 5mm of the pipe wall, and is homogeneous in the middle part. The microstructure of steel A consists mostly of acicular ferrite with some etched dark areas, which are pearlite colonies, this can be seen in figure 4.3. No centreline segregation was observed using optical microscopy.

These pearlite colonies and acicular ferrite as well as polygonal ferrite are also found in the base microstructure of steel B, as can be seen in figure 4.4. Steel B also shows a clear morphology related to the rolling direction of the plate, especially at the edge of the pipe wall, with ferrite grains elongated in the rolling direction (figure 4.4b).

The base metal microstructure of steel C consists of acicular and polygonal ferrite, with pearlite colonies at the half thickness of the pipe wall. The microstructure at the edge of the pipe wall shows a clear morphology with large ferrite grains elongated in the rolling direction, with smaller, equiaxed ferrite grains in-between.

The microstructure of steel D is similar to that of steel A, but now highly substructured, especially at the edge of the pipe wall.

The nature of these microstructures makes determination of a grain size using standard 2d methods, such as the linear intersection method, nearly impossible.

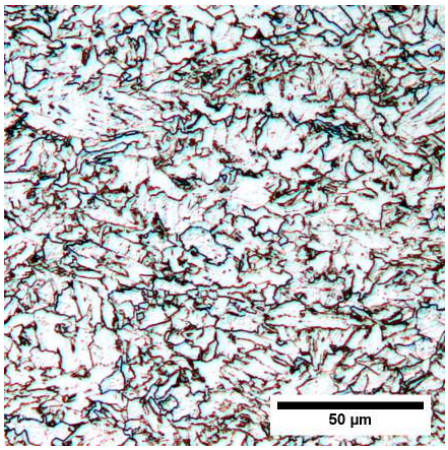

(a) Base metal microstructure of steel A at the half thickness of the pipe wall, nital etched 500× magnification.

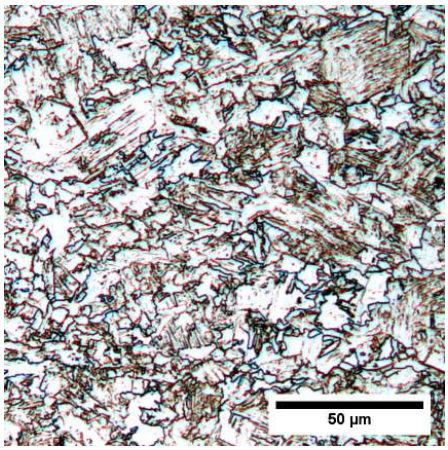

(b) Base metal microstructure of steel A at the full thickness of the pipe wall, nital etched 500× magnification.

Figure 4.3: Steel A base metal microstructure.

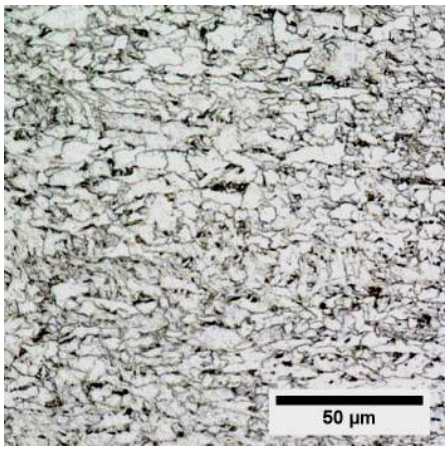

(a) Base metal microstructure of steel B at the half thickness of the pipe wall, nital etched 1000× magnification.

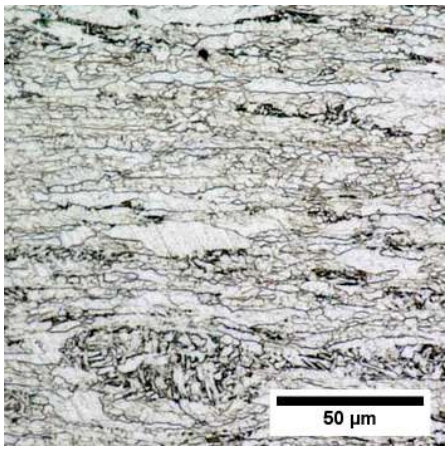

(b) Base metal microstructure of steel B at the full thickness of the pipe wall, nital etched 1000× magnification.

Figure 4.4: Steel B base metal microstructure.

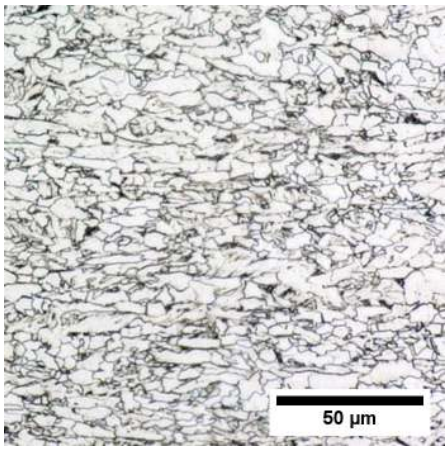

(a) Base metal microstructure of steel C at the half thickness of the pipe wall, nital etched 1000× magnification.

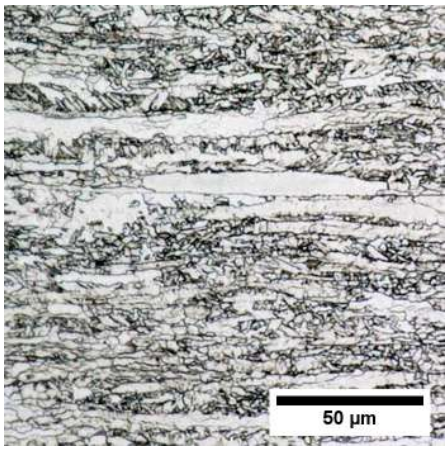

(b) Base metal microstructure of steel C at the full thickness of the pipe wall, nital etched 1000× magnification.

Figure 4.5: Steel B base metal microstructure.

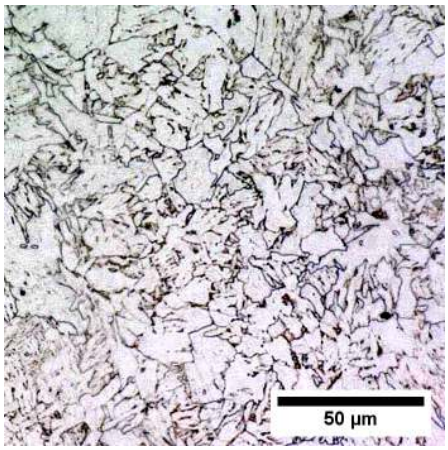

(a) Base metal microstructure of steel D at the half thickness of the pipe wall, nital etched 500× magnification.

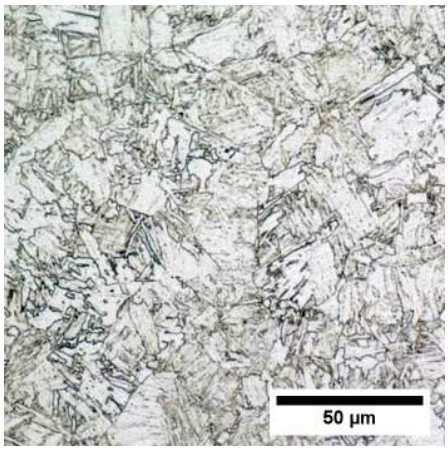

(b) Base metal microstructure of steel D at the full thickness of the pipe wall, nital etched 1000× magnification.

Figure 4.6: Steel D base metal microstructure.

4.3.2 Coarse-grained heat-Affected zone

In this section the optical microscopy results will be discussed of the Gleeble simulated samples of the CGHAZ, which are the temperature cycles LHI IHI and HHI described in table 3.2. The results discussed will be of the microstructures

as observed when etched by Nital, Lepera etching of the CGHAZ samples gave inconsistent results, as ilustrated by figure 4.7.

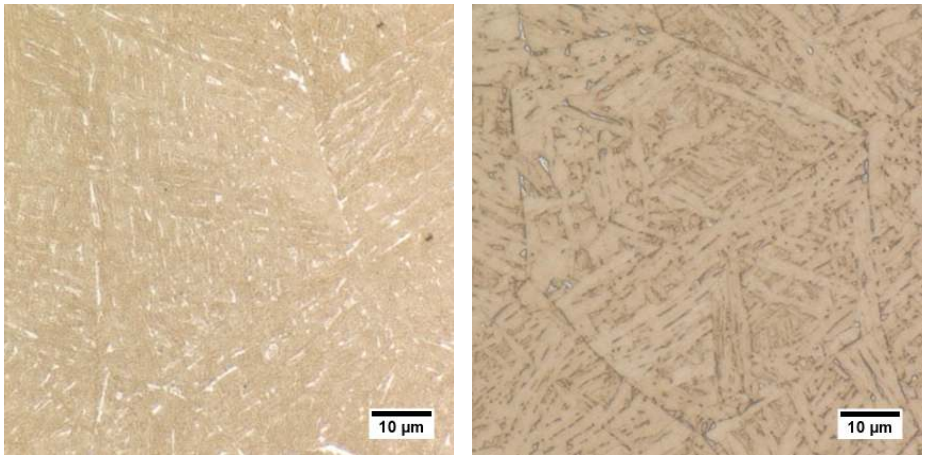

(a) (b)

Figure 4.7: Micrographs of the CGHAZ for A-IHI, etched with Lepera's etchant, 2500x magnification, showing the inconsistent etching effect.

The results for the LHI cycles are shown in figure 4.8 The LHI samples of steel A and D are somewhat similar and have a microstructure mainly consisting of upper bainite, with small fractions of acicular ferrite. Steel D further contains a fraction of lower bainite. Both steel A and D show clear prior austenite grain boundaries. The microstructure of Steel B consists of mostly acicular ferrite and granular bainite. The microstructure of steel C primarily consists of martensite with some upper bainite islands and clearly delineated prior austenite grain boundaries.

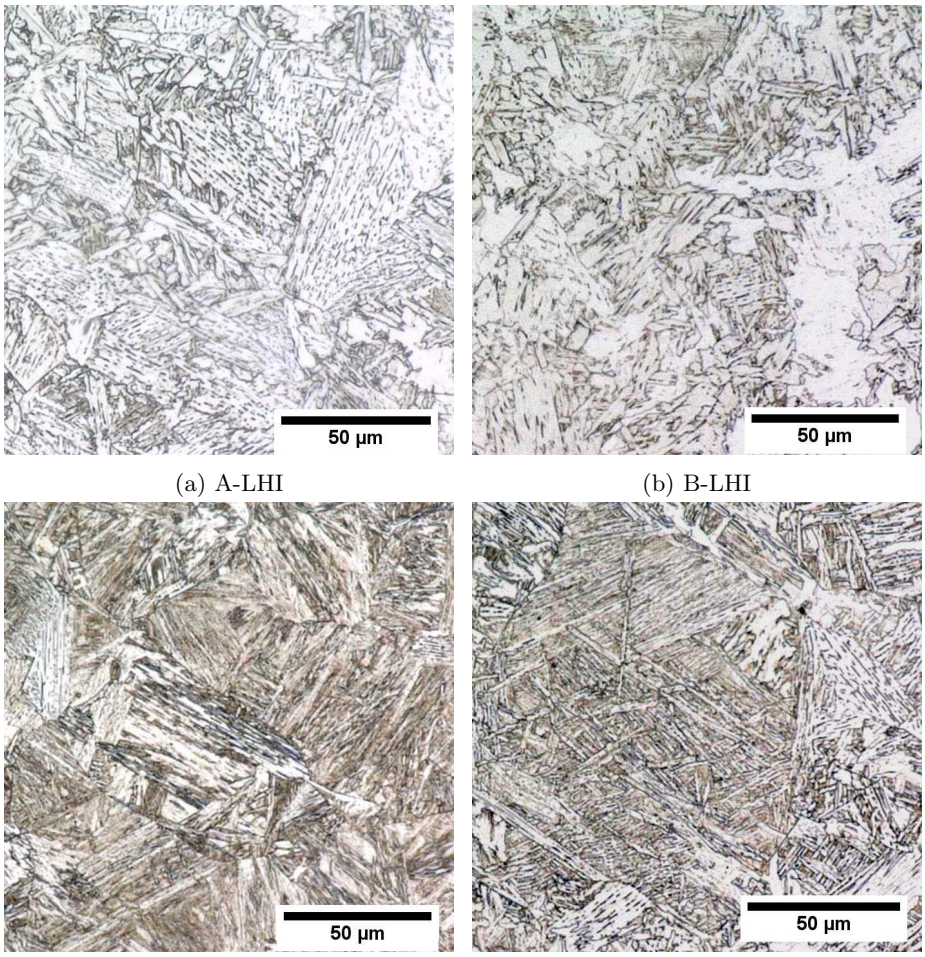

(a) A-LHI (b) B-LHI

(c) C-LHI (d) D-LHI

Figure 4.8: Micrograph of the CGHAZ for steel A-D for the LHI temperature cycle, etched with Nital 3%, 1000x magnification.

When the heat Input is increased and the IHI samples are considered, the microstructures of steel A, B and D appear very similar to that of the LHI cycle. The microstructure of steel C again consist of a mixture of lower and upper bainite.

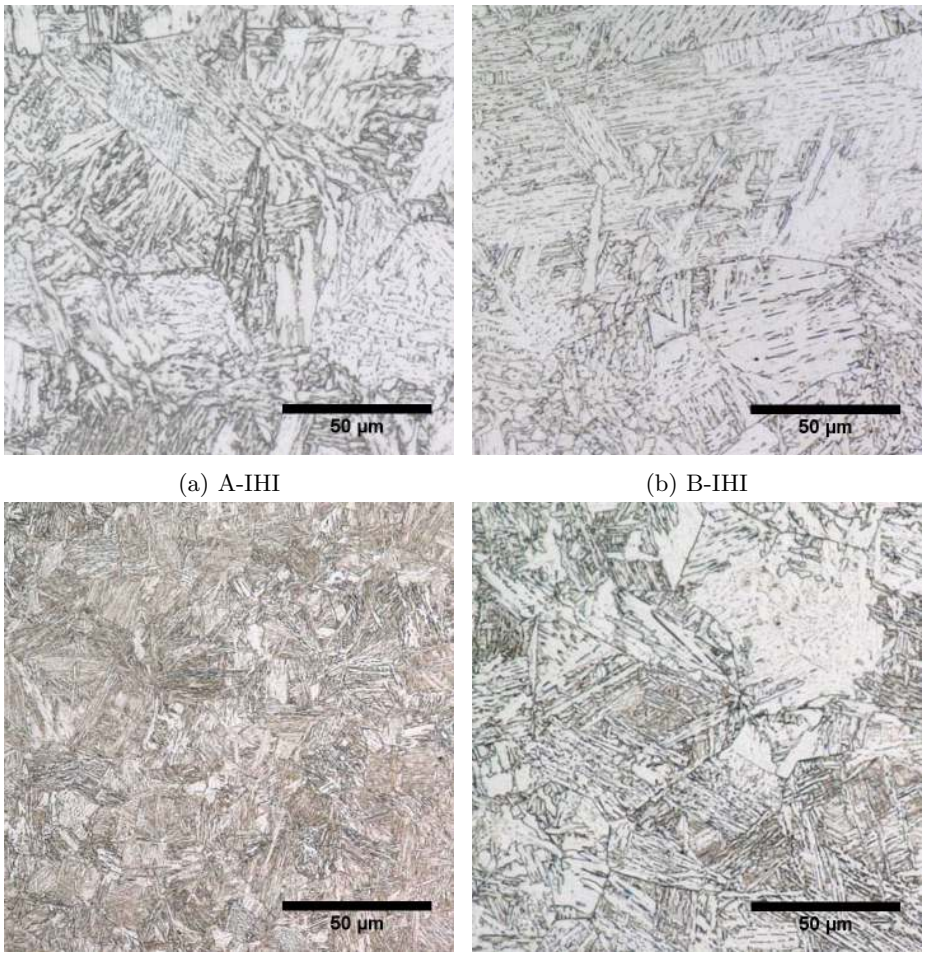

(a) A-IHI (b) B-IHI

(c) C-IHI (d) D-IHI

Figure 4.9: Micrograph of the CGHAZ for steel A-D for the IHI temperature cycle, etched with Nital 3%, 1000x magnification.

When the HHI temperature cycle is considered, some part of the microstructure of steel A are still upper bainite, the major fraction of the microstructure consists of granular bainite with elongated cementite islands. The microstructure of steel B for this cycle also consists of acicular ferrite, but with uniformly distributed spherical cementite particles. The microstructure of steel C is still mostly bainitic(upper and lower) and steel D consists of upper bainite, granular bainite and acicular ferrite. The Prior austenite grain boundaries are still clearly visible. These microstructures are shown in figure 4.10.

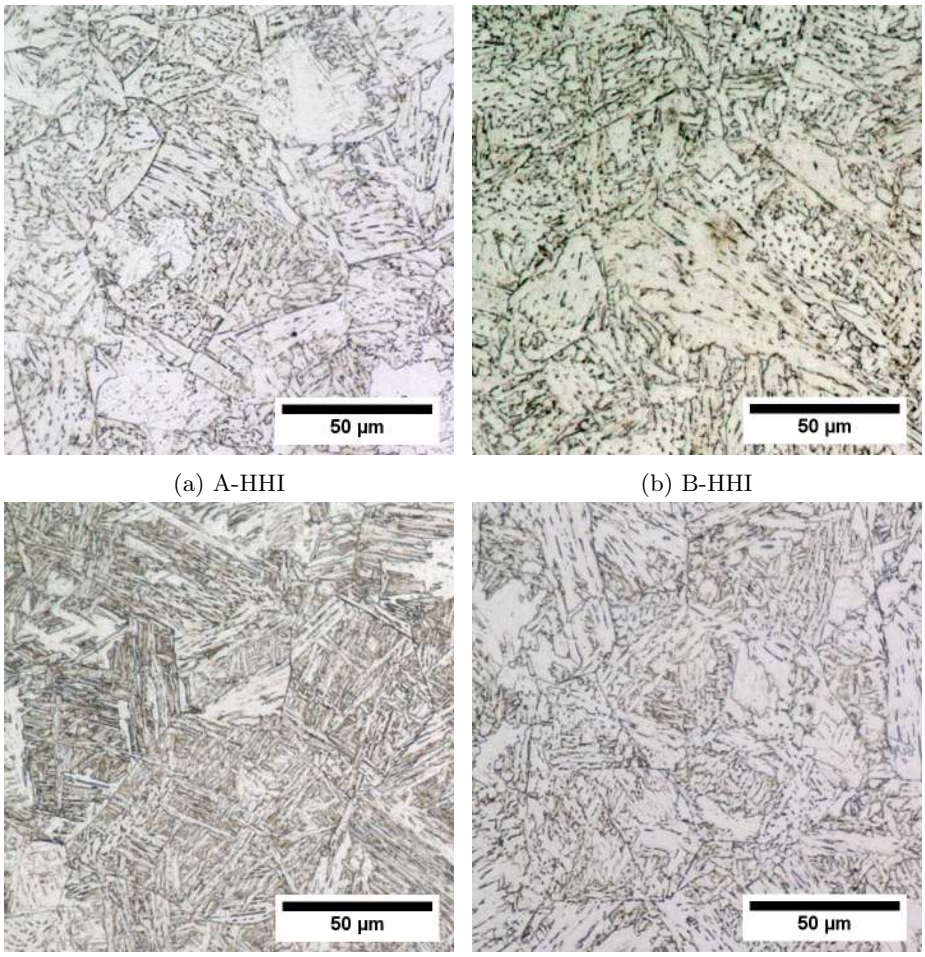

(a) A-HHI (b) B-HHI

(c) C-HHI (d) D-HHI

Figure 4.10: Micrograph of the CGHAZ for steel A-D for the HHI temperature cycle, etched with Nital 3%, 1000x magnification.

4.3.3 Reheated coarse-grained heat-affected zone

The CGHAZ was reheated to both 810 ˚C and 860 ˚C of which the resulting microstructures as observed after nital etching by optical microscopy will be discussed in this section.

Low heat input

The samples subjected to the LHI-810 temperature profile are shown in figure 4.11. Steel A and D both show a mixture of three different microstructural constituents. The main microstucture is composed of an acicular ferrite con-

stituent with relatively big grains containing no substructure and is hardly or not etched by nital(denoted by F in figure 4.11a) and upper bainite or granular bainite. A clear network of a separate constituent is shown, outlining the prior austenite grain boundaries, which is etched more by Nital. This constituent on the prior austenite grain boundaries is also found in the sample of steel C, but now the matrix microstructure consists fully of bainite. The prior austenite grain boundary consituent is not visible in the steel B sample, which consists of mostly acicular ferrite and granular bainite.

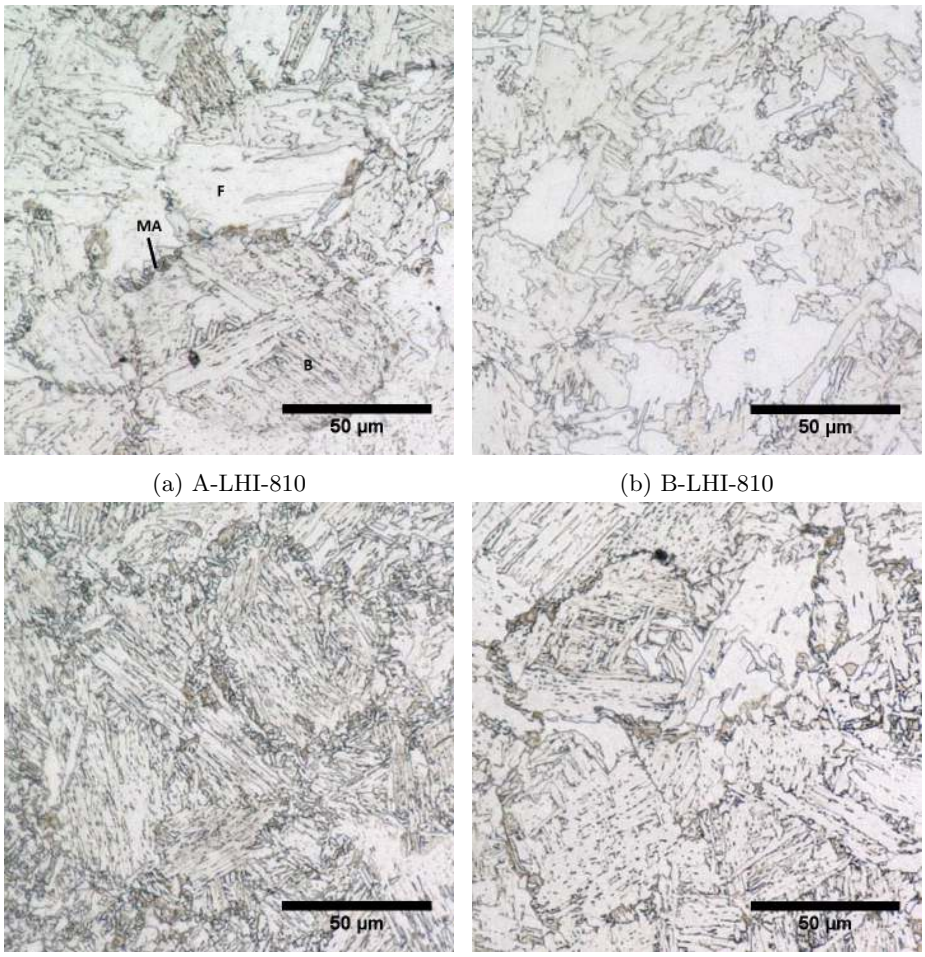

(a) A-LHI-810

(b) B-LHI-810

(c) C-LHI-810

(d) D-LHI-810

Figure 4.11: Micrograph of the CGHAZ for steel A-D for the LHI temperature cycle, etched with Nital 3%, 1000x magnification.

When the samples were etched with lepera's etchant, the grain boundary phase was clearly delineated for the samples reheated to 810 °C. These results, after

contrast enhancement, are shown in figure 4.12. The microstructure consists of a blocky, near connected M-A constituent located at the prior austenite grain boundaries and some stringer M-A constituent within the prior austenite grains.

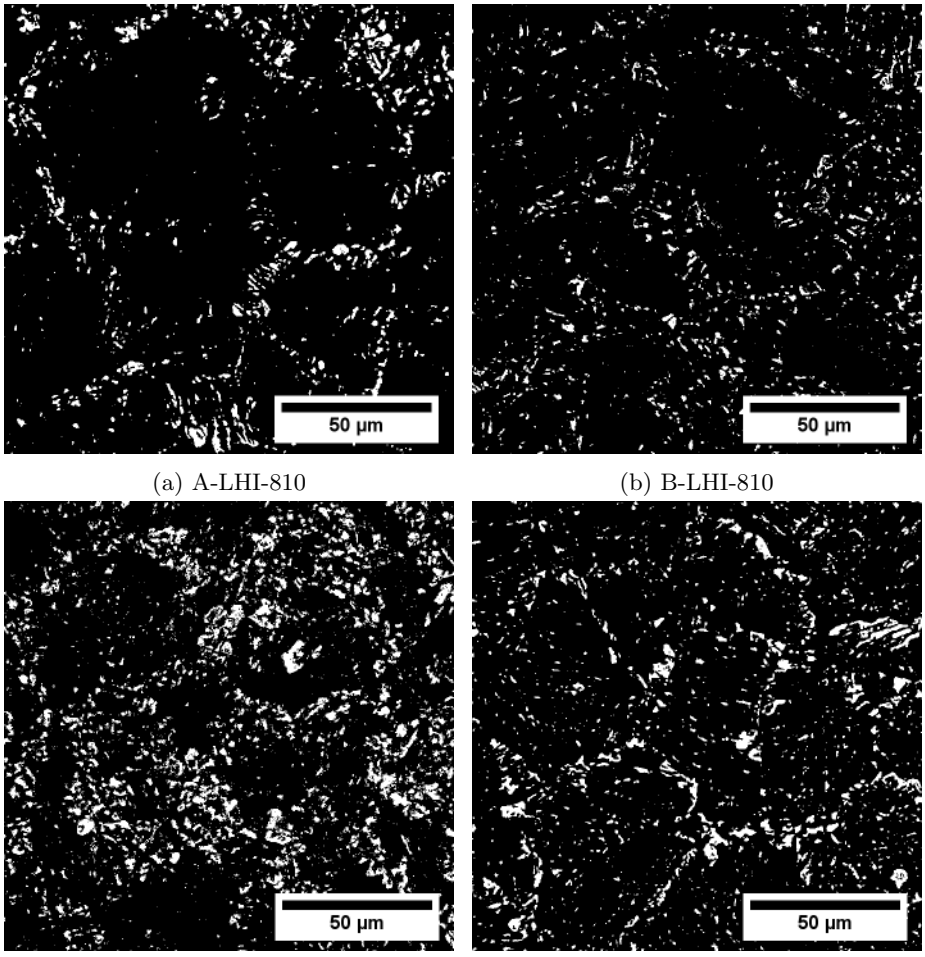

(a) A-LHI-810 (b) B-LHI-810

(c) C-LHI-810 (d) D-LHI-810

Figure 4.12: Micrograph of the CGHAZ for steel A-D for the LHI-810 temperature cycle, etched with Lepera's etchant, 1000x magnification. A brightness threshold has been applied in order to create sufficient contrast.

When the LHI-860 samples are etched with Nital, the M-A constituent along the prior austenite grain boundary is no longer present. A constituent, which is similarly etched, can however be found throughout the microstrucuture. Both the samples for steel A and B show an acicular ferrite microstrucuture very similar to the base metal microstructure, but without the pearlite islands. Steel C shows a microstructure with very small features and is no longer clearly bainitic

nor martensitic. Steel D still shows a bainitic structure (upper and granular) with relatively big acicular ferrite grains throughout. These microstructures are shown in figure 4.13 at a higher magnification than previous micrographs in order to show the microstructural features more clearly. When these samples are etched with Lepera's etchant M-A constituent are now homogeneously spread throughout the microstructure, which is illustrated by figure 4.14.

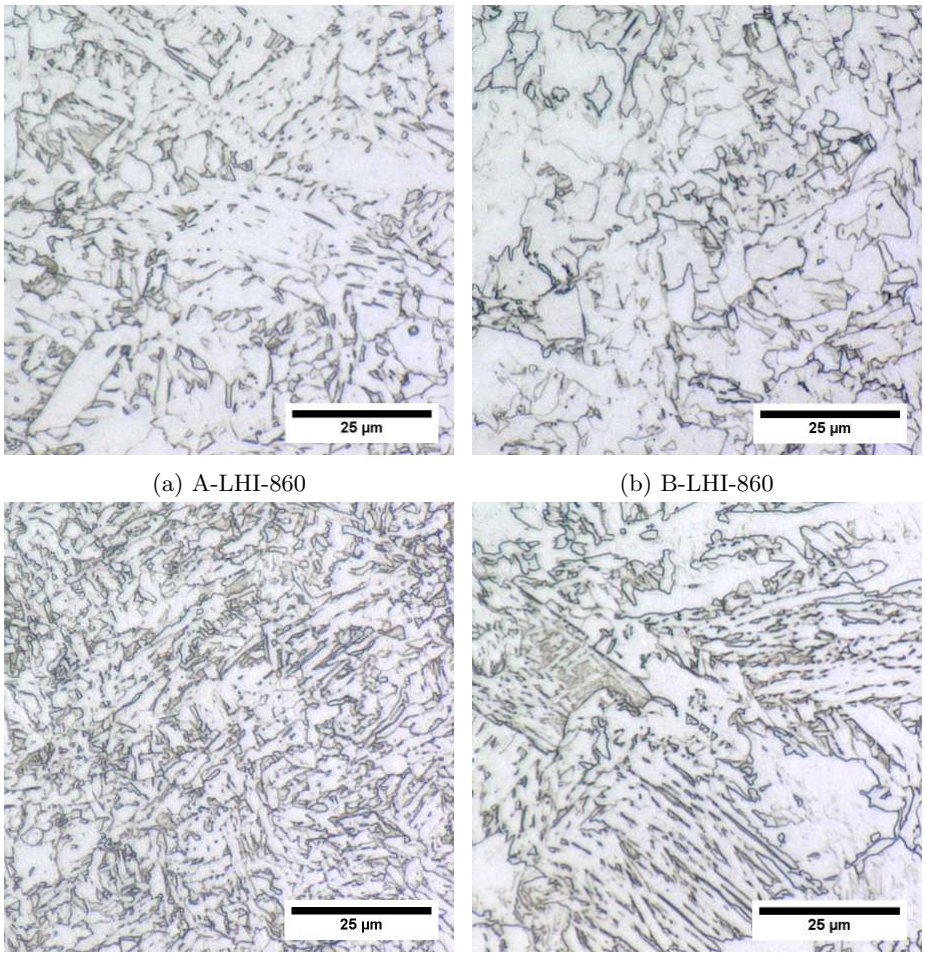

(a) A-LHI-860 (b) B-LHI-860

(c) C-LHI-860 (d) D-LHI-860

Figure 4.13: Micrograph of the CGHAZ for steel A-D for the LHI-860 temperature cycle, etched with Nital 3%, 2500x magnification.

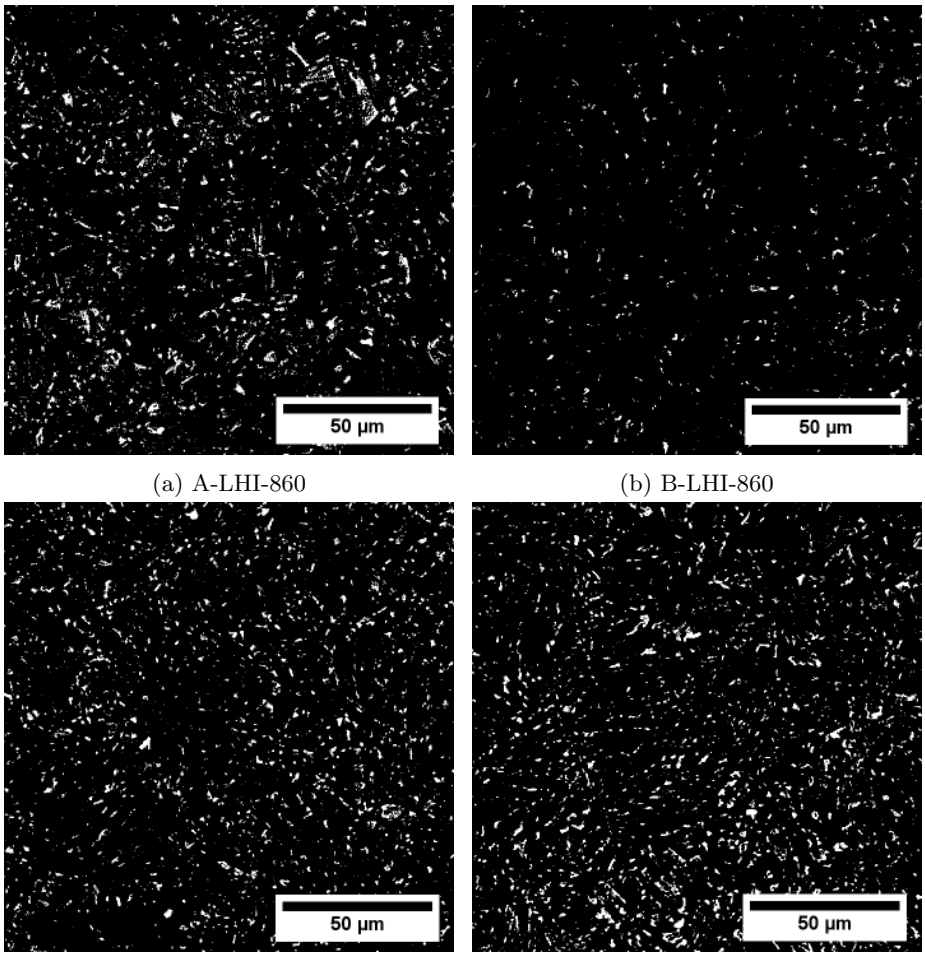

(a) A-LHI-860 (b) B-LHI-860

(c) C-LHI-860 (d) D-LHI-860

Figure 4.14: Micrograph of the CGHAZ for steel A-D for the LHI-860 temperature cycle, etched with Lepera's etchant, 1000x magnification. A brightness threshold has been applied in order to create sufficient contrast.

Intermediate heat input

The IHI samples reheated to 810 °Cof all steels look similar to the reheated LHI samples when etched by nital. The matrix microstructure of all the steels is the same, the prior austenite boundary constituent however is not as well defined as in the LHI-810 samples in steel A and D and no longer definable when steel B and C are considered. These microstructures, as etched with nital, are shown in figure 4.15.

When etched with Lepera's etchant, the M-A constituents allong the prior

austenite grain boundaries is not as clear as for the LHI-810 samples, especially when steels B and C are considered. The M-A constituents however are not uniformly distributed throughout the microstructure. These results are shown in figure 4.17.

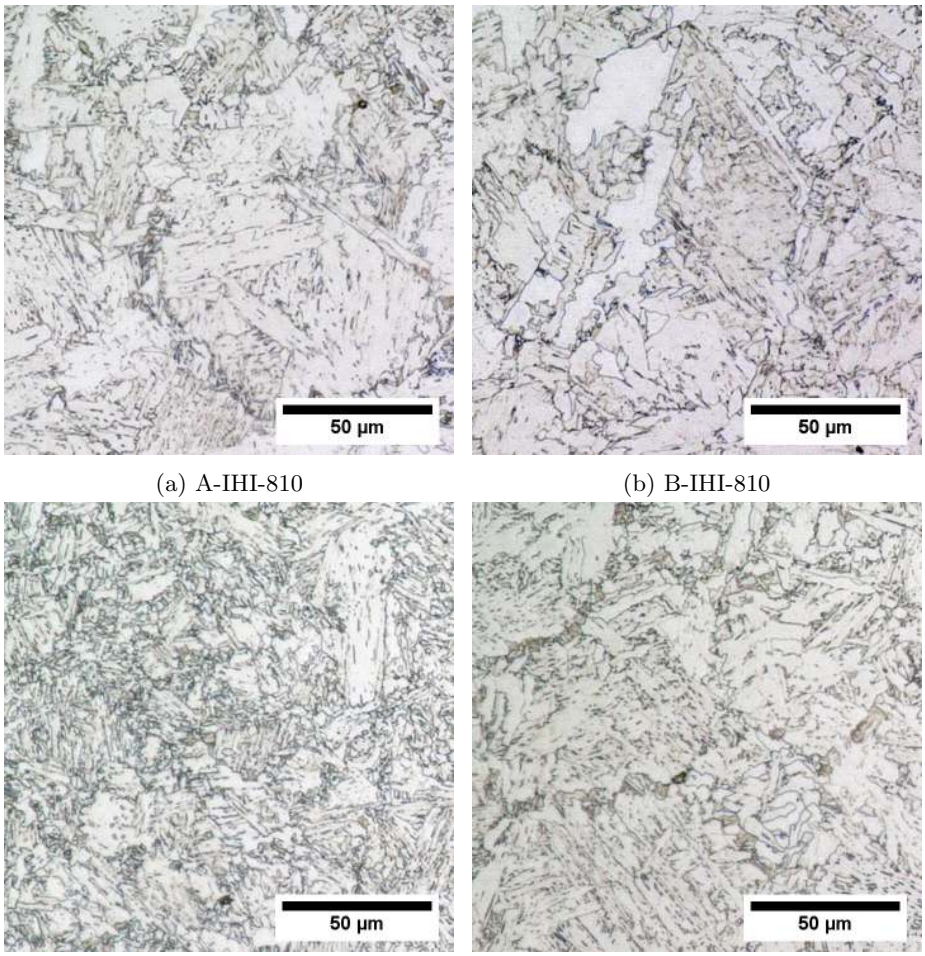

(a) A-IHI-810

(b) B-IHI-810

(c) C-IHI-810

(d) D-IHI-810

Figure 4.15: Micrograph of the CGHAZ for steel A-D for the IHI-810 temperature cycle, etched with Nital 3%, 1000x magnification.

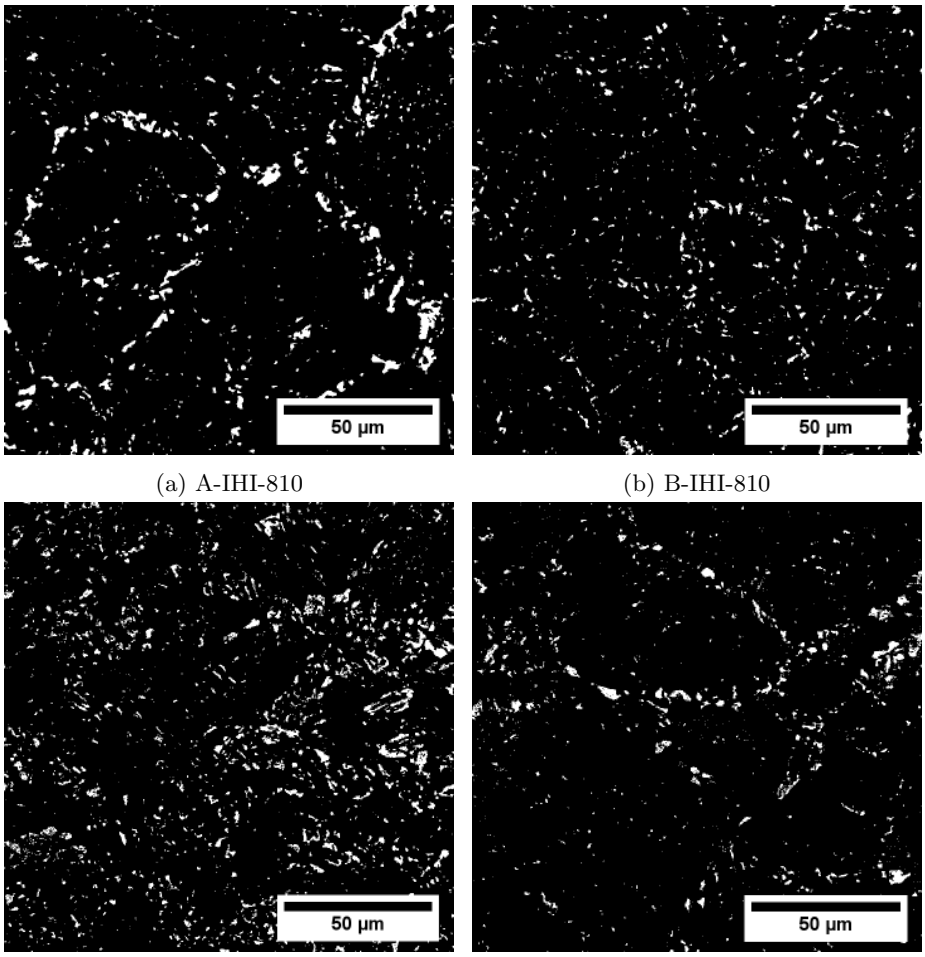

(a) A-IHI-810 (b) B-IHI-810

(c) C-IHI-810 (d) D-IHI-810

Figure 4.16: Micrograph of the CGHAZ for steel A-D for the IHI temperature cycle, etched with Lepera's etchant, 1000x magnification. A brightness threshold has been applied in order to create sufficient contrast.

The microstructures of the IHI-860 samples, which are shown in figure 4.17, consist mostly of acicular ferrite and granular bainite. The microstructure constituent which was etched more heavily was again found, as with the LHI-860 samples. The results when etched with Lepera's etchant are essentially the same as in figure 4.14 but with a smaller fraction of M-A constituents (fractions will be discussed in section 4.3.4).

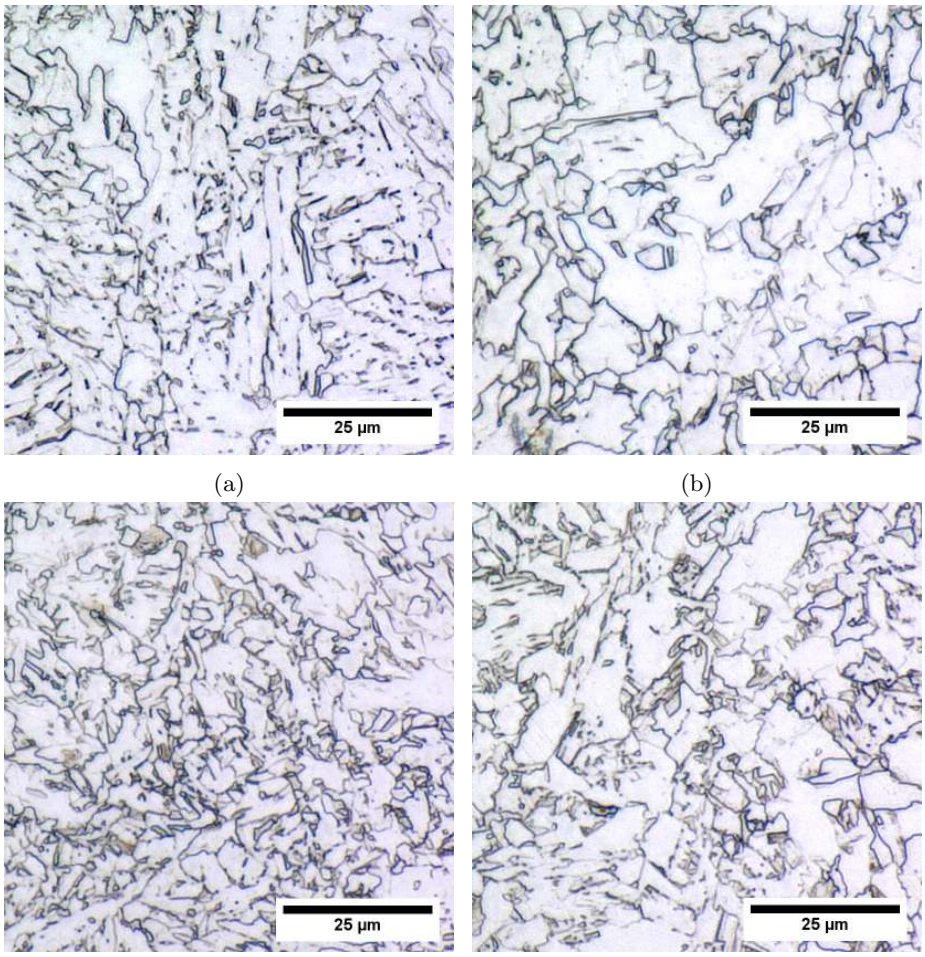

(a) (b)

(c) (d)

Figure 4.17: Micrograph of the CGHAZ for steel A-D for the IHI-860 temperature cycle, etched with Nital 3%, 2500x magnification.

High heat input

The microstructures of the HHI-810 samples no longer contain a prior austenite grain boundary constituent which is visible when etched with nital. The sample of steel B consist mostly of polygonal ferrite with some regions which are etched somewhat darker. Steel A and D consist of granular bainite and acicular ferrite. The cementite particles are elongated for steel D and less so for steel A. These clear cementite particles are not found in the sample of steel C, which also has a acicular ferrite and granular bainite microstructure. These microstructures are shown in figures 4.18 and 4.19. Lepera's etchant reveals the M-A constituents to be still concentrated at the prior austenite grain boundaries for steel A,C and

D but not for steel B. This is shown in figure 4.20. These prior austenite grain boundaries however are not as discernible as was the case for the other heat inputs. Note that the prior austenite grains for the samples of steel D appear larger in size than those of the others.

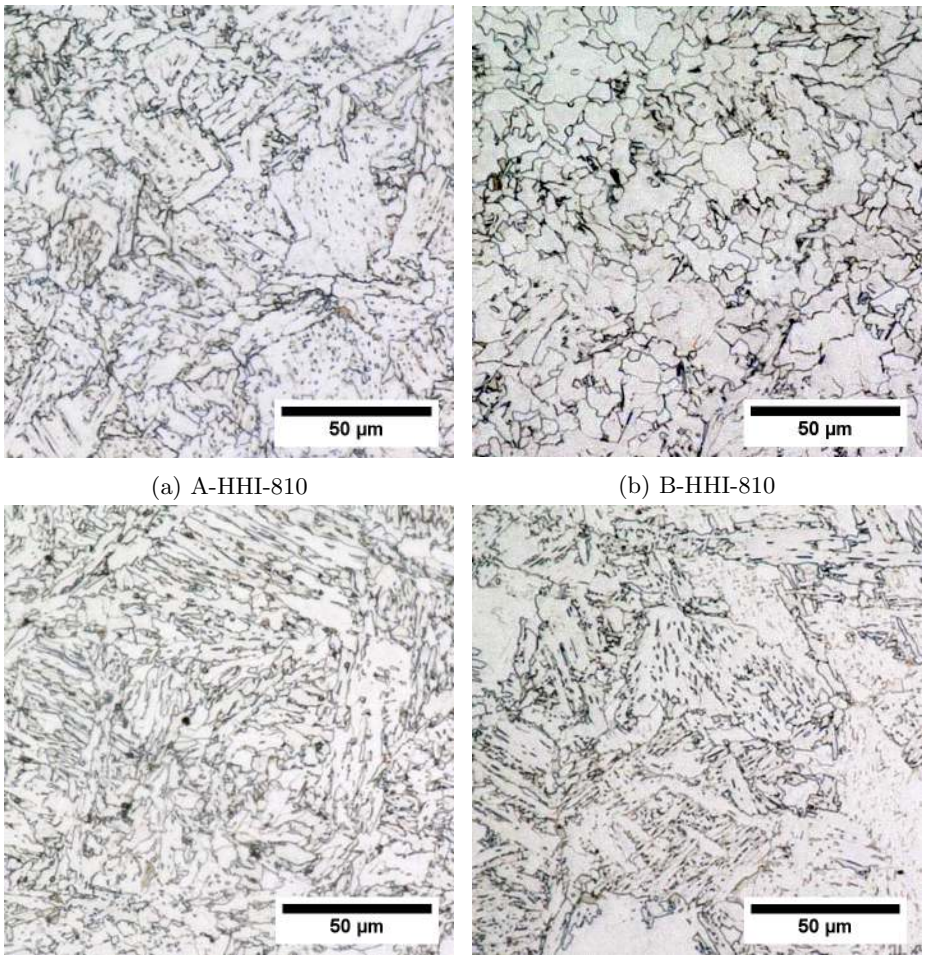

(a) A-HHI-810 (b) B-HHI-810

(c) C-HHI-810 (d) D-HHI-810

Figure 4.18: Micrograph of the CGHAZ for steel A-D for the HHI-810 temperature cycle, etched with Nital 3%, 1000x magnification.

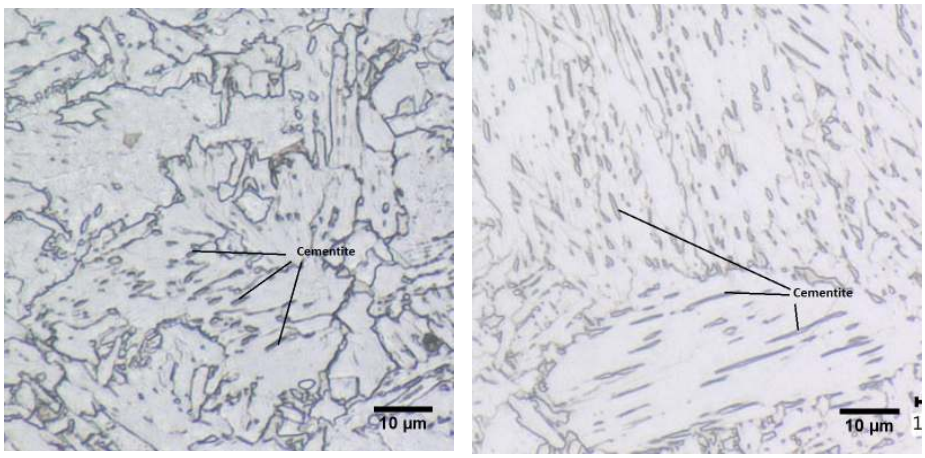

(a) A-HHI-810

(b) D-HHI-810

Figure 4.19: Micrograph of the CGHAZ for steel A and D for the HHI-810 temperature cycle, etched with Nital 3%, the cementite particles are highlighted 2500x magnification.

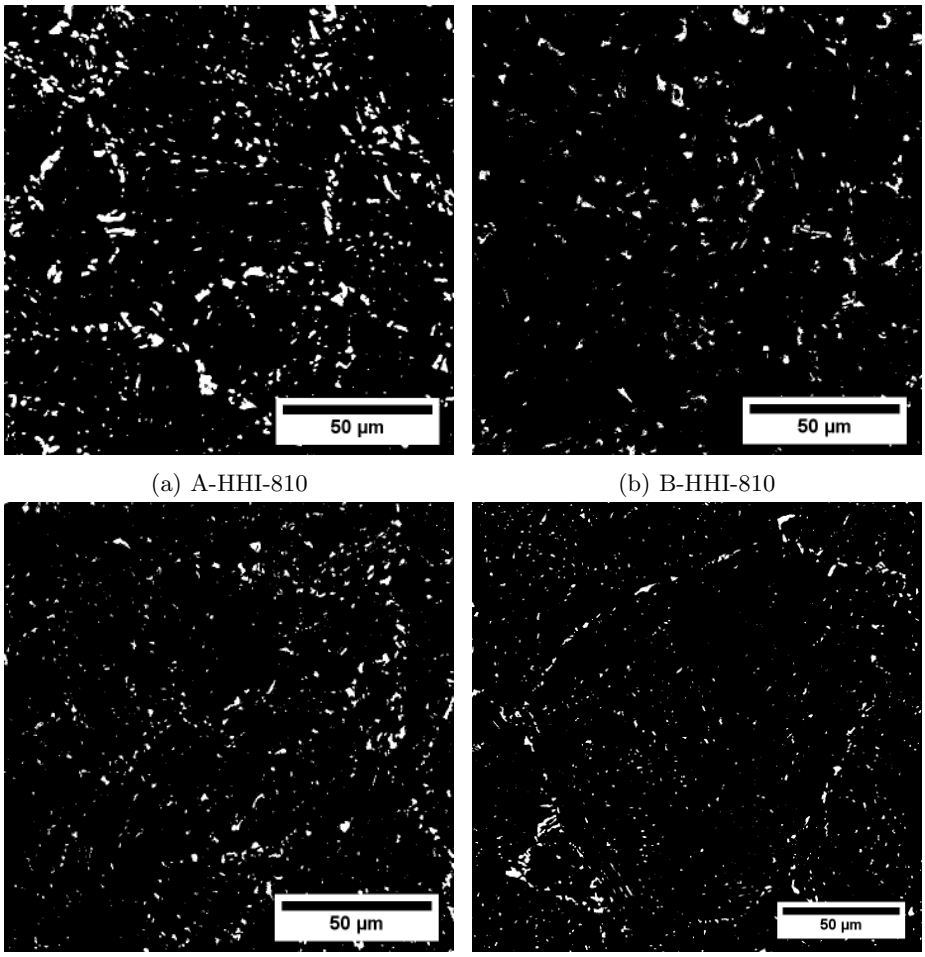

(a) A-HHI-810 (b) B-HHI-810

(c) C-HHI-810 (d) D-HHI-810

Figure 4.20: Micrograph of the CGHAZ for steel A-D for the HHI temperature cycle, etched with Lepera's etchant, 1000x magnification. A brightness threshold has been applied in order to create sufficient contrast.

The microstructures of the steel subjected the HHI-860 temperature profile are shown in figure 4.21 as etched by nital. Steel A and B have an acicular ferrite microstructure. Steel B shows small areas of pearlite and steel A shows cementite particles, which seem to be concentrated along the ferrite grain boundaries, but this cannot be clearly resolved by Nital etching and optical microscopy. Steels C and D show an acicular ferrite and granular bainite microstructure with distributed cementite particles, which are elongated in steel D.

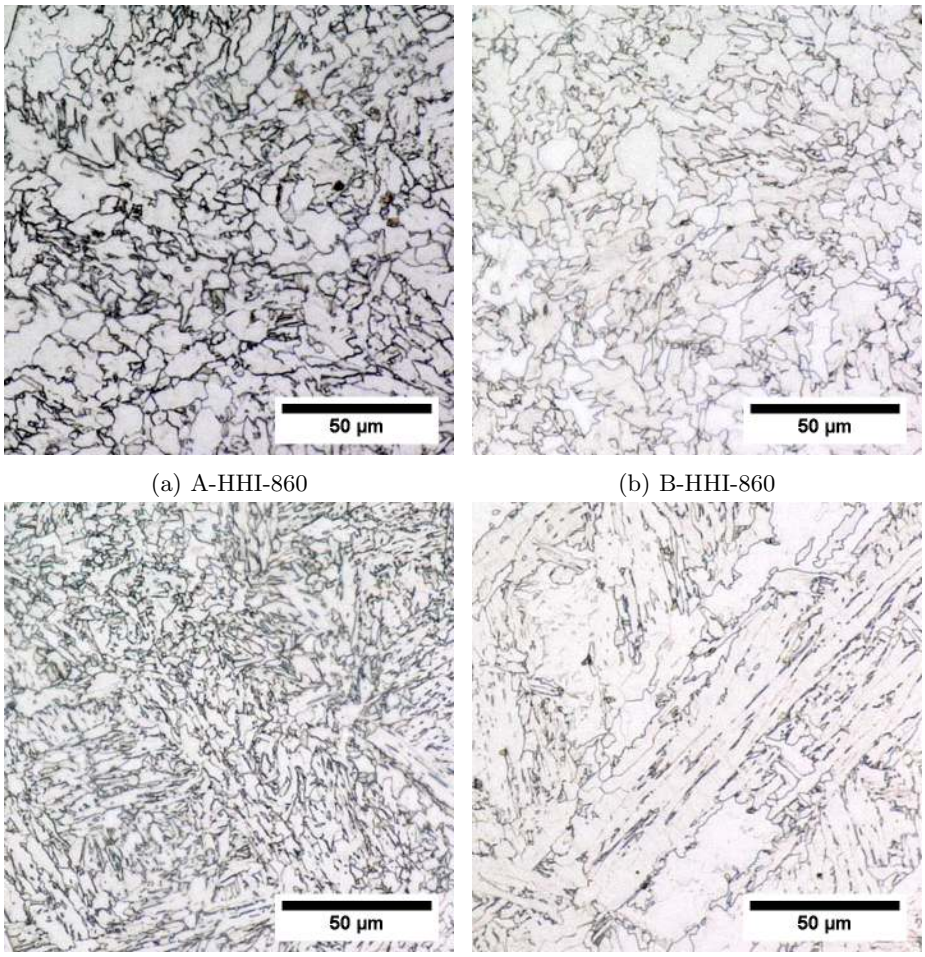

(a) A-HHI-860 (b) B-HHI-860

(c) C-HHI-860 (d) D-HHI-860

Figure 4.21: Micrograph of the CGHAZ for steel A-D for the HHI-860 temperature cycle, etched with Nital 3%, 1000x magnification.

4.3.4 Lepera quantification.

All reheated samples were etched with Lepera's etchant and the result was analysed using ImageJ software. For this particle analysis, particles with a size less than 0.1 μm^2 were discarded, in order to discard measurements of individual pixels. The fraction and average size of M-A constituents found for all Gleeble simulated samples are shown in figures 4.22 to 4.24 where the denomination of the samples has been shortened.

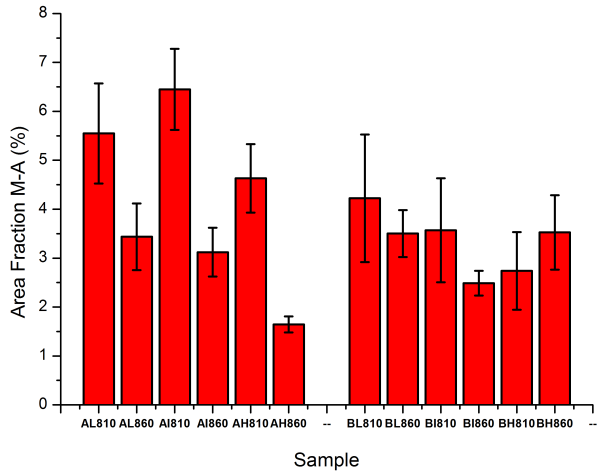

Figure 4.22: Area fraction of M-A for samples of steels A and B, the denomination has been shortened (A-LHI-810 is shortened to AL810 etc.) Error bars denote the standard deviation of the measurements.

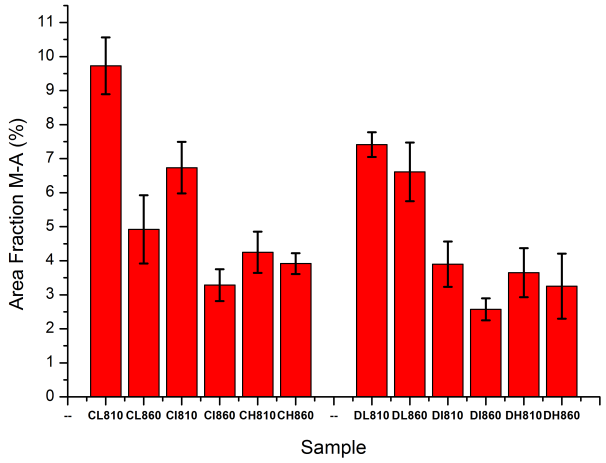

Figure 4.23: Area fraction of M-A constituents for samples of steels C and D, the denomination has been shortened (C-LHI-810 is shortened to CL810 etc.) Error bars denote the standard deviation of the measurements.

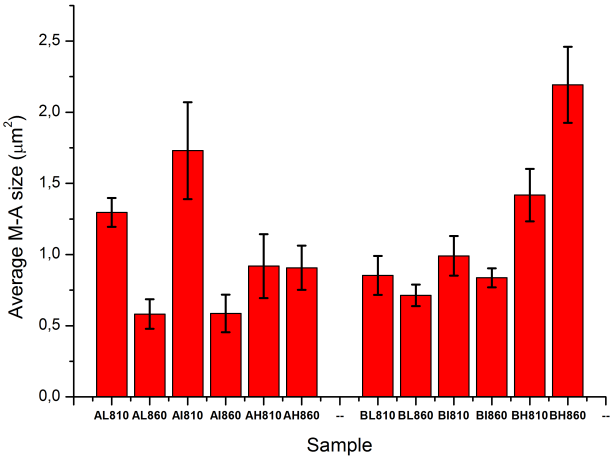

Figure 4.24: Average size of M-A for samples of steels A and B, the denomination has been shortened (A-LHI-810 is shortened to AL810 etc.) Error bars denote the standard deviation of the measurements.

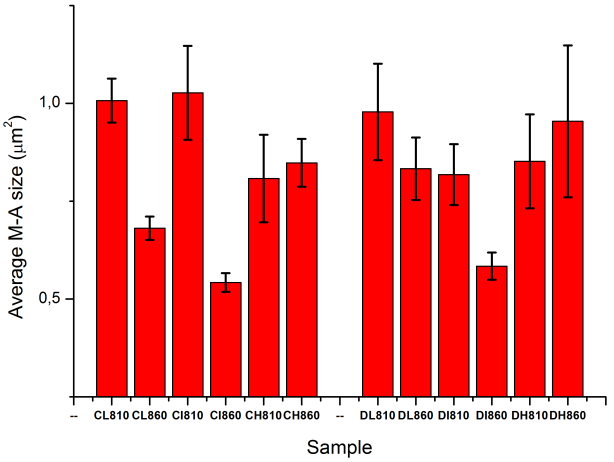

Figure 4.25: Average size of M-A constituents for samples of steels C and D, the denomination has been shortened (C-LHI-810 is shortened to CL810 etc.) Error bars denote the standard deviation of the measurements.

4.3.5 Actual weld

Only of steel A an actual weld was available for study. The weld was created by a laboratory weld process and not from the actual welding procedure. The heat input can therefore not be compared to the ones discussed in this work. The microstructure of the CGHAZ for an actual weld in steel A is shown in figure 4.26. In the discussion chapter this microstructure will be compared to the simulated microstructures.

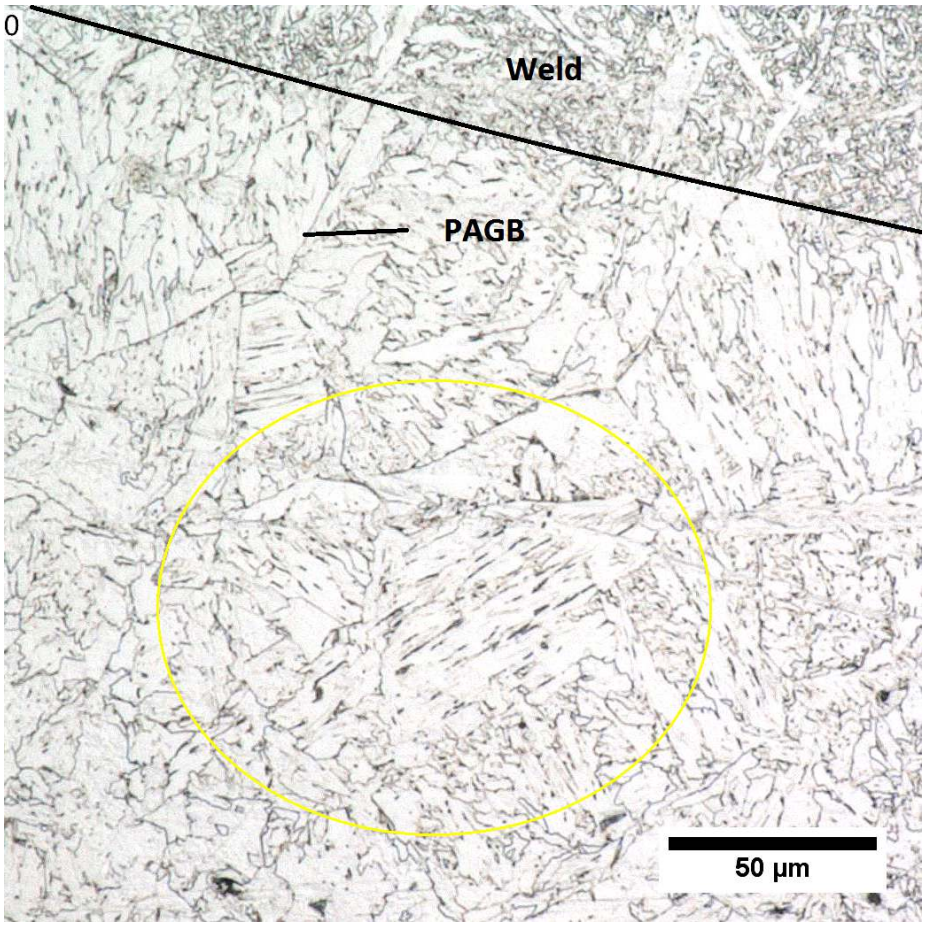

Figure 4.26: Micrograph of an actual weld, black line shows the fusion line and the prior austenite grain boundary(PAGB) is denoted. The yellow circle shows a microstructure comparable to A-HHI.

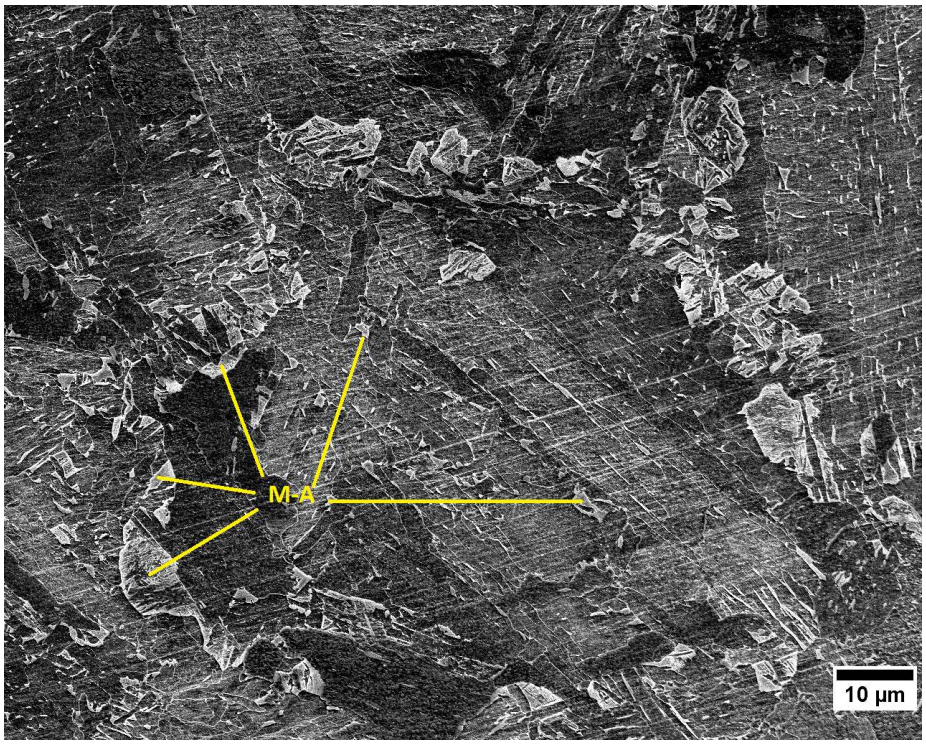

Figure 4.27: Secondary electron image of A-LHI-810 showing M-A cosititutuents located at the prior austenite grain boundary at a magnification of 1000×.

4.4 Electron Microscopy

Secondary electron images made from the A-LHI-810 sample are shown in figures 4.27 and 4.28. The sample was unfortunately not prepared very well and the parallel line which are visible at around a 16° angle to the horizontal are scratches. The internal structure of the big M-A constituents is etched just like the surrounding ferrite, but the boundary region is not, which is identified as martensite. Both a secondary electron image and backscatter electron image of a region with M-A constituents is shown in figure 4.29.

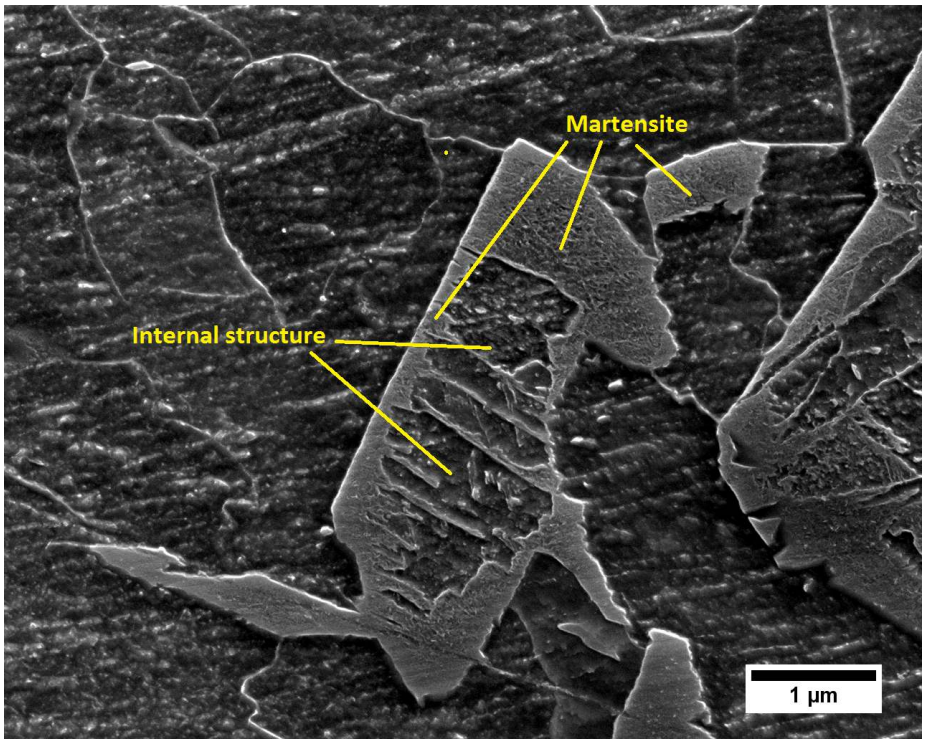

Figure 4.28: Secondary electron image of A-LHI-810 showing a M-A particle at a magnification of 16000×.

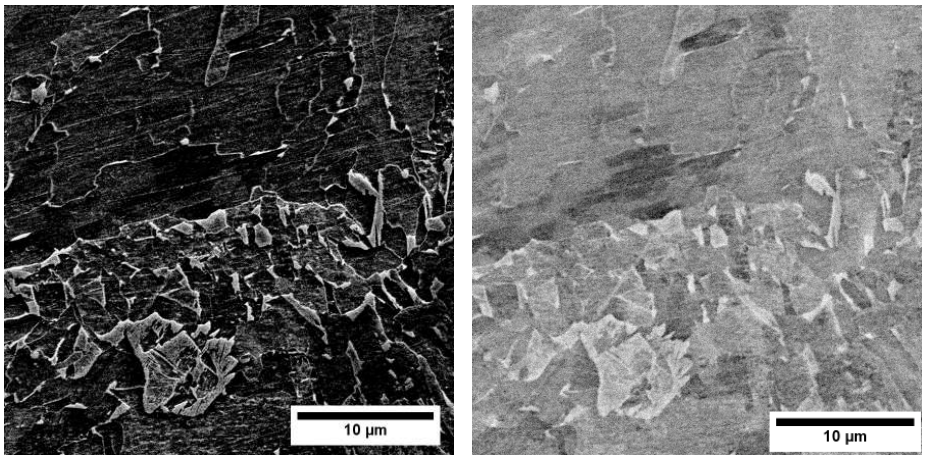

(a) (b)

Figure 4.29: (a) Secondary and (b) backscatter electron image of A-LHI-810 showing M-A constituents at a magnification of 2500×.

4.5 Electron backscatter diffraction

EBSD measurements were done on the following samples: the base metal of steel A (A-BM), A-LHI-810, A-LHI-860, A-HHI-810, A-HHI, D-LHI-810 and D-LHI-860. The measurement parameters are shown in table 4.2. Maps of the EBSD scans can be found in appendix C.

Table 4.2: Parameters used for the EBSD measurements.

Sample	Step size (µm)	Area (µm)
A-BM	0.20	220 × 250
A-LHI-810	0.10	250 × 240
A-LHI-860	0.10	240 × 230
A-HHI-810	0.15	280 × 270
A-HHI	0.15	280 × 270
B-LHI-810	0.15	320 × 310
B-LHI-860	0.15	250 × 240

A inverse pole figure representation of the scan of the base metal of steel A is shown in figure 4.30, revealing the acicular ferrite microstructure.

4.5.1 Phase and microstructure constituent quantification.

The EBSD measurements done, can discern a phase difference between the fcc phase, austenite and the bcc phase, ferrite. The difference in diffraction

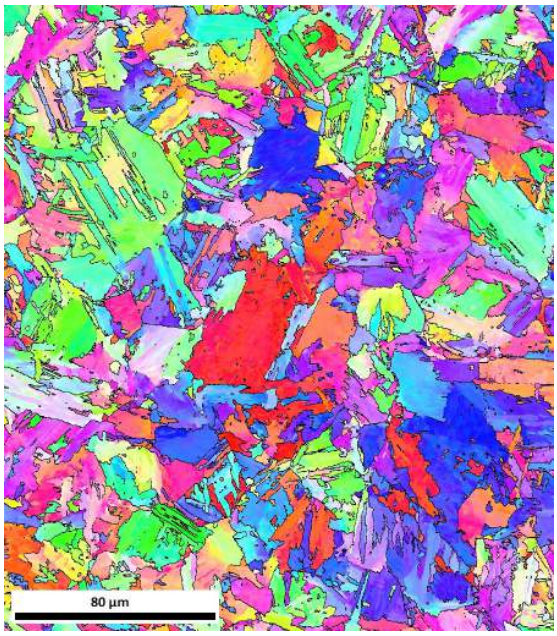

Figure 4.30: Inverse pole figure of the EBSD scan performed on the base metal of steel A. Black lines represent high angle grain boundaries.

pattern between bct martensite and bcc ferrite is however too small to measure using EBSD. Therefore the method described in section 3.5 using the image quality is used to quantitatively describe the microstructure constituents. For the quantification points with an CI lower than 0.05 were deemed unreliable and discarded.

CGHAZ

In order for austenite to be measured, it had to consist of at least 3 measurement points and have an average CI of above 0,05. The fraction of austenite for all samples was found well below 0.1 %.

The area shown in figure 4.31 is used for the quantification of the microstructure. The middle grain on the line was identified as martensite and the IQ of this grain was used as a threshold for grains to be identified as martensite. The thresholds for the lowest IQ were chosen lower than 1650. The IQ map of the grains with a average IQ within these boundaries, is shown in figure 4.32, which is 3.2 %of the total scan. Not all of the austenite which has formed in the second heating cycle transforms to Martensite, but the angles between two grains transformed from the same autenite grain have a minimum misorientation angle of 10.5 °. Therefore, to obtain a grain average IQ, the threshold for the grain construction was set to 10°[13]. The fraction of this microstructure

constituent is very much dependent on the threshold value chosen which can make a difference of 3 % for a variation of 100 in the IQ. One of the areas for the threshold value of 1650 is shown in figure 4.33 with the grain boundaries, which satisfy the K-S and N-W orientation relation, highlighted.

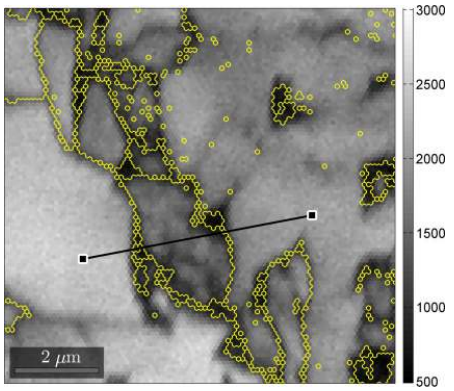

(a)

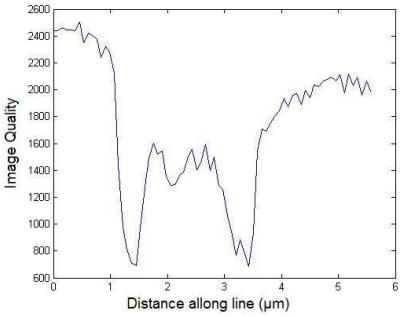

(b)

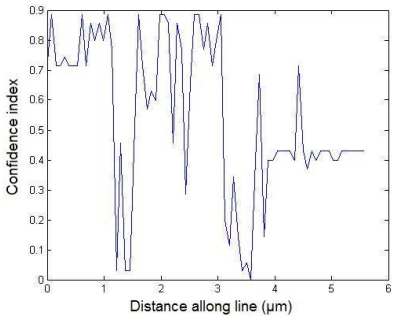

(c)

Figure 4.31: (a) IQ map used for the quantive description of the microstructure (b) Confidence index and (c) Image quality profile along the line in (a)

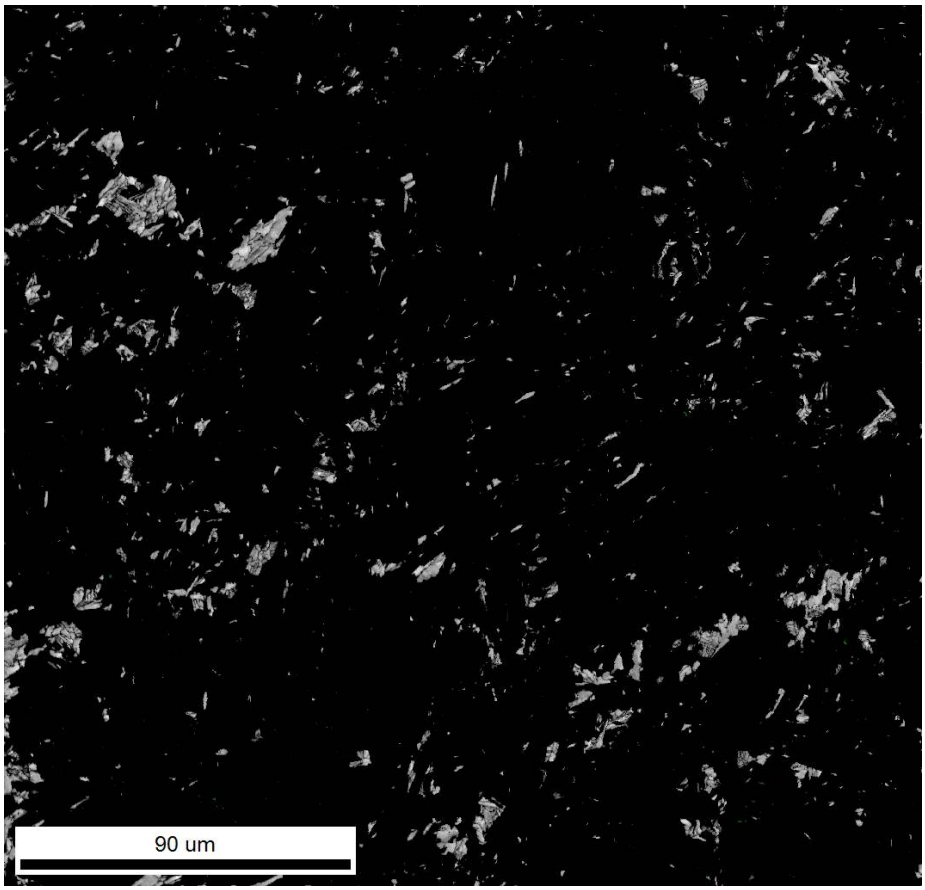

Figure 4.32: Image quality map of A-LHI-810 with QI threshold set to IQ<1650.

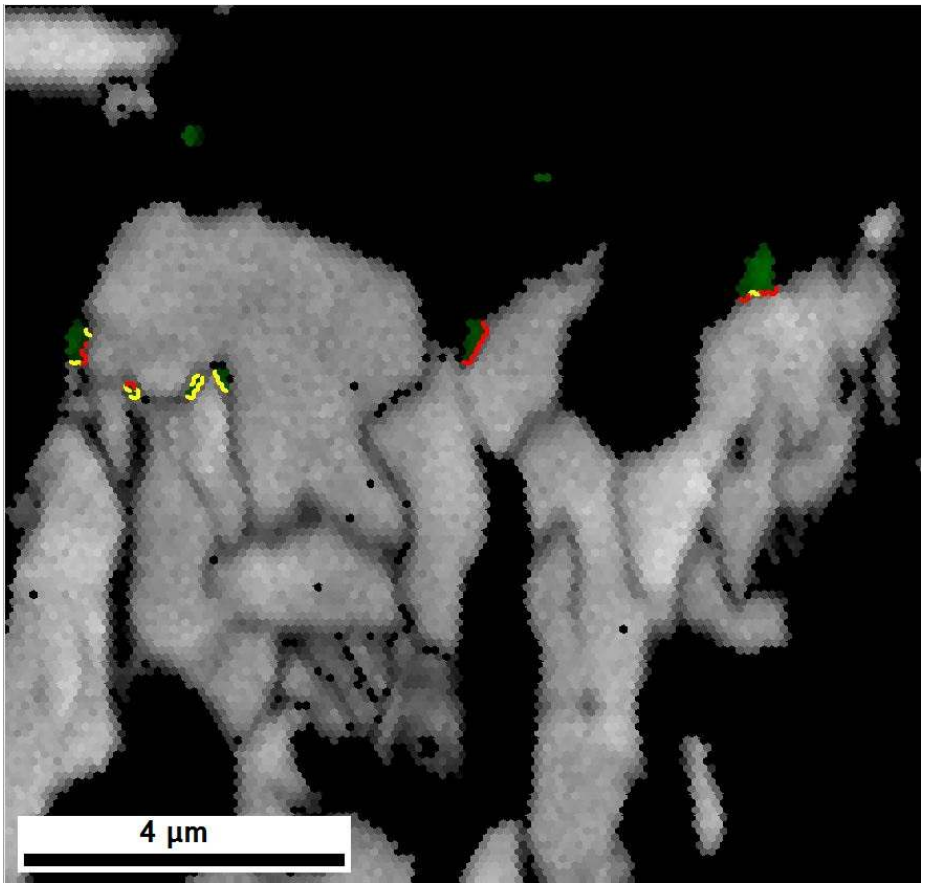

Figure 4.33: A small area in figure 4.32 with austenite shown in a green color. The grain boundaries between austenite and ferrite which satisfy the K-S relationship are highlighted in red and the boundaries which satisfy the N-W are highlighted in yellow.

The fraction of a certain microstructural constituent was also determined by the method described by Wu et al.[81], without performing the normalization as it does not yield different results for the fractions. For A-LHI-810 and B-LHI-810 this is shown in figures 4.34 and 4.35, in which the area fractions are denoted. A good fit was found for a summation of 3 Gaussian curves, with a R^2 value of 0.9999 and 0.9998, respectively. This fit is based on the assumption that the microstructure consists of three constituents and measurement point with an CI lower than 0.05 were discarded. This procedure was performed on data from all EBSD scans, the results are shown in table 4.3, the fit with the highest R^2 was accepted as the best fit. The names given to the microstructural constituents in the graphs are to denote the difference in dislocation density, the exact microstructural constituent is not clear from the IQ distribution themselves and

Table 4.3: Fractions of microstructural constituents found by fitting a sum of Gaussian curves to IQ data obtained from the EBSD scans.

Sample	Ferrite	Bainite	Martensite	R^2 of fit
A-BM	0.756	0.235	0.007	0.9996
A-LHI-810	0.852	0.107	0.040	0.9999
A-LHI-860	0.766	0.215	0.018	0.9998
A-HHI-810	0.885	0.077	0.038	0.9998
A-HHI	0.771	0.226	0.003	0.9998
D-LHI-810	0.398	0.543	0.058	0.9998
D-LHI-860	0.697	0.277	0.026	0.9997

this has to be related to results from optical microscopy and maps generated from the EBSD results.

Another process which is employed, consist of fitting two Gaussian curves to the measured IQ values. These two Gaussians for A-LHI-810 are shown in figure 4.36. Using the average of the small Gaussian as the maximum average IQ (1692) threshold value for the M-A constituents yields an M-A constituent fraction of 5.1 %.

The M-A constituents identified by this last method do not always contain austenite (in fact, mostly they don't). In order to make the reverted austenite areas visible, and thus to identify the M-A constituents the orientation relations from table 2.6 were used. A result of this is shown in figure 4.37. The threshold angle which were used for the applications of these relations was set to 10°.

The same process using the summation of two Gaussian curves for microstructure quantification was performed on all the samples, the results are shown in table 4.4. The sample of A-LHI-860 contained a large amount of scratches, lowering the average IQ of certain grains significantly.

Table 4.4: Fraction (in %) of M-A constituents as derived from EBSD measurements.

Sample	Gaussian method	Visual method
A-LHI-810	5.1	3.2
A-LHI-860	10.2	-
A-HHI-810	0.5	-
A-HHI	0.6	-
D-LHI-810	7.9	5.5
D-LHI-860	3	4.2

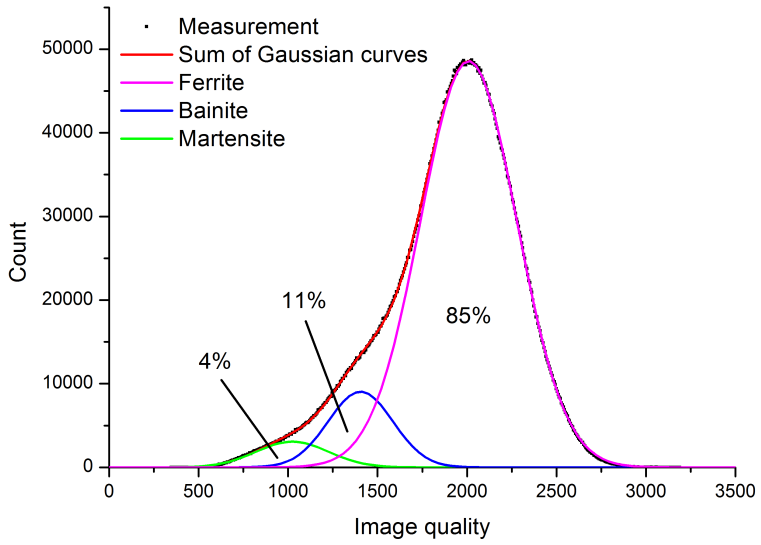

Figure 4.34: Gaussian fits to the IQ distribution of A-LHI-810 with the area fractions denoted.

4.5.2 Grain boundaries.

To describe the grain boundaries, the fraction of high angle grain boundaries (hagb) and low angle grain boundaries (lagb) were analysed. The thresholds were set to $2^\circ \leq \theta \leq 15^\circ$ and $\theta \geq 15^\circ$ for lagb and hagb respectively, where θ is the misorientetion angle between two grains. The results of this analysis are shown in table 4.5.

Table 4.5: Fraction of high angle grain boundaries as measured by electron backscatter diffraction.

Sample	Fraction HAGB
BM-A	0.65
A-LHI-810	0.69
A-LHI-860	0.75
A-HHI-810	0.73
A-HHI	0.65
B-LHI-810	0.71
B-LHI-860	0.77

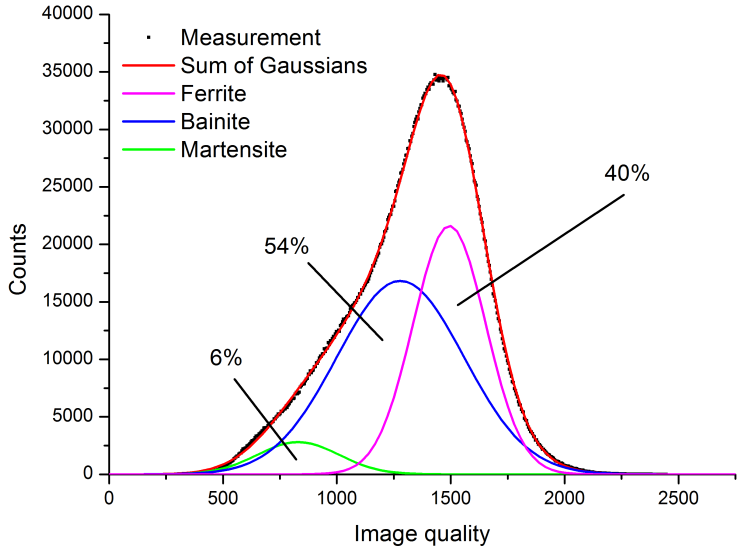

Figure 4.35: Gaussian fits to the IQ distribution of D-LHI-810 with the area fractions denoted.

4.6 Hardness

4.6.1 Macro hardness

Hardness was measured for all gleeble simmulated samples as well as the base metal, at both the half thickness and the edge. No difference in the hardness of the base metal was observed between the two edges of the pipe wall. The results are shown in figures 4.38 to 4.41 . Hardness was measured at at least 18 points across the whole surface. A complete list of measured hardness can be found in appendix A. The indents were bigger than 49 µmin diameter for all measurements with a load of 500g.

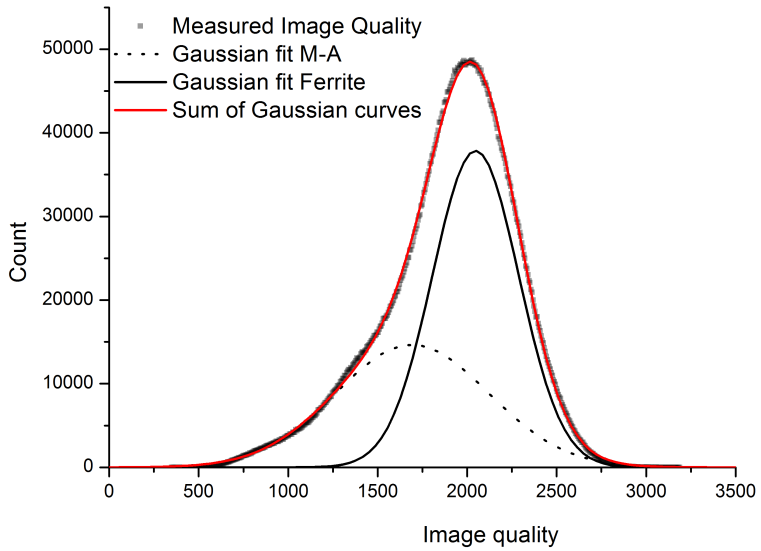

Figure 4.36: Gaussian fits to the IQ distribution of D-LHI-810

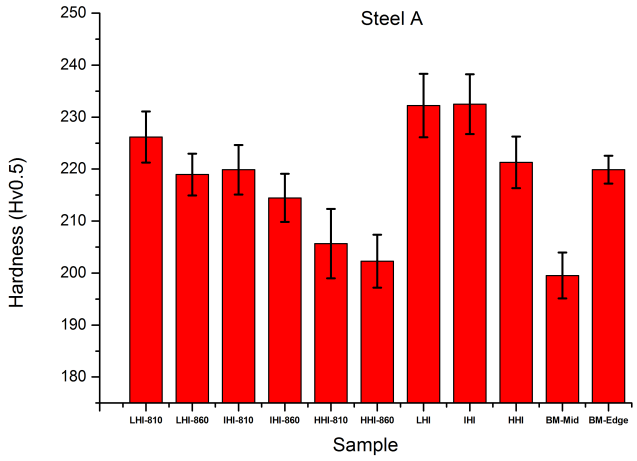

Figure 4.38: Hardness measured for all Gleeble samples and base metal of steel A, error bars are the standard deviation of the measurements.

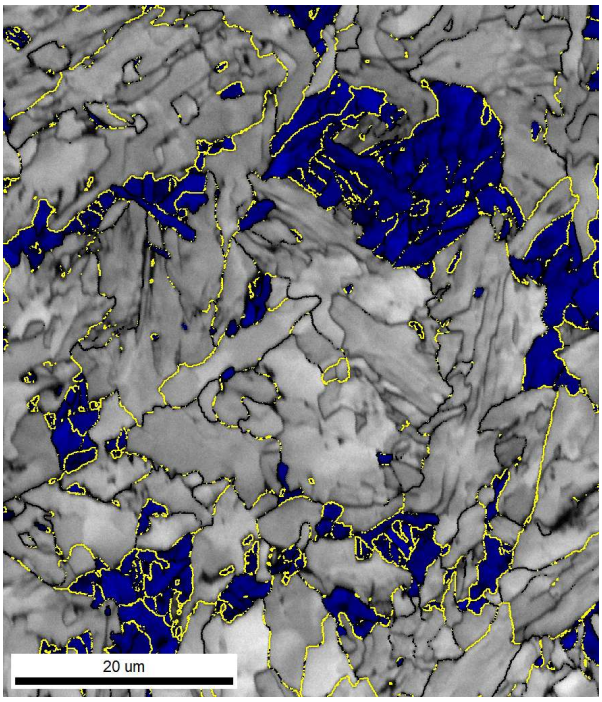

Figure 4.37: Image quality map of part of the measurement on A-LHI-810 with the M-A constituents highlighted blue, the grain boundaries larger than 10 ˚are yellow and the black grain boundaries satisfy the relations from table 2.6

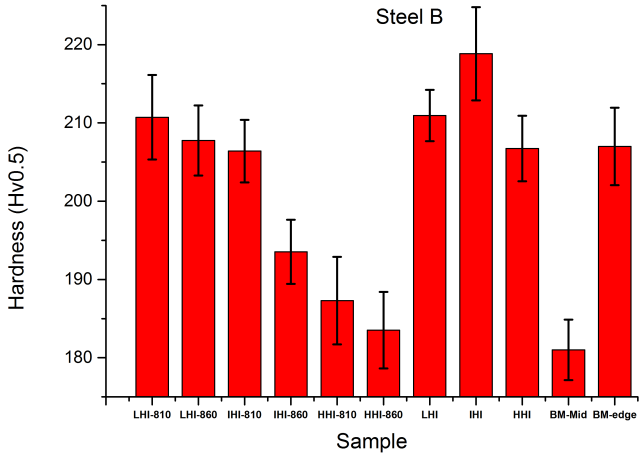

Figure 4.39: Hardness measured for all Gleeble samples and base metal of steel B, error bars are the standard deviation of the measurements.

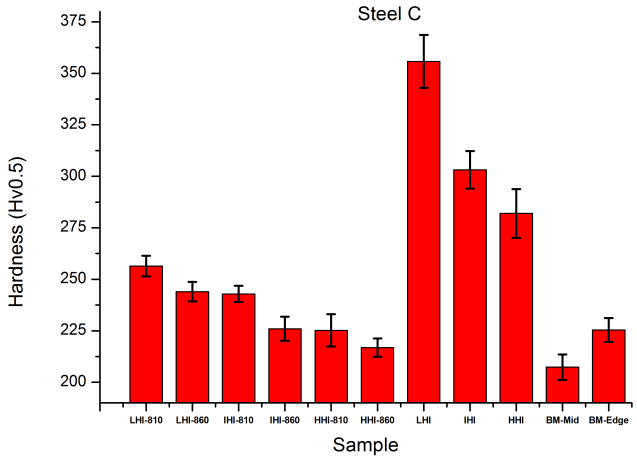

Figure 4.40: Hardness measured for all Gleeble samples and base metal of steel C, error bars are the standard deviation of the measurements.

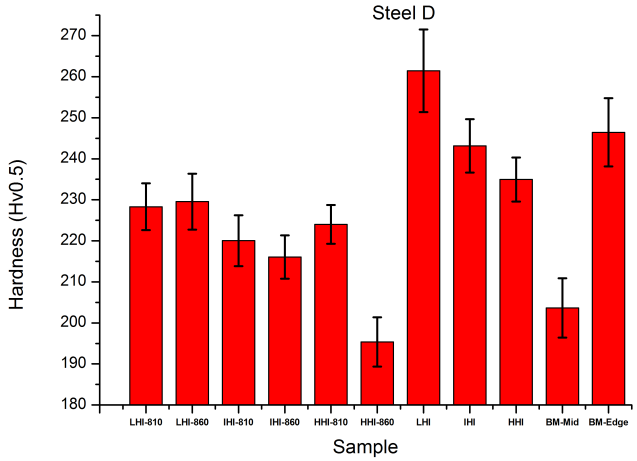

Figure 4.41: Hardness measured for all Gleeble samples and base metal of steel D, error bars are the standard deviation of the measurements.

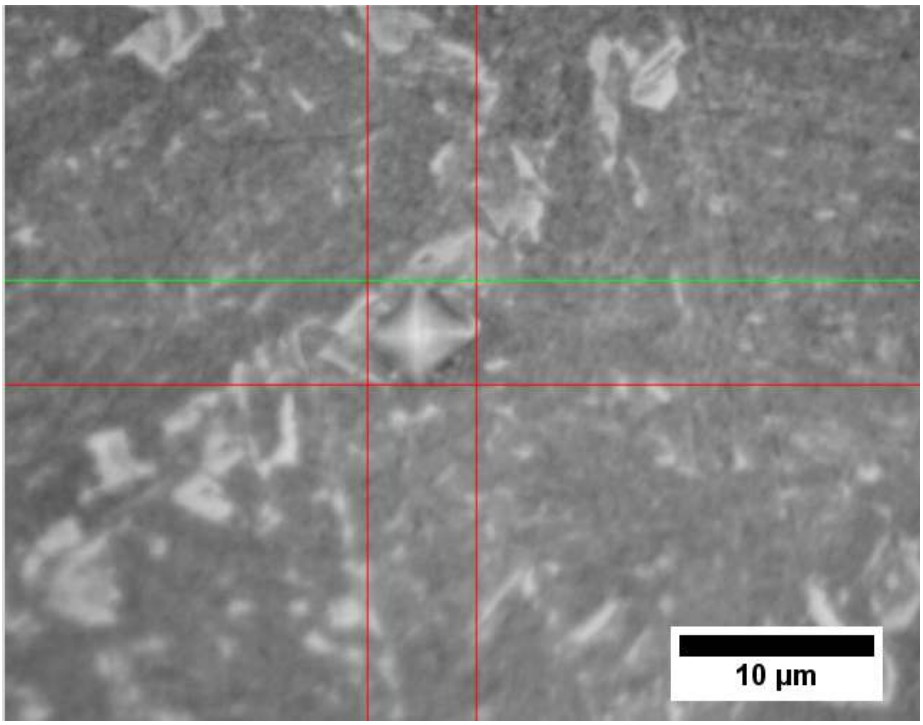

Figure 4.42: Indent in a M-A particle in D-LHI-810. The horizontal and vertical lines are the lines used for determining the diameters of the indent.

4.6.2 Micro hardness

The micro hardness was measured by a 10g load on both the M-A particles and matrix in the D-LHI-810 sample. This sample was chosen for the relatively large M-A constituents located at the prior austenite grain boundaries. A typical indent in a M-A particle is shown in figure 4.42. The average hardness found for the M-A particles was 289 HV0.01 with a standard deviation of 17 HV0.01 and a maximum of 310 HV0.01. The matrix hardness was measured as 226 HV0.01 with a standard deviation of 7 HV0.01 and a maximum of 234 HV0.01. The typical indent depth of these indents was around 1 µm.

Chapter 5

Discussion

5.1 General remarks

5.1.1 Dilatometer experiments

The goal of the dilatometer experiments was to determine Ac1 at higher heating rates than the ones which were calculated for an equilibrium situation. This knowledge is necessary in order to have the highest possible fraction of M-A constituents in the reheated CGHAZ simulations. The result from method IV is discarded because it did not yield a result for all steels. The results for method II and III were discarded because 840 and 820 °C were deemed too high when compared to results from earlier work[48;52]. In method V the first instant the derivative curve is bellow the minimum of the linear part is discarded as the peak after this part is due to the change in magnetic properties of the steel and no continued decrease in expansion coefficient is observed (see in figure 3.7). The results from method I and V are comparable, and using these, a reheat temperature of 810 °C was chosen for the CGHAZ simulations. In a real welding process, all peak temperatures between Ac1 and Ac3 will occur within the reheated CGHAZ. To study the peak temperatures which is possibly most detrimental to the toughness, the peak temperature which will result in the highest fraction of M-A was chosen, which according to Bonnevie et al.[57] should be in the window of Ac1 + 20-50 °C. The heating rate used for the dilatometer experiments is a factor 5 lower than the one eventually used for the simulations, but it was the highest heating rate possible for this sample geometry using this type of dilatometer. Some extra overheating an thus increase of Ac1 can take place, but the peak temperature of 810 °Cis still assumed to be within the windows to obtain the highest M-A fraction. Lepera etching did reveal a significant fraction of M-A constituent, confirming that an appropriate reheat temperature was chosen. The transformation temperatures found are comparable to the ones found by Yue et al.[85], whom observed 770 °C for Ac1 at a heating rate of 200 °Cs using a steel comparable in chemical composition to steel C in the current work. No relation between Ac1 and the

chemical composition is apparent as the transformation temperatures are within a reasonable range from each other (within 10 ˚C).

5.1.2 Gleeble experiments

The gleeble temperature profiles were chosen such that the resulting microstructure would fit the microstructure of the CGHAZ close to the weld pool. To this end, the first peak temperature was chosen as 1350 ˚C. This temperature was reached by using a heating rate of 250 ˚C/s which will in fact be higher in a real weld cycle (up to 1500 ˚C/s[86]). A higher heating rate of 500 ˚C/s was used at first but this heating rate caused the samples to locally melt and these samples were thus discarded. During the gleeble experiments, the temperature was controlled using a single thermocouple connected to the surface of the sample rods. The temperature within these rods however could not be measured, the cooling rate can thus be different, closer to the center of the sample. The peak temperatures are considered to be uniform in the radial direction of the samples, due to the heating by Joule heating. The peak temperatures however are not uniform in the length direction, therefore a region as small as possible around the thermocouple was taken from the sample rod in order to mitigate this effect. During microstructure observation, close attention was paid to the uniformity of the microstructure throughout the sample area.

5.1.3 Hardness measurements

The macro hardness measurements using a load of 500g are scalable upward to vickers hardness measurements with a higher load according to the ASTM standard[83] due to the diagonals of the indents being bigger than 25 µm in all cases. This scalability is however still dependent on grain size, if the size of the indent is in the order of the size of the grains, the hardness will be dependent on the microstructure, at the place the harness is measured. In this case the grain size was often visually sufficiently smaller than the minimum indent diagonal and the rest of local effects are averaged by performing at least 18 hardness measurements across the whole sample area. The micro hardness measurements on the M-A constituents were however less reliable, as the indent was often bigger than the size of the M-A particle and thus a lower value of the Vickers hardness was measured than the actual value. Due to the depth of the indent being around 1 µm which is smaller than the size of the biggest , this error is only present in the two visual dimensions.

5.1.4 Electron backscatter diffraction

The areas on which EBSD scans were performed are fairly small, but form optical microscopy results they are assumed to be sufficiently large to obtain a reasonable microstructural qualification. For the quantification of the microstructure points with a CI values lower than 0.05 were discarded, assuring that only points with a high probability of correct indexation were taken into

account. This procedure automatically discards the points allong the grain boundaries, which also have a low IQ value and these will no longer show up in the IQ distribution. The process as proposed by Wu et al.[81] to discard measurement points at grain boundaries is therefore no longer needed. This is illustrated by figure 5.1, where the gaussian term due to the grain boundaries also shown.

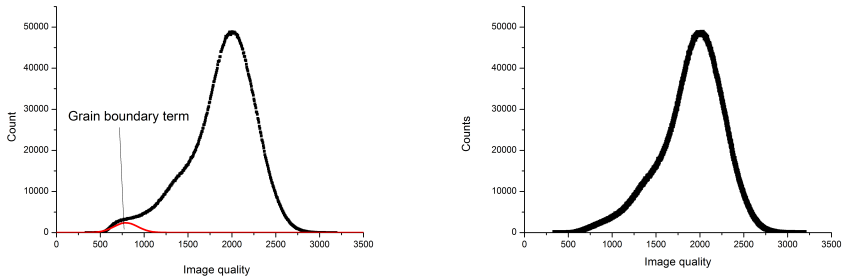

(a) (b)

Figure 5.1: Result on IQ distribution by discarding point with a CI lower than 0.05. (a) Shows the IQ with the low CI points and the gaussian curve for the grain boundaries is added (b) shows the IQ distribution with the low CI points discarded.

For the quantification of the scanned microstructures by the method of Wu et al.[81], it was assumed that three constituents were present. The IQ distributions of A-HHI and A-BM could however also be fitted to high accuracy by a sum of two Gaussian curves. In general, the distribution of the IQ could also be fitted using more than three Gaussian curves, this however yields constituents without physical meaning because these extra curves are small and were completely covered by curves from other constituents. An example of this is shown in figure 5.2. Automatic fitting by the curve fitting toolbox often gave unsatisfactory results and upper and lower bounds for the fitting parameter controlling the average of the Gaussian were chosen manually until the highest possible R^2 was achieved.

The other method used in this work is performed by fitting the IQ distribution with two Gaussian curves and assuming that the average of the Gaussian curve with the lowest IQ is the maximum grain average IQ of Martensite. The propose of this method is to have a reproducible way of choosing a IQ threshold for the creation of the maps such as figure 4.37. This method has no clear physical background but does yield good results, where the method of visually choosing a threshold is very dependent on the point in the scan which is chosen. The fraction of austenite found in all samples was lower than 0.1 %, thus the concentration of alloying elements was almost never high enough to halt the transformation from austenite to martensite.

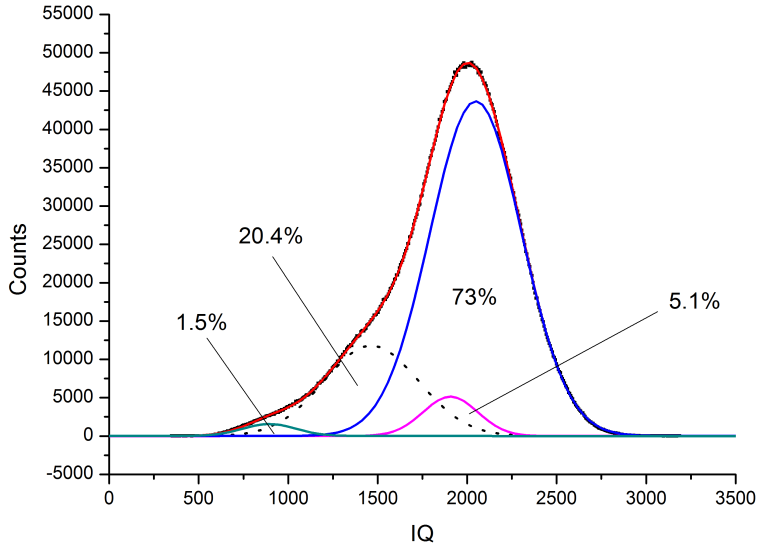

Figure 5.2: Example of the IQ distribution of A-LHI-810 fitted to 4 Gaussian curves.

5.1.5 Point count quantification

Quantification by a point count method of the microstructure in the coming sections was made difficult by the fact that, using only light microscopy, sometimes no easy distinction can be made between Martensite and Lower bainite or upper bainite and widmanstätten ferrite. The complexity of some microstructure makes accurate determination of its constituents impossible or useless by the fact of the uncertainty.

5.2 Base metal

The microstructures of the base metals A, B, C and D are visibly very different from each other. Also the microstructure from the edge of the pipe wall differs largely from the half thickness. This microstructure difference is reflected in the measured hardness difference between these two regions. During hot rolling in the manufacturing process, the deformation of the plate at the edge is bigger than at the center region (because of surface shear during rolling), causing a more clearly defined rolling texture at the edge of the pipe wall. Also, when cooled, the cooling rate at the edge of the pipe wall is higher, which causes a harder microstructure and smaller grains. The rolling morphology is not visible in the base metal of steel A and D, which in the case of steel A is due to the

rolling parameters. In the case of steel D this is due to the fact that the SMLS pipe manufacturing process does not include a conventional rolling process.

Etching of the base metals with Lepera's etchant did not show significant ammounts of M-A constituent, which was to be expected from the microstructure being mostly ferritic. The carbon has often segregated to pearlite regions, instead of martensitic regions. Furthermore, pipes are not quenched, causing martensite formation to be less likely.

The EBSD scan of the base metal shows the same acicular ferrite microstructure as found with optical microscopy. The EBSD scan also reveals some areas with a very low confidence index (smaller than 0.05) which will be the pearlite regions identified with optical microscopy. The reason for these small pearlite regions to have a low CI is due to the fact that cementite is not indexable by EBSD measurements which will deter the signal of the neighbouring ferrite.

Quantification of this microstructure shows that there are two constituents present, and a negligible third phase. These constituents differ in dislocation density but the nature of these constituents is not apparent from optical microscopy. Using Lepera's etchant almost no M-A could be found, which is confirmed by the quantification.

5.3 Coarse-grained heat-affected zone

Before discussing the simulated microstructures further, it should be noted that the thermal gradient in the CGHAZ zone can be very high and the microstructure which were produced are only a very small part of the CGHAZ. This is especially the case when part of this CGHAZ is reheated, causing large gradients in microstructure constituents. This is illustrated by figure 4.26, which shows that the CGHAZ only consits of 2 or 3 prior austenite grains in the width direction.

For the simulation of the coarse grained heat affected zones samples were machined out the of the pipe wall. To this purpose, the edge region (the smaller grained region) was found too small for the Gleeble experiments. The assumption is therefore made that the base metal microstructure has no significant influence on the experiment as the austenite grains growth rate is very high at these elevated temperatures, especially shortly after the onset of transformation (seeequation (2.3)). The difference in microstructure was not mentioned in previous work and only the effect of the chemical composition was considered.

5.3.1 Microstructure

At the lowest heat input the microstructure of the CGHAZ the main microstructure constituent is either bainite or martensite with, in the case of steel A,B and D, a small amount of acicular ferrite. In order to confirm these observations done by optical microscopy, the hardness and transformation temperature will be investigated and compared to theoretical values (sections 2.4.3 and 2.6).

An indication of the transformation temperature can be obtained from the measured temperature during the Gleeble experiments. When the steel transforms from austenite during cooling, heat is released, which causes the cooling rate to decrease. During the LHI experments, the cooling capacity of the Gleeble was insufficient to negate this released energy, which is clearly visible in figure 4.2. After this transformation the cooling rate is again as prescribed. The heat of transformation is not released at once and the cooling capacity can still be sufficient at the start of the transformation, therefore this gives only an indication. Note that martensite grains (plates) grow at a speed of 800-1100 m/s which gives very little time for heat build up[12]. Furthermore, the temperature found gives, at most, a lower value of the transformation temperature. The transformation temperatures found using this method are shown in table 5.1, as well as the bainite start temperature and the martensite start temperature according to equations (2.4) and (2.6).

Table 5.1: Cooling transformation start temperatures of the LHI temperature cycles measured from the Gleeble experiments and compared to theoretical values.

Steel	Tranformation start temperature (°C)	B_s	M_s
A	539 ± 10	625	483
B	590 ± 5	640	488
C	473 ± 7	636	439
D	529 ± 15	619	464

In table 5.2 the measured hardness is compared to theorerical hardness values given by equations (2.8a), (2.8b) and (2.9). These equations give a hardness for a fully martensitic or bainitic microstructure.

Table 5.2: Measured hardness for the LHI samples compared to theoretical hardness values. Hardness values are given in Vickers hardness.

Steel	Hardness	H_m(eq. 2.8a)	H_m(eq.2.9)	H_b (eq. 2.8b)
A	232	233	330	145
B	211	223	324	103
C	356	255	354	118
D	261	244	340	152

From the transformation temperatures found using the results from the gleeble experiments, it is likely that A,B and D are a bainitic microstructure, as they were also identified from optical microscopy. The transformation temperature is too high for the microstructures to be martensite, and the microstructure will therefore consist of uppper, lower or granular bainite. The transformation temperatures found for steel A and D match the transformation temperature for upper bainite and for steel C that for lower bainite as reported by Reichert et al.[87]. The hardness of a bainitic microstructure predicted by equation (2.8b) shown in table 5.2 is however significantly lower than any hardness measured on the steel considered. Therefore, the formulas for hardness calculation as proposed by Blondeau et al.[40] are considered as not applicable for the steels discussed in this work. The hardness of steel C is spot compared to the martensite hardness as predicted by equation (2.9). A similar approach is not possible for the rest of the samples, as the transformation is no longer visible in the measured gleeble temperature profile and the microstructures have visually changed and do no longer mainly consist of a single constituent. In all CGHAZ samples, except for B-HHI, prior austenite grain boundaries are still visible which indicates that the transformation from austenite was displacive and nucleated on the prior austenite grain boundaries.

When the microstructures found are compared to the microstructures expected from the CCT diagrams in section 2.8.1, a number of conclusions can be drawn.

When the microstructures of steel A are compared to the ones found by Zhao et al.[32] and Zhang et al.[62] which have similar carbon content, the microstructures found by Zhao et al.[32] are similar to the ones found in current work, even tough the nomenclature used is different. The acicular ferrite found by Zhao et al.[32] is interpreted as upper bainite for steel A. When compared to experiments by Zhang et al.[62], it is concluded that the addition of chromium (2 wt%in this case) causes martensite to form more readily at higher cooling rates.

Steel B is similar in carbon content to steel C discussed by Zhao et al.[32] and indeed shows similar microstructures to the ones found by experiments performed in for this work. The spherical cementite particles found for the high heat input cycle, were however not found or identified by Zhao et al.[32].

Steel C is comparable in carbon content to the steel discussed by Zhang et al.[63] and steel B as discussed by Zhao et al.[32]. Zhang et al.[63] concluded that the addition of Nb causes martensite to form at high cooling rates, which is the case for for steel C in current work. Zhao et al.[32] however did not find this to be the case. There is no apparent reason for this difference.

Steel D, when compared to the work by Kong and Qiu[64] shows that the addition of a small ammount of Ni, Mo, and Cr (0.85 wt%) can cause martensite to form at high cooling rates in steels of a similar carbon content. Jun et al.[66] however found martensite without the addition of the alloying elements. The

regions of martensite found by Jun et al.[66] were however fairly small and might not be distinguishable by light microscopy.

One mentionable microstructure found is the one for B-HHI which shows spherical carbides throughout the microstructure (figure 4.10b). This is the only sample which shows these spherical cementite particles, suggesting the formation is dependent on the chemical composition of the steel. No cause for this microstructure occurrence can however be found in previous works.

Lepera etching was also performed on the CGHAZ samples. The etching, which was performed more than 5 times on each sample, did not yield consistent results. In literature it is often noted that the M-A constituent is mostly revealed at the bainite lath boundaries, which is also where the cementite within upper bainite is located. In current work, Lepera etching did indeed reveal a constituent at the bainite lath boundaries (a parallel elongated constituent shown in figure 4.7a), especially for the LHI and IHI samples. Lepera[60] noted that the etchant also tends to etch large carbides and it can thus not be concluded that these elongated constituents are either M-A constituents or carbides located at the lath boundaries of the upper bainite.

The quantification of the EBSD scan of A-HHI shows that the microstructure consists out of 2 constituents. The highest fraction is the ferritic constituent with the higher IQ. This ferritic constituent is the granular bainite which was identified by optical microscopy making the other constituent, upper bainite which is concluded due the difference in dislocation density between the two microstructures[23]. The fraction of martensite found is negligable and the distribution could just as well be fitted by a sum of two Gaussian curves.

When comparing the CGHAZ samples to the actual weld microstructure shown in figure 4.26 the microstructure marked by the yellow circle shows similarities to the A-HHI samples, which suggest slow cooling. The lack of the bainitic structures which were found in A-HHI in the real weld CGHAZ also suggest a low cooling rate in the real weld. Some pearlitic regions also were found in the real weld, which were not present in any of the simulated samples, which once more suggest a lower cooling rate than discussed in this work.

5.3.2 Hardness

The hardness of all the CGHAZ simulated samples was parametrised for chemical composition and cooling rate. The result is shown in equations (5.1) and (5.2). This parametrization gives the highest hardness which is to be expected in the CGHAZ.

$$\mathrm{Hv} = (11,5\mathrm{Pcm}^* - 1,57)\mathrm{CR} + 289\mathrm{Pcm}^* + 170 \tag{5.1}$$

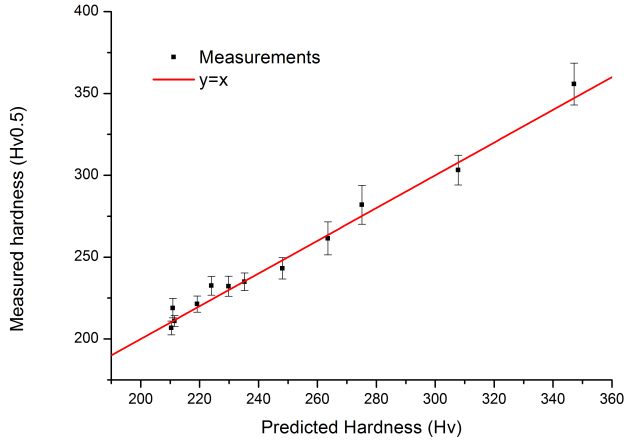

Figure 5.3: The hardness of the CGHAZ as predicted by equation (5.1) compared to the measured hardness.

Where CR is the cooling rate from 800 to 500 °Cand Pcm* is given by the adjusted Pcm formula:

$$\text{Pcm*} = \text{Pcm} + \frac{11Ni}{60} + \frac{Nb}{5} \tag{5.2}$$

Where Pcm is defined as equation (2.11a). In this formula, the contribution of Ni has been increased and a contribution by Nb has been added. Ni was added due to the extra hardening in steel C, which has only added Ni content when compared to the other steels. This can be justified by the fact that Yoshinori and Kiyoshi[88] did not take into account a similar Ni content and no Niobium containing steel when defining Pcm. Furthermore, as can be seen in table 2.4 and figure 2.2 Ni and Nb both increase the hardenability. Nb by forming highly stable carbides in the austenite phase which impinge austenite grain growth, creating smaller ferrite grains at cooling which causes a greater hardness. The same factor for Nb was also used by Lazor and Graville[89] for the representation of the hardenability in HSLA steels. Even tough Ni does not form carbides it does form stable intermetallic precipitates with Mo and it retards pearlite formation, which increases the possibility for bainite or martensite formation. Pcm was used as a parameter for the hardenability in this case, because pipe manufacturers tend to cite the Pcm value in the specification sheet for linepipe steels and the maximum hardness can thus be easily calculated. Pcm is a empirical hardenability number used for representing the susceptibility of a weld to cold cracking. The results of this parametrization is shown in figure 5.3. The result is compared to the formulas by Kasuya et al.[41](equation (2.10))and Nolan et al.[42](equation (2.11)) in figure 5.5.

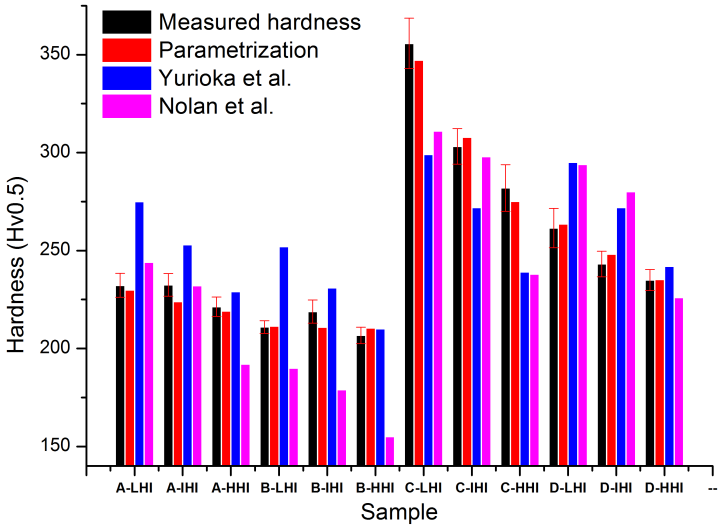

Figure 5.4

Figure 5.5: The hardness of the CGHAZ as predicted by equation (5.1) compared to the measured hardness and predicted hardness by Kasuya et al.[41] and Nolan et al.[42].

As can be seen in figure 5.3 the parametrisation given in this section gives a fairly accurate prediction (but not always conservative) of the hardness in the CGHAZ, with an R^2 value of 0.98. The formulas taken from literature however do not agree with the measured hardness for most measurements as can be seen in figure 5.5, which have negative R^2 values. This can be attributed to the difference in chemical composition between the steels in current work and the steels used for deriving equations (2.10) and (2.11). Using the steel used for this thesis, the range of alloying elements are shown in table 5.3. If the peak temperaterature of the first cycle is lower than 1350 °C, but still within the CGHAZ region, less austenite grain growth will occur and the resulting bainitic or martensitic microstructure will contain smaller grains resulting in a slightly higher hardness. In practice, this causes the hardness in the CGHAZ of a real weld to be higher than the one given by this parametrization if one would measure the hardness further away from the weld pool, where the achieved peak temperature was lower than 1350 °C.

Note that the LHI and IHI temperature cycles for steel C result in a hardness which exceeds the maximum allowed hardness by[5] which is 300 Hv.

Table 5.3: Range of elements for which the parametrization of equations (5.1) and (5.2) is applicable.

Element	range (wt%)
C	0.034 - 0.068
Mn	1.27 - 1.51
Cr	0.02 - 0.26
Si	0.20 - 0.31
Mo	0.01 - 0.22
Nb	0.002 - 0.041
Al	0.022 - 0.033
Ti	0.011 - 0.015
Cu	0.01 - 0.20
Ni	0.01 - 0.37
V	0.0046 - 0.0487
B	0.0002
Pcm	0.126 - 0.174

5.4 Reheated coarse-grained heat-affected zone

5.4.1 Hardness

When the hardness of the CGHAZ samples is compared to the hardness of the reheated CGHAZ for the same heat input, the hardness of the CGHAZ is highest for all steels. As problems will probably occur at high hardness values and the applicable standard sets upper bounds to the hardness, the macro hardness of the reheated CGHAZ is of less importance. This softening effect due to reheat is different from results found by some authors whom observed hardening, for example Zhu et al.[67](figure 2.26). A reason for this difference with literature might be due to the fact that often, the cooling rate in the second cycles is taken to be the same as in the first cycle, whereas this cooling rate is found to be significantly lower in the second cycle in present work. The higher cooling rate can result in a harder and/or larger fraction of M-A constituents, which causes the overall hardness to be higher. Due to the second cycle being inside the intercritical region, the ferrite which does not transform will lose its carbon to the newly formed austenite (which will later (partly) transform to M-A constituents). Due to this effect, the bainitic microstructure changes into a ferrite microstructure (acicular or polygonal), without carbides. The formation of M-A constituents does not completely rectify this effect.

The hardness in the reheated CGHAZ was lower for the reheat temperature of 860 °C than for the reheat temperature of 810 °C, which can be directly related to the fraction of M-A constituents which is lower for the higher reheat temperature. Another reason for this softening is due to the fact that a higher fraction of the steel has transformed to austenite, which will transform to softer

microstructure than the one after one cycle, due to the lower cooling rate in the second cycle.

Overall the hardness is lowered at higher heat inputs, except for the D-HHI-810 samples, which is not easily explained by microstructural features.

5.4.2 Microstructure

The main microstructure of the CGHAZ samples is mostly lost during the second temperature cycle. The LHI and HHI samples which were reheated to 860 ˚Cshow small ferrite grains, and no prior austenite grain boundaries phase nor traces of the microstructure after one cycle. This shows that these samples have for the most part been transformed to austenite but no austenite grain growth was allowed to take place, creating small ferrite grains when cooled. In the case of the LHI-860 cycles, one might expect these small austenite grains transform to a similar microstructure as the IHI cycles, which is not observed using optical microscopy and is probably due to the small austenite grain size. The HHI-860 temperature cycle does allow for austenite grain growth in steel A, B and D and the grains are visually bigger than for the other two cycles. Steel C still shows fairly small grains due to the higher carbon content which can form grain refining carbides with the other alloying elements. The same microstructure as observed for A-HHI-810 and A-HHI-860 was found by Li et al.[48] whom investigated steel of a similar chemical composition and a similar temperature cycle.

The LHI-810 and IHI-810 samples have a complex microstructure in which traces of the microstructure after one thermal cycle can be found. Steel A, B and D show remnants of the former bainitic structure but some areas have transformed to ferrite with no substructure or carbides. These ferrite grains are of a very jagged shape and the outer boundaries can be assumed to outline the former bainite blocks. If the carbides are removed from the bainite lath boundaries, only the outer boundaries of the blocks remain. These ferrite grains with jagged edges, as well as the bainite and M-A constituents, are marked in figure 4.11a. Steel C does not show these particular microstructural constituents and has a complex microstructure which cannot be qualified using optical microscopy only. The microstructure of steel D contains less of the ferrite phase than steel A and retains a larger bainite fraction from the first pass. The observed microstructure for A-LHI-810 and D-LHI-810 resemble the microstructure found by Li et al.[48], whom described is as having an irregular arrangement. The microstructure of A-LHI-810, A-LHI-860 and D-LHI-810 were also investigated using EBSD scans. The IQ maps of the A-LHI-810 and D-LHI-810 show the bainite laths also found using optical microscopy, surrounded by a proir austenite grain boundarie constituent with a lower image quality, indicating M-A constituents. The bainite laths identified in IQ maps have similar orientations or small angle grain boundaries between them, which confirms the identification of bainite laths by optical microscopy. The microstructure quantification for A-LHI-810 does however not show the bainitic phase as the constituent with

the highest fraction but rather a constituent with a lower dislocation density. This indicates that the second heating cycle causes tempering within the upper bainite giving a lower dislocation density both during heating and cooling. This effect is also noted when looking at the increased fraction of ferrite (from 0.77 to 0.88) when the LHI sample is reheated to 810 °C. Due to the higher hardenability (reflected by the Pcm* values) of steel D, this tempering effect is less pronounced and the fraction of bainite is higher than the fraction of ferrite.

A difference between steel A and steel D is that the fraction of ferrite decreases from 0.85 to 0.76 with increased reheat temperature in the case of steel A but increases from 0.398 to 0.697 in the case of steel D. The eventual fractions are however very similar. In the case of steel A this can be explained by the fact that a big fraction of the sample transforms to austenite when reheated to 860 °Cwhich transforms to bainite upon cooling, which is concluded from the optical microscopy results of sample A-IHI because of it having the same cooling rate as the second cycle in the LHI-860 temperature profile. As fractions of bainite in both steel A and B are similar after the LHI-860 temperature cycle, this is very likely to have occurred.

The microstructures of the HHI-810 samples of steels A, B and D do contain the bainite fraction which is retained from the single cycle sample. The prior austenite grain boundaries are no longer visible. Steel A has a complex microstructure with grain boundaries which appear like a double line, indicating grain boundary carbides (cementite).

5.4.3 Martensitic austenitic constituents

Lepera's etchant

Using Lepera's etchant, M-A constituents were revealed in all reheated samples. When quantifying this revealed M-A constituents there is however a significant error due to the fact that a contrast threshold value has to be chosen manually, changing the result significantly. By choosing a threshold visually for every analysed photo, and not a fixed value, this error is mostly incorporated in the standard deviation. Another noticed effect when using this etchant is that for high fraction of M-A constituents the etchant does not tend to reveal the M-A constituents uniformly, some particles might be brighter than others or even a brightness gradient within a particle. The fractions given are, due to observed inconsistency in etching effect and the error due to the threshold, not accurate but will give an estimation of the fraction of M-A constituents. Due to 3D isotropy, the area fraction measured can be assumed to be the same as the volume fraction of M-A constituents.

Overall the fraction of M-A constituents decreased with increased reheat temperature, which was also observed in previous works[67]. The fractions found for steel A-HHI-810 and A-HHI-860 are similar to the fractions found by Zhu

et al.[67] on steel of a similar composition and similar temperature cycles. The fraction is also found to decrease with increasing heat input, which is due to the lower cooling rate which will cause less austenite to transform to martensite. The fraction of M-A constituents in steel B is nearly constant for all samples, which shows that the welding process and the location in the reheated CGHAZ has no influence on the fraction of M-A constituents for steels of this composition.

For all samples reheated to 810 °C, except for sample B-HHI-810, the M-A constituent was found to be located at the prior austenite grain boundaries. The average size of these M-A constituents is often larger than the the ones found for a reheat temperature of 860 °C. This is due to the fact that only a small part transforming to austenite in the samples reheated to 810 °C, which causes this reverted austenite to (almost) completely transform to M-A, which are relatively big. This is different from what was observed by Davis and King[22] whom found no necklacing M-A constituents at the prior austenite grain boundaries for this reheat temperature, but rather M-A constituents homogenously distributed trough the microstructure. When the steel is reheated to 860 °Ca much larger fraction has transformed to austenite, causing only regions which locally contain a higher carbon content to transform to M-A constituents. In figure 4.18 it should be noted that the prior austenite grain size for steel D is somewhat bigger than for steel A and C, which is explained by a problem during the gleeble heat treatment, causing the the steel to stay a second longer in the austenite phase when compared to the other samples (the prescribed cooling rate from 1350 °C to 800 °C was not achieved).

Electron microscopy

Electron microscopy also shows the M-A constituent located at the prior austenite grain boundaries for D-LHI-810. When these particles are observed at a higher magnification, they contain a clear internal structure, which is different from the edges (figure 4.28). This suggests that the M-A constituents as identified by electron microscope, might consist of other microstructure constituents than martensite and austenite. The inhomogeneity of the M-A constituents is due to the limited time between Ac1 and Ac3, giving little time for the carbon to diffuse to the center of the just formed austenite, the same was noted for higher grade linepipe steel by Zajac et al.[90]. In general the bigger particles have an internal structure which is not martensite, which can also be seen in figure 4.27. The Backscatter electron imaging does show an increased carbon content in these regions indicating a higher fraction of alloying elements as the surrounding ferrite. The difference between the border and the internal parts of the M-A constituents are also seen in the backscatter imaging figures, confirming the inhomogeneity of the alloying elements.

Electron backscatter diffraction

The methods described to identify M-A constituents are based on the martensite having a higher dislocation density than other constituents. The areas in which martensite is able to form due to higher carbon content can however also transform to other microstructure constituents which are less hard than martensite, which is also confirmed by the observed inhomogeneity in the M-A constituents using secondary electron imaging (figure 4.28). These microstructure constituents, for instance upper bainite, can have a dislocation density close to that of martensite. The fact that a relatively large change in identified fraction of martensite occurs with a slight change in IQ threshold suggests that not only M-A constituents are present but also constituents with a dislocation density close to that of M-A constituents. This makes it hard to choose a threshold value for the IQ for which it is certain that martensite is identified. The microstructural quantification as by analyzing the IQ distribution using a sum of three Gaussian curves, does not yield a threshold value and can thus not be used to this extent.

The values found for the M-A constituent fraction for samples A-LHI-810 and D-LHI-810 using the method with gaussian curves to find a threshold value, are comparable to the ones found using Lepera's etchant. The necklacing structure found using Lepera's etchant for A-LHI-810 and D-LHI-810 is however not as apparent in the EBSD results. Applying the appropriate orientation relationships from table 2.6 does show that most areas identified as M-A constituents using EBSD have indeed transformed form a single austenite grain and are thus a likely candidate to be M-A constituents. The result of the application of these orientation relations is somewhat obscured due to the fact that prior austenite grain boundaries from the first cycle and grains that have transformed trough a non-displacive mechanism, are also highlighted. It can also be seen in figure 4.33 that the grains identified as martensite have transformed through a displacive mechanism satisfying the N-W or K-S orientation relations.

For the A-HHI-810 and A-HHI sample, no appropriate IQ threshold could be found using the visual method for identifying M-A constituents and the method using Gaussian fits for identifying an appropriate threshold yielded very low fractions of M-A constituents. This suggests that no M-A constituents are present within the microstructure. For D-LHI-860 no M-A constituents could be visually identified in the IQ map.

The prepared sample of A-LHI-860 contained too many scratches on the surface which caused the IQ of some grains to be lowered despite the actual microstructure and therefore the identified fraction found by the threshold method is incorrect.

The quantitative analysis of the IQ distributions also yields a fraction of M-A constituents which is, from all the methods employed for the EBSD scans,

Table 5.4: Comparrison between different methods for evaluating the fraction of M-A constituents, values are given in vol.%.

	A-BM	A-LHI-810	A-LHI-860	A-HHI
Lepera etching	0	5.5	3.4	-
Quantitative IQ analysis	0	4.0	1.8	0.3
Visual threshold	0	3.2	-	-
Gaussian threshold	0	5.1	10.2	0.6
	A-HHI-810	D-LHI-810	D-LHI-860	
Lepera etching	4.6	7.4	2.5	
Quantitative IQ analysis	3.8	5.4	2.6	
Visual threshold	-	5.5	4.2	
Gaussian threshold	0.5	7.9	3	

the most tested and reliable as it is not dependent on local microstructure in that the inhomogeneity found in the secondary electron images are taken into account. The result from Lepera etching, the two thresholding methods and the quantatative IQ analysis are compared in table 5.4. In general the fraction of M-A constituents found with Lepera etching is higher than the fraction of martensite identified with quantitative IQ analysis, which is due to the fact that the M-A constituent is not homogeneous, as revealed by the Lepera's etchant.

Microhardness

The microhardness found for the M-A consituents was much lower that that found in previous works, a maximum of 310 Hv versus an average of 600-1000 Hv. Due to the error discussed at the beginning of the chapter, the value of 310 Hv can in reality be higher but not twice as high. In order for the hardness to be twice as high as the measured value, only half of the M-A particle had to have been measured. This is not the case when inspecting the location of the indent. The hardness of the M-A constituents is however still higher than that of the matrix, 226 Hv versus 310 Hv which does show that it is a microstructural constituent than the matrix. The fact that the hardness is lower than expected, again shows that the M-A constituents as revealed by Lepera's etchant are not fully martensitic.

5.5 Fracture toughness

5.5.1 Relation to previous work

This section will relate the observed microstructures to the expected toughness properties of the CGHAZ and the reheated CGHAZ. The second and third mechanisms described by Davis and King[46] (section 2.8.3) are dependent on

the morphology of the M-A constituent, which is the (near) connected M-A phase along the prior austenite grain boundaries which were present for all CG-HAZ samples reheated to 810 °C. This in combination with the independence of the fraction of M-A constituents predicts that the toughness will not depend on the chemical composition or the heat input of the welding process (at least for the ones considered in this work). The third mechanism will however be more pronounced for high heat inputs, as the strength mismatch is bigger between the M-A constituents and the matrix (which is concluded from the hardness), causing higher stress concentrations and eventually easier debonding. Even tough the fourth mechanism proposed by Davis and King[46] has not been confirmed experimentally, this mechanism will also be more pronounced in a softer matrix.

The average size of the M-A constituents decreases for a higher reheat temperature for the LHI and HHI temperature cycles. For the HHI temperature cycle this is however not the case, here the average size increases with the increased reheat temperature. The spread in size of the M-A constituents can be anywhere from 0.1 μm^2 to 60 μm^2 The average size does not give a prediction for the toughness behaviour as there seems to be no trend.

The mechanism by Ohya et al.[75] and Yokoyama and Nagumo[73] states that the crack initiation will take place at boundaries between bainitic structures and (quasi-)polygonal ferrite. These boundaries are mostly present in the LHI-810 and IHI-810 temperature cycles where part of the upper bainite from the single heating cycle has transformed to quasi-polygonal ferrite. Quantitative IQ analysis shows that D-LHI-810 has the bainite to ferrite ratio closest to 1 of all the scan performed, making it the best candidate for this mechanism to occur.

HAGB's tend to retard crack propagation and thus a higher fraction of HAGB's tend to increase the fracture toughness. The fraction of HAGB's only increased in the CGHAZ and the reheated CGHAZ and thus this not be an explanation for toughness deterioration.

5.5.2 Conclusion

Electron microscopy showed that constituents revealed as M-A by etching are not homogeneous in microstructure and are not fully consisting of martensite and austenite, which is suspected to be due to inhomogeneous distribution of carbon. Furthermore, microhardness of M-A shows a lower hardness than was to be expected from previous work, and IQ analysis of the microstructures yielded a lower fraction of M-A constituents than revealed by Lepera's etchant. These results show that the M-A constituents might not be as detrimental to the fracture toughness as suspected in previous work, at least in the steels and thermal cycles discussed in this thesis. The theories for the toughness degradation are all based on the assumption that M-A constituents as revealed by Lepera's etchant are fully martensitic austenitic. It must be mentioned that it was never fully proven that M-A constituents are responsible for decreased

fracture toughness. As electron microscopy and microhardness measurements were only performed on one samples, this conclusion might not hold in all cases.

Chapter 6

Conclusions

In this thesis the effect of single pass welding and multipass welding on the microstructure and hardness has been investigated for X65 linepipe steel of four different chemical compositions, three heat inputs and two reheating temperatures. The thermal simulation has been achieved by simulating the CGHAZ with a Gleeble® thermal-mechanical simulator and the reheat peak temperatures used for this simulation were derived from dilatometer experiments. The resulting microstructures were thereafter examined by optical and scanning electron microscopy as well as EBSD. The overall hardness of the samples was measured as well as the micro hardness of M-A constituents. The hardness of the single pass CGHAZ was parametrized for the cooling rate and the chemical composition. A number of samples were quantitatively described by use of the IQ distribution from EBSD measurement and the M-A constituents were quantified by Lepera's etchant for all multipass welded samples. Finally the fractions and morphology of M-A and the surrounding matrix microstructure was related to fracture toughness measurements from previous research. The following general conclusions can be drawn:

- Overheating of the ferrite phase by more than 50 °C occurs at high heating rates which causes austenite to form at higher temperatures than assumed in some of the previous work.
- The assumption in most previous research that the second heating cycle for multipass welding causes the same cooling rate in the CGHAZ as the first cycle, was found to be wrong. The cooling rate in the second cycle was found to be nearly half that of the first. Due to this, the hardness in the reheated CGHAZ was found to be lower than that in the single pass CGHAZ, which is different from what was observed in some of the previous research.
- The hardness of the CGHAZ was successfully parametrized for the cooling rate and chemical compositions. This parametrization can predict whether the hardness becomes too high or low for the wanted application. It was

found that the alloying with a small fraction of Ni (0.3 wt %) causes additional hardening in the CGHAZ.

- Using Lepera's etchant, M-A phase was revealed in all reheated samples with a minumum fraction of 1.6 %. The fraction was found to be highest for steel with high hardenability and the temperature cycle for low heat input welding (up to 9.7 %). The fraction was found to be independent of heat input or reheat temperature for steel with a low hardenability (Pcm of 0.126).In the CGHAZ reheated to 810°C, M-A was found at the prior austenite grain boundaries in a necklacing structure as well as elongated particles within the prior austenite grains.This morphology is independent of heat input.

- Lepera's etchant, generally used in previous work for quantifying the M-A fraction, was found to be unreliable for revealing M-A in single pass CGHAZ, for steels of the chemical compositions and weld heat inputs discussed in this work. EBSD measurements revealed no significant amount of martensite in a steel subjected to a single pass temperature cycle of a high heat input weld process.

- When quantifying the simulated microstructures by EBSD IQ quantification it is found that use of only optical microscopy might yield a wrong impression of the characteristics of the microstructure. Observed bainitic microstructures by optical microscopy were found to be lower in dislocation density than expected and the fraction of martensite was found to be lower than what was observed from etching with Lepera's etchant. The second weld pass was found to have a tempering effect on the microstructure of the first pass.

- Observed fractions of retained austenite by EBSD on two steel compositions and two weld heat inputs were found to be nearly zero.

- The fracture toughness is independent of heat input when only the morphology of M-A constituents is concerned. The combination of a soft microstructure matrix and the distribution of M-A for a high heat input weld processes might be detrimental for the toughness.

- M-A constituents, as revealed by Lepera's etchant, were not found to be fully martensitic-austenitic in the steels considered and are thus of less importance for the fracture toughness than reported by previous research.

Chapter 7

Recommendations

- To give a better prediction of the hardness in the CGHAZ, more cooling rates and chemical compositions need to be investigated. The exact reason why Ni gives increased hardenability must also be explained, by varying other alloying elements.
- Transmission electron microscopy is needed to give insight in the exact microstructure of the M-A constituents.
- Electron microscopy has to be performed on more samples to confirm the inhomogeneity of large M-A constituents.
- Complete austenite grain reconstruction using the obtained EBSD scans can give insight in the exact transformation mechanisms during multipass welding.
- Fracture toughness measurements should be performed on the CGHAZ simulated samples to examine the influence of the microstructures investigated.
- Nanohardness measurements should be performed on various locations within M-A constituents to examine the exact hardness of these particles.
- The influence on toughness of the cementite particles found at high heat input weld cycles should be investigated.
- Insight in the chemistry of Lepera etching should be obtained to find what constituents are revealed by the etchant.

Chapter 8

Bibliography

[1] *API 5L: Specification for Line Pipe*. American Petroleum Institute, 43th edition, October 2004.

[2] Wengui Zhao, Wei Wang, Shaohui Chen, and Jinbo Qu. Effect of simulated welding thermal cycle on microstructure and mechanical properties of x90 pipeline steel. *Materials Science and Engineering: A*, 528(24):7417–7422, 2011.

[3] MD Herynk, S Kyriakides, A Onoufriou, and HD Yun. Effects of the uoe/uoc pipe manufacturing processes on pipe collapse pressure. *International Journal of Mechanical Sciences*, 49(5):533–553, 2007.

[4] AM Sage. Physical metallurgy of high-strength, low-alloy line-pipe and pipe-fitting steels. *Metals Technology*, 10(1):224–233, 1983.

[5] Offshore Standard. Submarine pipeline systems, 2007.

[6] Madeleine Durand-Charre. *Microstructure of steels and cast irons*. Springer, 2004.

[7] Bruce L Bramfitt. *Metallographer's guide: practice and procedures for irons and steels*. ASM International, 2001.

[8] C-M Raihle and Hasse Fredriksson. On the formation of pipes and centerline segregates in continuously cast billets. *Metallurgical and Materials Transactions B*, 25(1):123–133, 1994.

[9] KW Andrews. Empirical formulae for the calculation of some transformation temperatures. *J. Iron Steel Inst*, 203(7):721–727, 1965.

[10] Herman W Pollack. Materials science and metallurgy. 1988.

[11] Edgar C Bain and NY Dunkirk. The nature of martensite. *trans. AIME*, 70(1):25–47, 1924.

[12] David A Porter, Kenneth E Easterling, and Mohamed Sherif. *Phase Transformations in Metals and Alloys, (Revised Reprint)*. CRC press, 2009.

[13] Hiske Landheer. *Nucleation of ferrite in austenite: the role of crystallography*. TU Delft, Delft University of Technology, 2010.

[14] Harry Bhadeshia and Robert Honeycombe. *Steels: microstructure and properties: microstructure and properties*. Butterworth-Heinemann, 2011.

[15] Astrid Lambert-Perlade, Anne-Françoise Gourgues, and André Pineau. Austenite to bainite phase transformation in the heat-affected zone of a high strength low alloy steel. *Acta Materialia*, 52(8):2337–2348, 2004.

[16] Xueda Li, Yuran Fan, Xiaoping Ma, SV Subramanian, and Chengjia Shang. Influence of martensite-austenite constituents formed at different intercritical temperatures on toughness. *Materials & Design*, 2014.

[17] E Nes, N Ryum, and O Hunderi. On the zener drag. *Acta Metallurgica*, 33 (1):11–22, 1985.

[18] Seok-Jae Lee and Young-Kook Lee. Prediction of austenite grain growth during austenitization of low alloy steels. *Materials & Design*, 29(9):1840 – 1844, 2008.

[19] KW Andrews. Empirical formulae for the calculation of some transformation temperatures. *J. Iron Steel Inst*, 203(7):721–727, 1965.

[20] Hong-Seok Yang and HKDH Bhadeshia. Austenite grain size and the martensite-start temperature. *Scripta materialia*, 60(7):493–495, 2009.

[21] Y-K Lee. Empirical formula of isothermal bainite start temperature of steels. *Journal of materials science letters*, 21(16):1253–1255, 2002.

[22] CL Davis and JE King. Effect of cooling rate on intercritically reheated microstructure and toughness in high strength low alloy steel. *Materials Science and technology*, 9(1):8–15, 1993.

[23] G Thewlis. Classification and quantification of microstructures in steels. *Materials Science and technology*, 20(2):143–160, 2004.

[24] George Krauss and Steven W Thompson. Ferritic microstructures in continuously cooled low-and ultralow-carbon steels. *ISIJ international*, 35(8): 937–945, 1995.

[25] M Yu Matrosov, IV Lyasotskii, AA Kichkina, DL Dyakonov, and AA Efimov. Microstructure in low-carbon low-alloy high-strength pipe steel. *Steel in Translation*, 42(1):84–93, 2012.

[26] Chao Sun, Shanwu Yang, and Guoliang Liu. Evolution of microstructures of a low carbon bainitic steel held at high service temperature. *Acta Metallurgica Sinica (English Letters)*, 27(3):436–443, 2014.

[27] A Jacot, M Rappaz, and RC Reed. Modelling of reaustenitization from the pearlite structure in steel. *Acta materialia*, 46(11):3949–3962, 1998.

[28] Fu-Ren Xiao, Bo Liao, Yi-Yin Shan, Gui-Ying Qiao, Yong Zhong, Chunling Zhang, and Ke Yang. Challenge of mechanical properties of an acicular ferrite pipeline steel. *Materials Science and Engineering: A*, 431(1):41–52, 2006.

[29] JM Gregg and HKDH Bhadeshia. Titanium-rich mineral phases and the nucleation of bainite. *Metallurgical and Materials Transactions A*, 25(8): 1603–1611, 1994.

[30] SS Babu and HKDH Bhadeshia. Stress and the acicular ferrite transformation. *Materials Science and Engineering: A*, 156(1):1–9, 1992.

[31] M Diaz-Fuentes, A Iza-Mendia, and I Gutierrez. Analysis of different acicular ferrite microstructures in low-carbon steels by electron backscattered diffraction. study of their toughness behavior. *Metallurgical and Materials Transactions A*, 34(11):2505–2516, 2003.

[32] Ming-Chun Zhao, Ke Yang, Fu-Ren Xiao, and Yi-Yin Shan. Continuous cooling transformation of undeformed and deformed low carbon pipeline steels. *Materials Science and Engineering: A*, 355(1):126–136, 2003.

[33] Yong Zhong, Yiyin Shan, Furen Xiao, and Ke Yang. Effect of toughness on low cycle fatigue behavior of pipeline steels. *Materials Letters*, 59(14): 1780–1784, 2005.

[34] AP Coldren and JL Mihelich. Acicular ferrite hsla steels for line pipe. *Metal Science and Heat Treatment*, 19(7):559–572, 1977.

[35] Zhenghua Tang and Waldo Stumpf. The role of molybdenum additions and prior deformation on acicular ferrite formation in microalloyed nb–ti low-carbon line-pipe steels. *Materials Characterization*, 59(6):717–728, 2008.

[36] LE Collins, MJ Godden, and JD Boyd. Microstructures of linepipe steels. *Canadian Metallurgical Quarterly*, 22(2):169–179, 1983.

[37] EA Wilson. The $\gamma \rightarrow \alpha$ transformation in low carbon irons. *ISIJ international*, 34(8):615–630, 1994.

[38] Farzad Mohammadi, Faysal Fayez Eliyan, and Akram Alfantazi. Corrosion of simulated weld haz of api x-80 pipeline steel. *Corrosion Science*, 63: 323–333, 2012.

[39] The Welding Institute. Hardness testing. URL `http://www.twi-global.com/technical-knowledge/job-knowledge/hardness-testing-part-1-074/`.

[40] R Blondeau, Ph Maynier, J Dollet, and B Viellard-Baron. Heat treatment'76. *London, Metals Soc*, page 189, 1976.

[41] Tadashi Kasuya, Nobutaka Yurioka, and Makoto Okumura. Methods for predicting maximum hardness of heat-affected zone and selecting necessary preheat temperature for steel welding. *Nippon Steel Technical Report*, pages 7–14, 1995.

[42] D Nolan, Zoran Sterjovski, and D Dunne. Hardness prediction models based on haz simulation for in-service welded pipeline steels. *Science and Technology of Welding & Joining*, 10(6):681–694, 2005.

[43] SH Hashemi. Strength–hardness statistical correlation in api x65 steel. *Materials Science and Engineering: A*, 528(3):1648–1655, 2011.

[44] Nobutaka Yurioka. Physical metallurgy of steel weldability. *ISIJ international*, 41(6):566–570, 2001.

[45] NPTEL. URL `http://nptel.ac.in/courses/112101005/modules/lec4-3/1.3.html`.

[46] CL Davis and JE King. Cleavage initiation in the intercritically reheated coarse-grained heat-affected zone: Part i. fractographic evidence. *Metallurgical and materials transactions A*, 25(3):563–573, 1994.

[47] Jun Hu, Lin-Xiu Du, Jian-Jun Wang, Hui Xie, Cai-Ru Gao, and RDK Misra. High toughness in the intercritically reheated coarse-grained (icrcg) heat-affected zone (haz) of low carbon microalloyed steel. *Materials Science and Engineering: A*, 590:323–328, 2014.

[48] Chaowen Li, Yong Wang, and Yuhua Chen. Influence of peak temperature during in-service welding of api x70 pipeline steels on microstructure and fracture energy of the reheated coarse grain heat-affected zones. *Journal of materials science*, 46(19):6424–6431, 2011.

[49] M Shome, OP Gupta, and ON Mohanty. Effect of simulated thermal cycles on the microstructure of the heat-affected zone in hsla-80 and hsla-100 steel plates. *Metallurgical and Materials Transactions A*, 35(3):985–996, 2004.

[50] JLM Andia, Luís Felipe Guimarães de Souza, and IS Bott. Microstructural and mechanical properties of the intercritically reheated coarse grained heat affected zone (iccghaz) of an api 5l x80 pipeline steel. In *Materials Science Forum*, volume 783, pages 657–662. Trans Tech Publ, 2014.

[51] WJ Poole, M Militzer, and T Garcin. An integrated model to predict microstructure and mechanical properties in the heat affected zone for x80 linepipe. In *2012 9th International Pipeline Conference*, pages 301–306. American Society of Mechanical Engineers, 2012.

[52] Zhixiong Zhu, Lenka Kuzmikova, Huijun Li, and Frank Barbaro. The effect of chemical composition on microstructure and properties of intercritically reheated coarse-grained heat-affected zone in x70 steels. *Metallurgical and Materials Transactions B*, 45:229–235, 2014.

[53] Degala Venkata Kiran, Dae-Won Cho, Hee-Keun Lee, Chung Yun Kang, and Suck-Joo Na. A study on the quality of two-wire tandem submerged arc welds under iso-heat input conditions. *The International Journal of Advanced Manufacturing Technology*, pages 1–10, 2014.

[54] W Zhang, JW Elmer, and T DebRoy. Modeling and real time mapping of phases during gta welding of 1005 steel. *Materials Science and Engineering: A*, 333(1):320–335, 2002.

[55] Dean Deng and Hidekazu Murakawa. Numerical simulation of temperature field and residual stress in multi-pass welds in stainless steel pipe and comparison with experimental measurements. *Computational materials science*, 37(3):269–277, 2006.

[56] Yang You, Chengjia Shang, Liang Chen, and Sundaresa Subramanian. Investigation on the crystallography of the transformation products of reverted austenite in intercritically reheated coarse grained heat affected zone. *Materials & Design*, 43:485–491, 2013.

[57] E Bonnevie, G Ferriere, A Ikhlef, D Kaplan, and JM Orain. Morphological aspects of martensite–austenite constituents in intercritical and coarse grain heat affected zones of structural steels. *Materials Science and Engineering: A*, 385(1):352–358, 2004.

[58] Peyman Mohseni, Jan Ketil Solberg, Morten Karlsen, Odd Magne Akselsen, and Erling Østby. Investigation of mechanism of cleavage fracture initiation in intercritically coarse grained heat affected zone of hsla steel. *Materials Science and Technology*, 28(11):1261–1268, 2012.

[59] Xueda Li, Xiaoping Ma, SV Subramanian, Chengjia Shang, and RDK Misra. Influence of prior austenite grain size on martensite–austenite constituent and toughness in the heat affected zone of 700mpa high strength linepipe steel. *Materials Science and Engineering: A*, 616:141–147, 2014.

[60] Frank S Lepera. Improved etching technique for the determination of percent martensite in high-strength dual-phase steels. *Metallography*, 12(3): 263–268, 1979.

[61] Furen Xiao, Bo Liao, Deliang Ren, Yiyin Shan, and Ke Yang. Acicular ferritic microstructure of a low-carbon mn–mo–nb microalloyed pipeline steel. *Materials Characterization*, 54(4):305–314, 2005.

[62] Zhi-min Zhang, C., Qing-wu Cai, Wei Yu X, Li Xiao-lin, and Li-dong Wang. Continuous cooling transformation behavior and kinetic models of transformations for an ultra-low carbon bainitic steel. *Journal of Iron and Steel Research, International*, 19(12):73–78, 2012.

[63] Ying-Qiao Zhang, Han-Qian Zhang, Jin-Fu Li, and Wei-Ming Liu. Effect of heat input on microstructure and toughness of coarse grain heat affected

zone in nb microalloyed hsla steels. *Journal of Iron and Steel Research, International*, 16(5):73–80, 2009.

[64] Xiangwei Kong and Chunlin Qiu. Continuous cooling bainite transformation characteristics of a low carbon microalloyed steel under the simulated welding thermal cycle process. *Journal of Materials Science & Technology*, 29(5):446–450, 2013.

[65] YQ Zhang, HQ Zhang, WM Liu, and H Hou. Effects of nb on microstructure and continuous cooling transformation of coarse grain heat-affected zone in 610mpa class high-strength low-alloy structural steels. *Materials Science and Engineering: A*, 499(1):182–186, 2009.

[66] H_J Jun, JS Kang, DH Seo, KB Kang, and CG Park. Effects of deformation and boron on microstructure and continuous cooling transformation in low carbon hsla steels. *Materials Science and Engineering: A*, 422(1):157–162, 2006.

[67] Zhixiong Zhu, Lenka Kuzmikova, Huijun Li, and Frank Barbaro. Effect of inter-critically reheating temperature on microstructure and properties of simulated inter-critically reheated coarse grained heat affected zone in x70 steel. *Materials Science and Engineering: A*, 605:8–13, 2014.

[68] Y Li, DN Crowther, MJW Green, PS Mitchell, and TN Baker. The effect of vanadium and niobium on the properties and microstructure of the intercritically reheated coarse grained heat affected zone in low carbon microalloyed steels. *ISIJ international*, 41(1):46–55, 2001.

[69] YT Chen, AM Guo, LX Wu, J Zeng, and PH Li. Microstructure and mechanical property development in the simulated heat affected zone of v treated hsla steels. *Acta Metallurgica Sinica (English Letters)*, 19(1):57–67, 2006.

[70] Astrid Lambert-Perlade, Anne-Françoise Gourgues, Jacques Besson, T Sturel, and André Pineau. Mechanisms and modeling of cleavage fracture in simulated heat-affected zone microstructures of a high-strength low alloy steel. *Metallurgical and Materials Transactions A*, 35(13):1039–1053, 2004.

[71] Liangyun Lan, Chunlin Qiu, Hongyu Song, and Dewen Zhao. Correlation of martensite–austenite constituent and cleavage crack initiation in welding heat affected zone of low carbon bainitic steel. *Materials Letters*, 125:86–88, 2014.

[72] Y Li and TN Baker. Effect of morphology of martensite–austenite phase on fracture of weld heat affected zone in vanadium and niobium microalloyed steels. *Materials Science and Technology*, 26(9):1029–1040, 2010.

[73] Kenichi Yokoyama and Michihiko Nagumo. Brittle fracture initiation associated with the strain localization in a heat-affected zone of a low carbon steel. *Metallurgical and Materials Transactions A*, 29(2):551–558, 1998.

[74] Liangyun Lan, Chunlin Qiu, Dewen Zhao, Xiuhua Gao, and Linxiu Du. Microstructural characteristics and toughness of the simulated coarse grained heat affected zone of high strength low carbon bainitic steel. *Materials Science and Engineering: A*, 529:192–200, 2011.

[75] Kenji Ohya, Jongseop Kim, Ken'ichi Yokoyama, and Michihiko Nagumo. Microstructures relevant to brittle fracture initiation at the heat-affected zone of weldment of a low carbon steel. *Metallurgical and Materials Transactions A*, 27(9):2574–2582, 1996.

[76] S Moeinifar, AH Kokabi, and HR Madaah Hosseini. Influence of peak temperature during simulation and real thermal cycles on microstructure and fracture properties of the reheated zones. *Materials & Design*, 31(6): 2948–2955, 2010.

[77] Elena Pereloma and David V Edmonds. *Phase Transformations in Steels: Diffusionless transformations, high strength steels, modelling and advanced analytical techniques*, volume 2. Elsevier, 2012.

[78] Adam J Schwartz, Mukul Kumar, Brent L Adams, and David P Field. *Electron backscatter diffraction in materials science*, volume 2. Springer, 2009.

[79] Roumen Petrov, Leo Kestens, Anna Wasilkowska, and Yvan Houbaert. Microstructure and texture of a lightly deformed trip-assisted steel characterized by means of the ebsd technique. *Materials Science and Engineering: A*, 447(1):285–297, 2007.

[80] Marijke De Meyer, Leo Kestens, and BC De Cooman. Texture development in cold rolled and annealed c-mn-si and c-mn-al-si trip steels. *Materials science and technology*, 17(11):1353–1359, 2001.

[81] Jinghui Wu, Peter J Wray, Calixto I Garcia, Mingjian Hua, and Anthony J DeArdo. Image quality analysis: a new method of characterizing microstructures. *ISIJ international*, 45(2):254–262, 2005.

[82] *Technical Note - EBSD, Confidence Index*. EDAX, November 2013. URL `http://www.edax.com/download/Confidence_Index_LR.pdf`.

[83] ASTM International. E384 11 standard test method for knoop and vickers hardness of materials, March 2012.

[84] Harry Chandler et al. *Hardness testing*. ASM international, 1999.

[85] X Yue, JC Lippold, BT Alexandrov, and SS Babu. Continuous cooling transformation behavior in the cghaz of naval steels. *Welding journal*, 91 (3), 2012.

[86] Oystein Grong. Metallurgical modelling of welding. *Institute of Materials, 1 Carlton House Terrace, London, SW 1 Y 5 DB, UK, 1997. 605*, 1997.

[87] Jennifer M Reichert, Thomas Garcin, Matthias Militzer, and Warren J Poole. Formation of martensite/austenite (m/a) in x80 linepipe steel. In *2012 9th International Pipeline Conference*, pages 483–489. American Society of Mechanical Engineers, 2012.

[88] Ito Yoshinori and Bessyo Kiyoshi. Cracking parameter of high strength steels related to heat affected zone cracking. *QUARTERLY JOURNAL OF THE JAPAN WELDING SOCIETY*, 37(9):983–991, 1968.

[89] RB Lazor and BA Graville. Effect of microalloying on weld cracking in low carbon steels. *Pipeline and energy plant piping: design and technology*, page 247, 1980.

[90] Stanislaw Zajac, Volker Schwinn, and KH Tacke. Characterisation and quantification of complex bainitic microstructures in high and ultra-high strength linepipe steels. In *Materials Science Forum*, volume 500, pages 387–394. Trans Tech Publ, 2005.

Appendices

Appendix A

Measured Hardness

Table A.1: Hardness in HV0.5 measured for all gleeble samples and the base metal.

Temperature profile	Steel A	Steel B	Steel C	Steel D
LHI-810	226 ± 5	211 ± 5	256 ± 5	228 ± 6
LHI-860	219 ± 4	208 ± 4	244 ± 5	230 ± 7
IHI-810	220 ± 5	206 ± 4	243 ± 4	220 ± 6
IHI-860	214 ± 5	194 ± 4	226 ± 6	216 ± 5
HHI-810	206 ± 7	187 ± 6	225 ± 8	227 ± 5
HHI-860	202 ± 5	184 ± 5	217 ± 4	195 ± 6
LHI	232 ± 6	211 ± 3	356 ± 13	261 ± 10
IHI	233 ± 6	219 ± 6	303 ± 9	243 ± 6
HHI	221 ± 5	207 ± 4	282 ± 12	235 ± 5
BM-Mid	200 ± 4	181 ± 4	225 ± 6	204 ± 7
BM-Edge	220 ± 3	207 ± 5	207 ± 6	246 ± 8

Appendix B

Lepera's etchant quantification

Table B.1: Lepera results threshold 0.1 μm^2

Sample	Size (μm^2)	Fraction (%)	Circularity	Aspect ratio
A-LHI-810	1.296 ± 0.102	5.548 ± 1.023	0.597 ± 0.013	1.999 ± 0.084
A-LHI-860	0.582 ± 0.104	3.436 ± 0.681	0.488 ± 0.039	2.155 ± 0.048
A-IHI-810	1.730 ± 0.340	6.448 ± 0.829	0.573 ± 0.017	1.981 ± 0.053
A-IHI-860	0.587 ± 0.132	3.121 ± 0.499	0.461 ± 0.034	2.090 ± 0.043
A-HHI-810	0.919 ± 0.225	4.631 ± 0.701	0.509 ± 0.086	2.180 ± 0.072
A-HHI-860	0.907 ± 0.155	1.645 ± 0.164	0.675 ± 0.015	2.183 ± 0.161
B-LHI-810	0,853 ± 0,137	4,224 ± 1,304	0,505 ± 0,035	1,993 ± 0,079
B-LHI-860	0,713 ± 0,076	3,503 ± 0,480	0,388 ± 0,007	2,020 ± 0,033
B-IHI-810	0,991 ± 0,139	3,567 ± 1,063	0,444 ± 0,006	2,047 ± 0,112
B-IHI-860	0,837 ± 0,067	2,488 ± 0,254	0,375 ± 0,013	2,016 ± 0,045
B-HHI-810	1,418 ± 0,184	2,739 ± 0,794	0,374 ± 0,022	1,968 ± 0,100
B-HHI-860	2,193 ± 0,267	3,525 ± 0,760	0,634 ± 0,029	1,929 ± 0,080
C-LHI-810	1,007 ± 0,056	9,727 ± 0,835	0,462 ± 0,049	2,028 ± 0,032
C-LHI-860	0,681 ± 0,030	4,922 ± 1,000	0,408 ± 0,015	2,025 ± 0,038
C-IHI-810	1,027 ± 0,120	6,736 ± 0,756	0,409 ± 0,022	1,961 ± 0,028
C-IHI-860	0,542 ± 0,024	3,284 ± 0,469	0,444 ± 0,009	2,143 ± 0,044
C-HHI-810	0,808 ± 0,112	4,248 ± 0,608	0,408 ± 0,021	2,113 ± 0,079
C-HHI-860	0,848 ± 0,061	3,916 ± 0,308	0,440 ± 0,025	2,117 ± 0,093
D-LHI-810	0,978 ± 0,123	7,410 ± 0,364	0,626 ± 0,023	2,009 ± 0,054
D-LHI-860	0,833 ± 0,080	6,610 ± 0,861	0,461 ± 0,007	2,132 ± 0,053
D-IHI-810	0,818 ± 0,078	3,900 ± 0,665	0,470 ± 0,059	2,105 ± 0,076
D-IHI-860	0,584 ± 0,035	2,570 ± 0,323	0,605 ± 0,014	2,363 ± 0,098
D-HHI-810	0,852 ± 0,120	3,650 ± 0,720	0,560 ± 0,012	2,177 ± 0,026
D-HHI-860	0,954 ± 0,194	3,252 ± 0,958	0,516 ± 0,044	2,158 ± 0,043

Table B.2: Lepera results threshold 1 μm^2

Sample	Size	Volume fraction	Circularity	Aspect ratio
A-LHI-810	3.997 ± 0.575	4.448 ± 0.882	0.404 ± 0.008	2.043 ± 0.084
A-LHI-860	2.134 ± 0.395	1.979 ± 1.157	0.288 ± 0.040	2.366 ± 0.124
A-IHI-810	4.751 ± 0.588	4.641 ± 1.340	0.420 ± 0.014	2.127 ± 0.090
A-IHI-860	2.150 ± 0.099	1.935 ± 0.552	0.275 ± 0.020	2.287 ± 0.105
A-HHI-810	2.638 ± 0.514	1.534 ± 0.543	0.375 ± 0.066	2.281 ± 0.115
A-HHI-860	2.592 ± 0.521	1.120 ± 0.203	0.521 ± 0.024	2.259 ± 0.257
B-LHI-810	2,470 ± 0,421	2,292 ± 0,859	0,334 ± 0,015	2,222 ± 0,143
B-LHI-860	2,036 ± 0,144	1,725 ± 0,500	0,244 ± 0,019	2,347 ± 0,137
B-IHI-810	2,909 ± 0,230	3,100 ± 0,358	0,306 ± 0,015	2,246 ± 0,151
B-IHI-860	2,265 ± 0,133	1,668 ± 0,185	0,245 ± 0,018	2,202 ± 0,105
B-HHI-810	2,265 ± 0,133	1,668 ± 0,185	0,245 ± 0,018	2,202 ± 0,105
B-HHI-860	3,933 ± 0,221	3,743 ± 0,713	0,572 ± 0,007	1,939 ± 0,095
C-LHI-810	2,681 ± 0,313	5,943 ± 1,881	0,315 ± 0,049	2,138 ± 0,048
C-LHI-860	2,260 ± 0,216	3,199 ± 0,884	0,242 ± 0,022	2,124 ± 0,033
C-IHI-810	2,260 ± 0,216	3,199 ± 0,884	0,242 ± 0,022	2,124 ± 0,033
C-IHI-860	2,113 ± 0,077	2,407 ± 0,769	0,269 ± 0,008	2,201 ± 0,060
C-HHI-810	2,638 ± 0,137	3,482 ± 0,549	0,245 ± 0,042	2,080 ± 0,103
C-HHI-860	2,602 ± 0,251	2,825 ± 0,645	0,296 ± 0,026	2,155 ± 0,179
D-LHI-810	3,359 ± 0,277	5,031 ± 0,908	0,397 ± 0,030	2,190 ± 0,105
D-LHI-860	2,551 ± 0,235	5,321 ± 1,327	0,291 ± 0,008	2,345 ± 0,162
D-IHI-810	3,220 ± 0,494	2,954 ± 0,946	0,282 ± 0,041	2,262 ± 0,168
D-IHI-860	2,128 ± 0,203	1,626 ± 0,397	0,375 ± 0,012	2,580 ± 0,154
D-HHI-810	2,923 ± 0,253	2,958 ± 0,858	0,377 ± 0,006	2,287 ± 0,092
D-HHI-860	2,668 ± 0,394	2,333 ± 0,987	0,384 ± 0,039	2,225 ± 0,129

Appendix C

EBSD scans

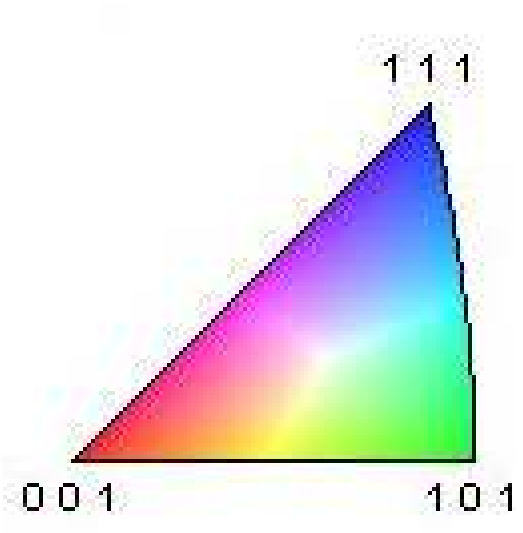

Figure C.1: Colour coding for the inverse pole figure maps.

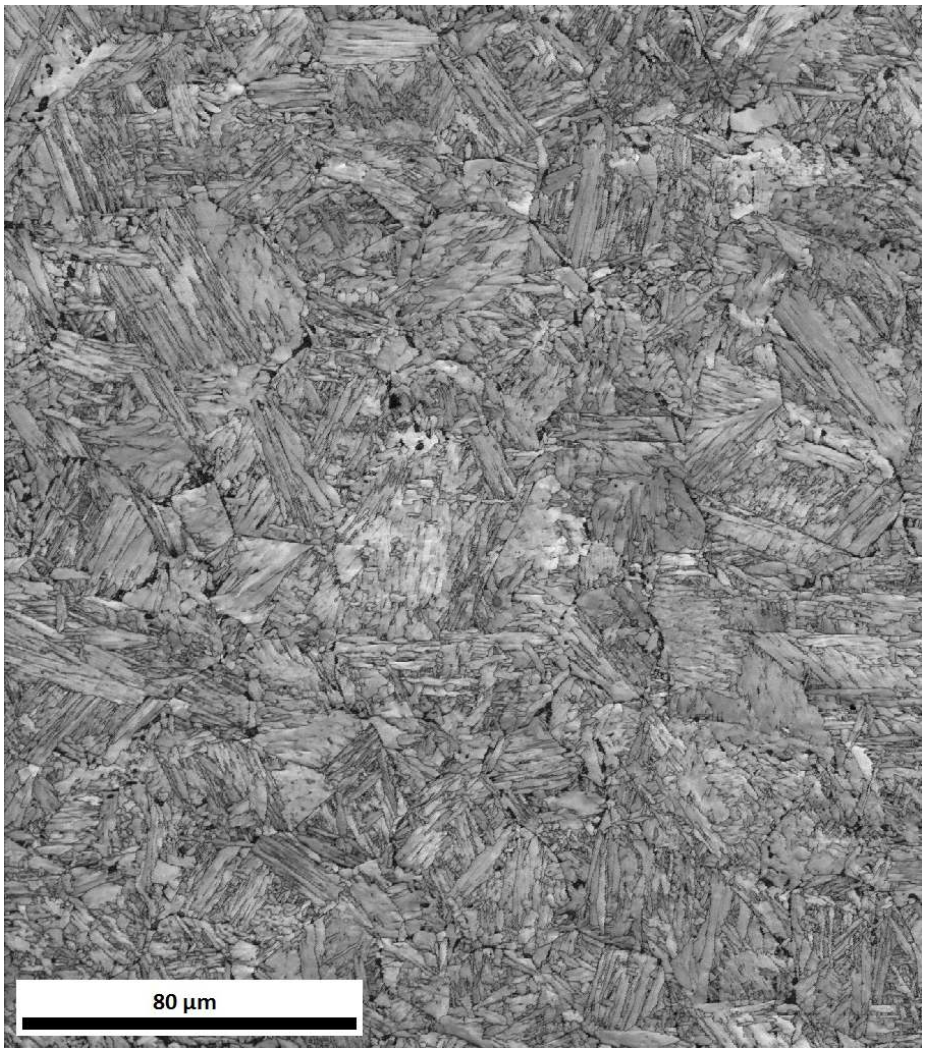

Figure C.2: IQ map of BM-A

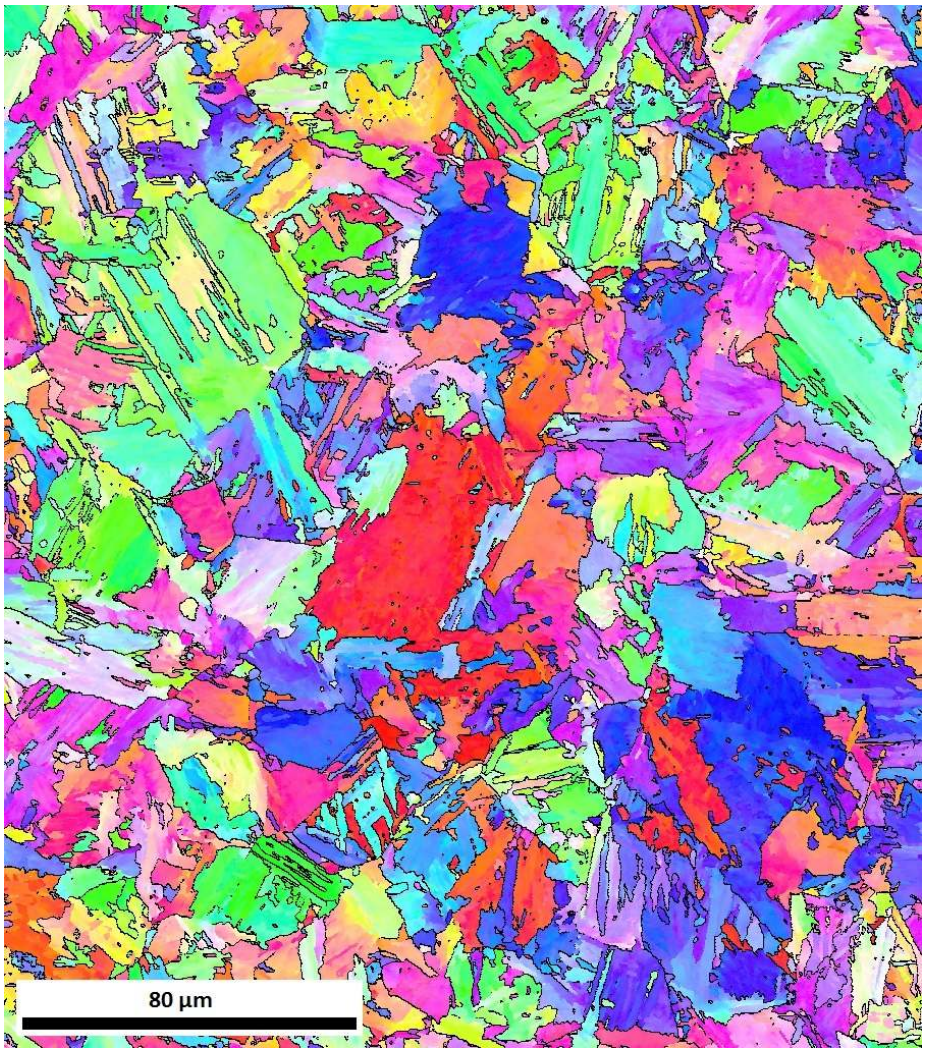

Figure C.3: IPF map of BM-A with the hagb highlighted as black lines. The colour coding can be found at the beginning of appendix C.

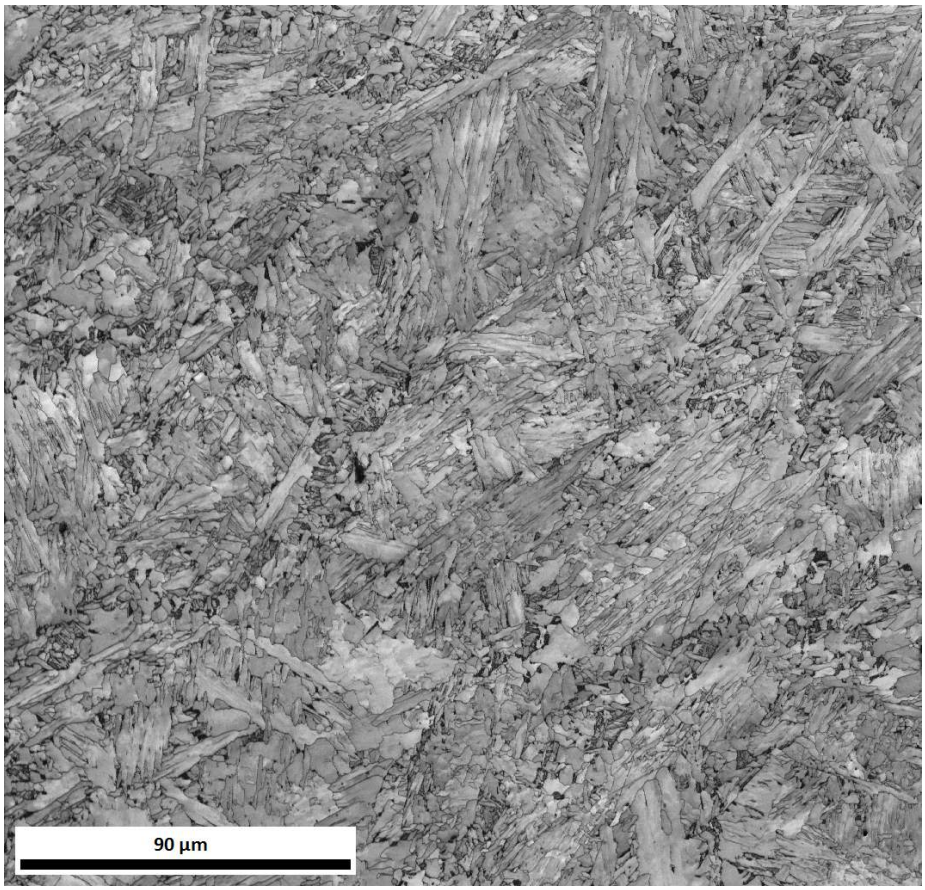

Figure C.4: IQ map of A-LHI-810

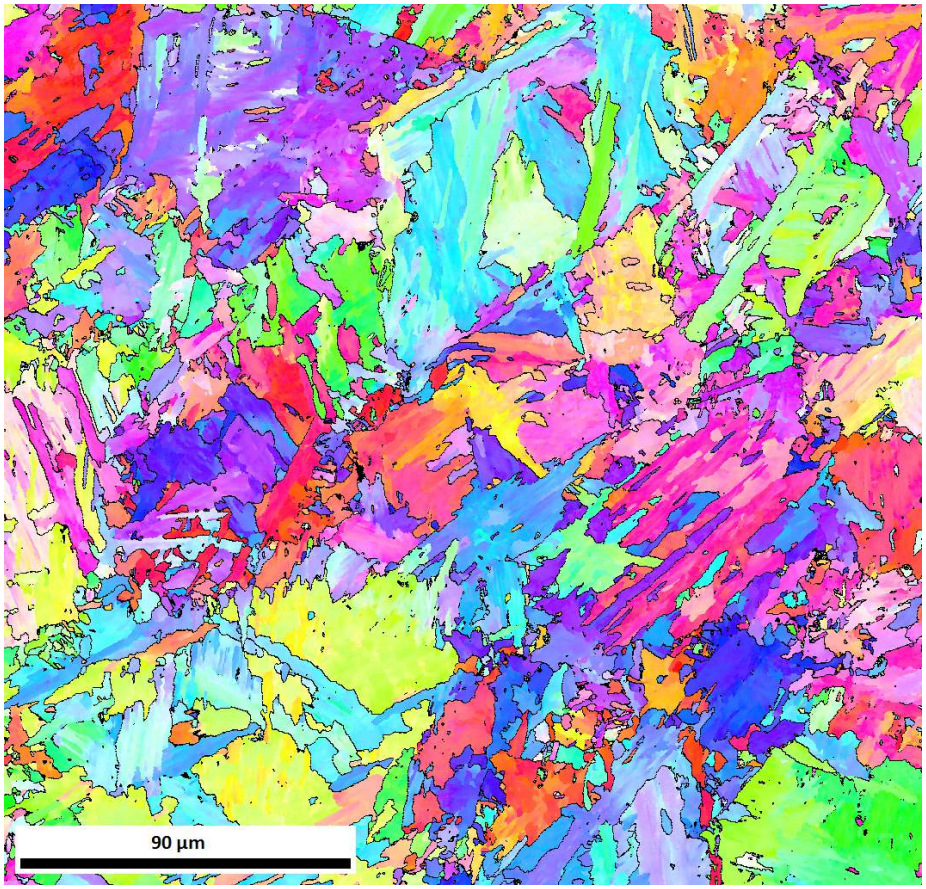

Figure C.5: IPF map of A-LHI-810 with the hagb highlighted as black lines. The colour coding can be found at the beginning of appendix C.

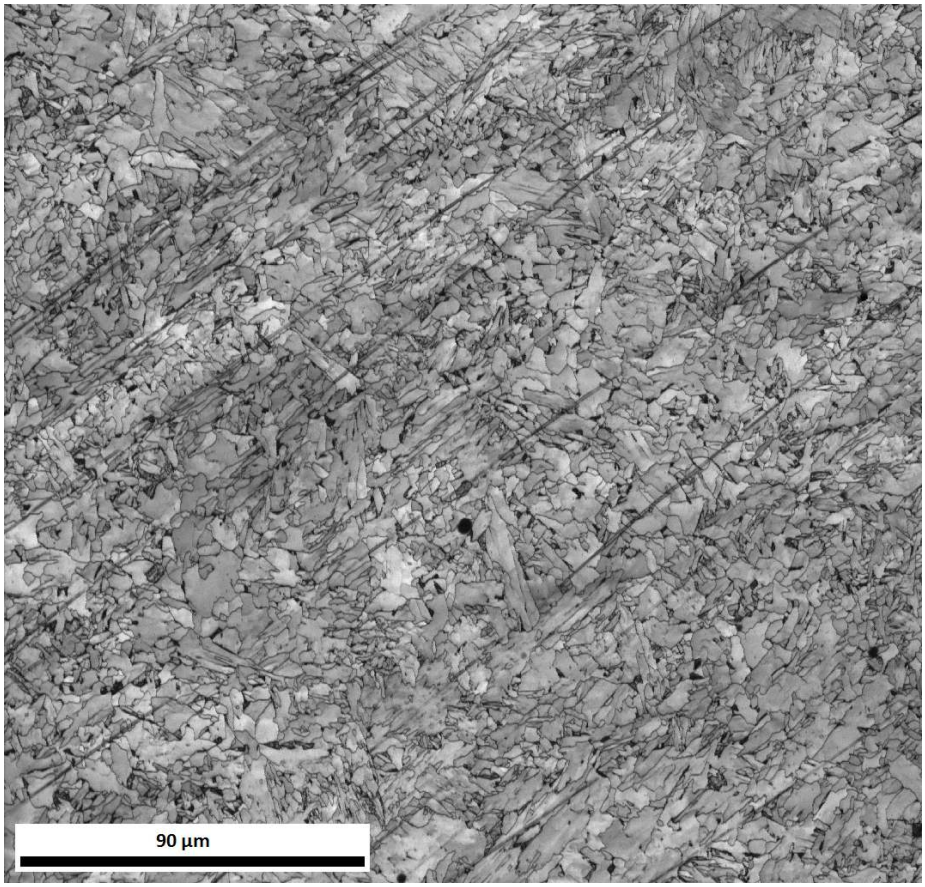

Figure C.6: IQ map of A-LHI-860

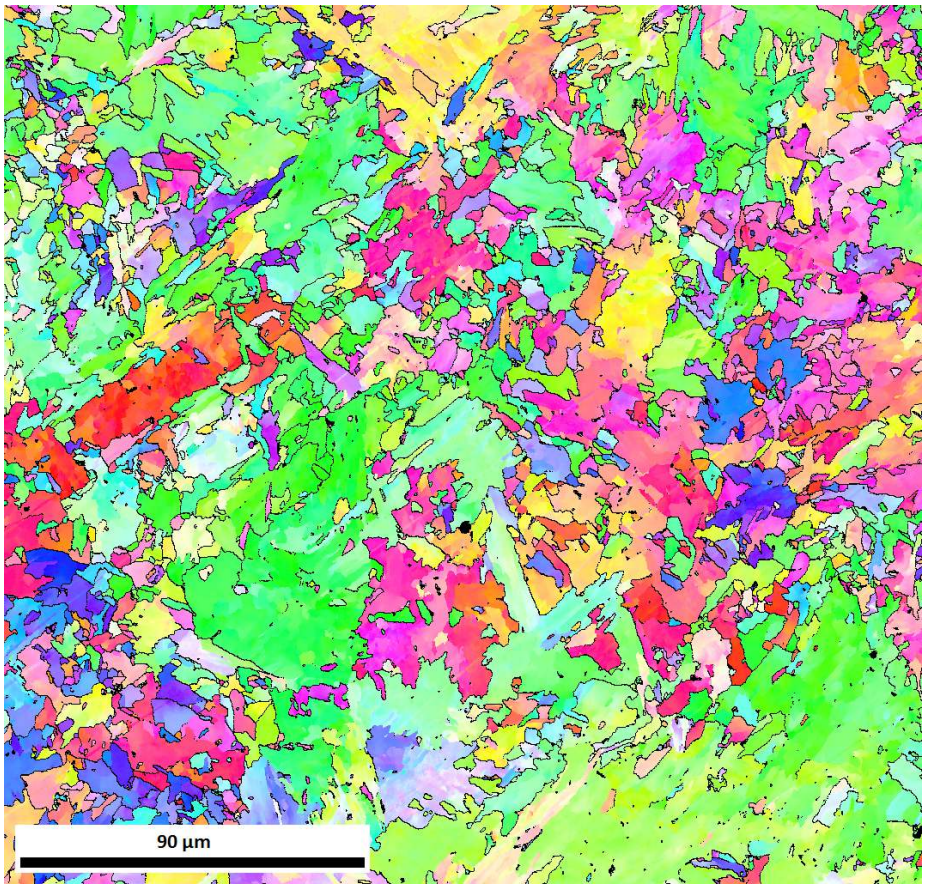

Figure C.7: IPF map of A-LHI-860 with the hagb highlighted as black lines. The colour coding can be found at the beginning of appendix C.

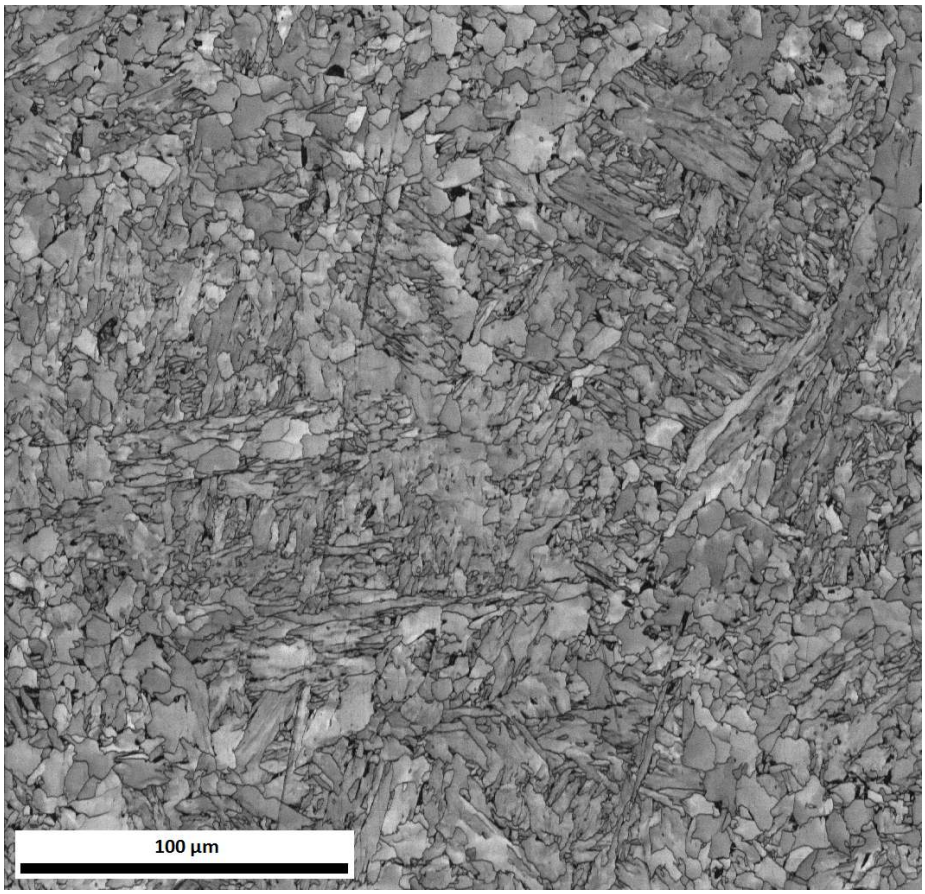

Figure C.8: IQ map of A-HHI-810

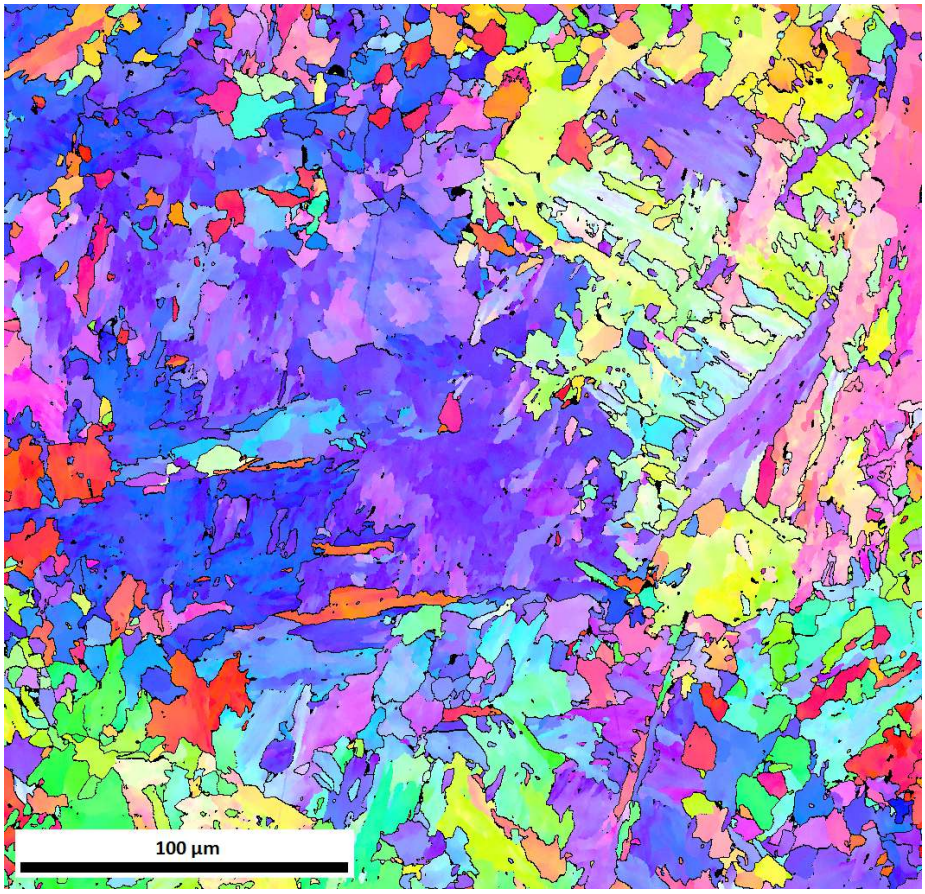

Figure C.9: IPF map of A-HHI-810 with the hagb highlighted as black lines. The colour coding can be found at the beginning of appendix C.

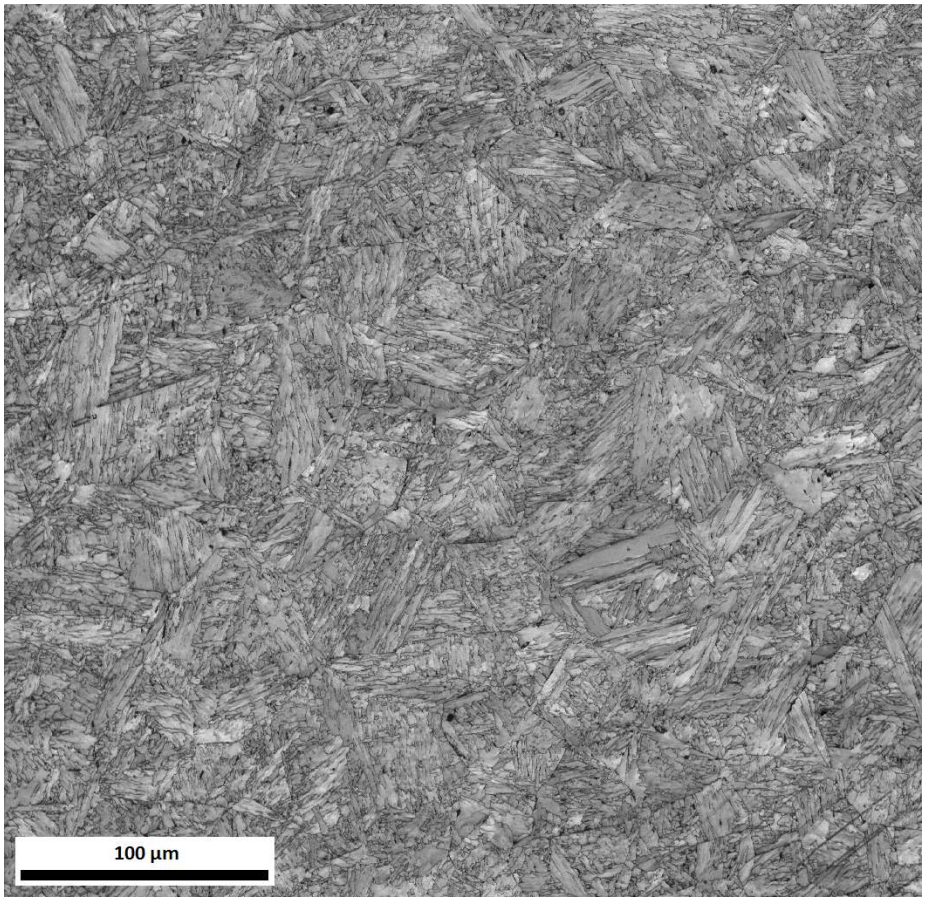

Figure C.10: IQ map of A-HHI

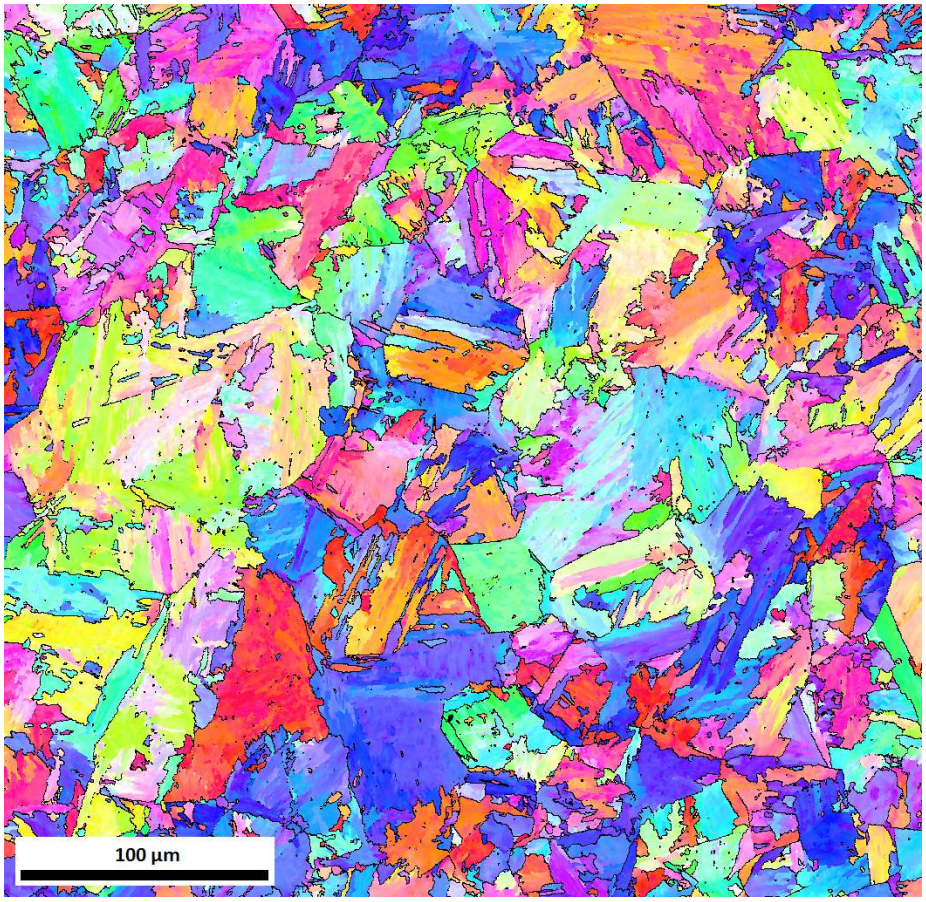

Figure C.11: IPF map of A-HHI with the hagb highlighted as black lines. The colour coding can be found at the beginning of appendix C.

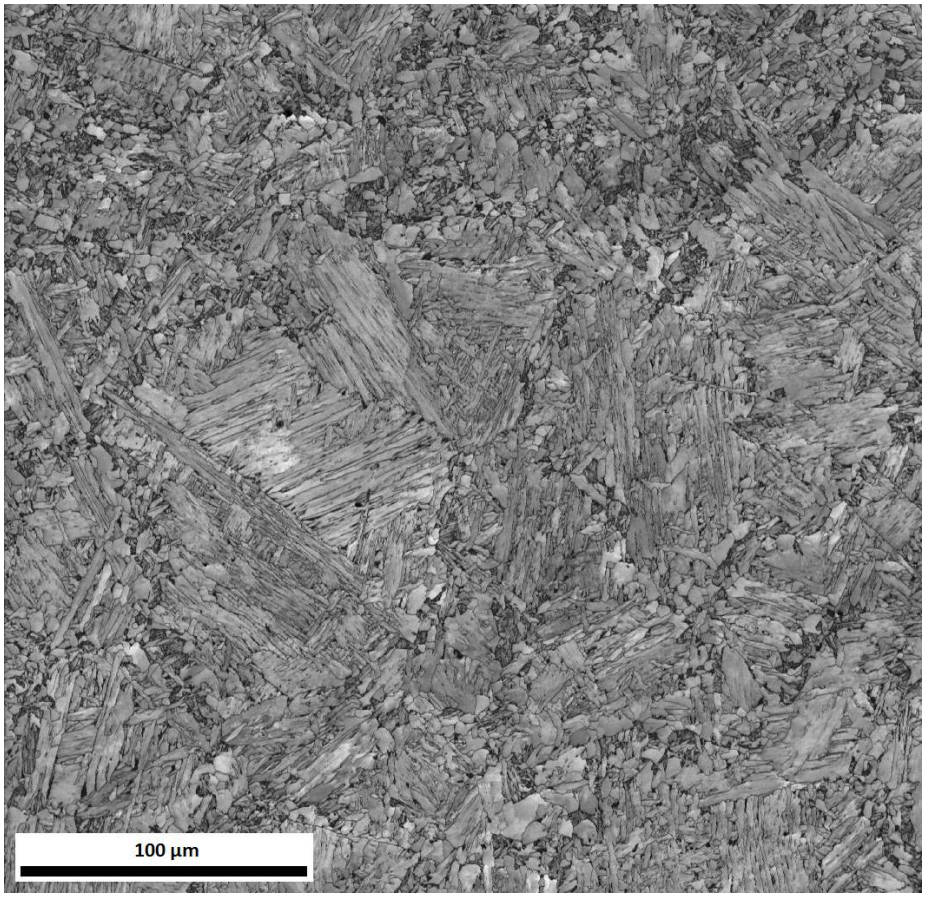

Figure C.12: IQ map of D-LHI-810

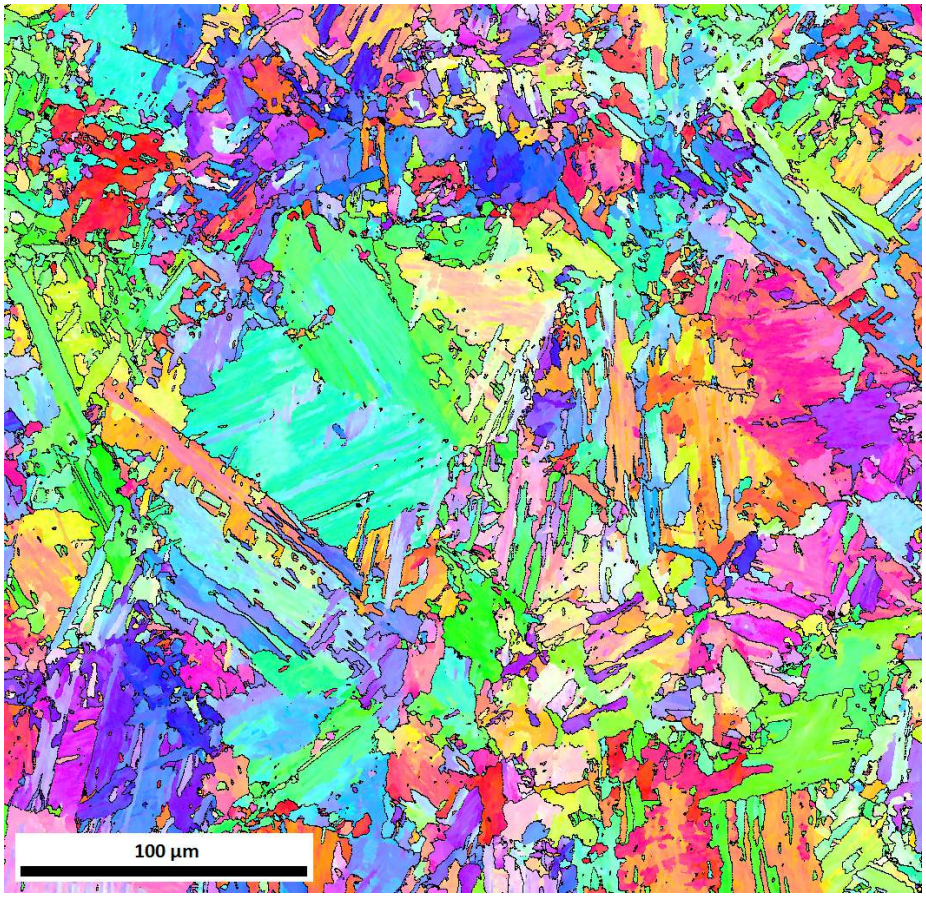

Figure C.13: IPF map of D-LHI-810 with the hagb highlighted as black lines. The colour coding can be found at the beginning of appendix C.

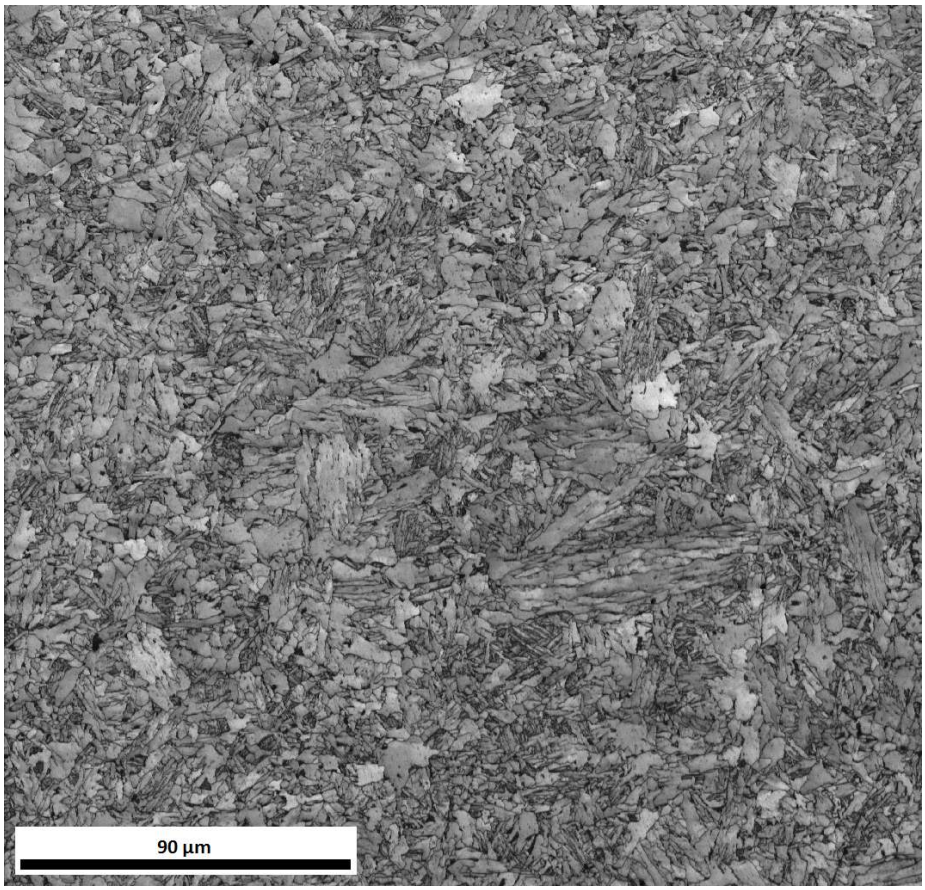

Figure C.14: IQ map of D-LHI-860

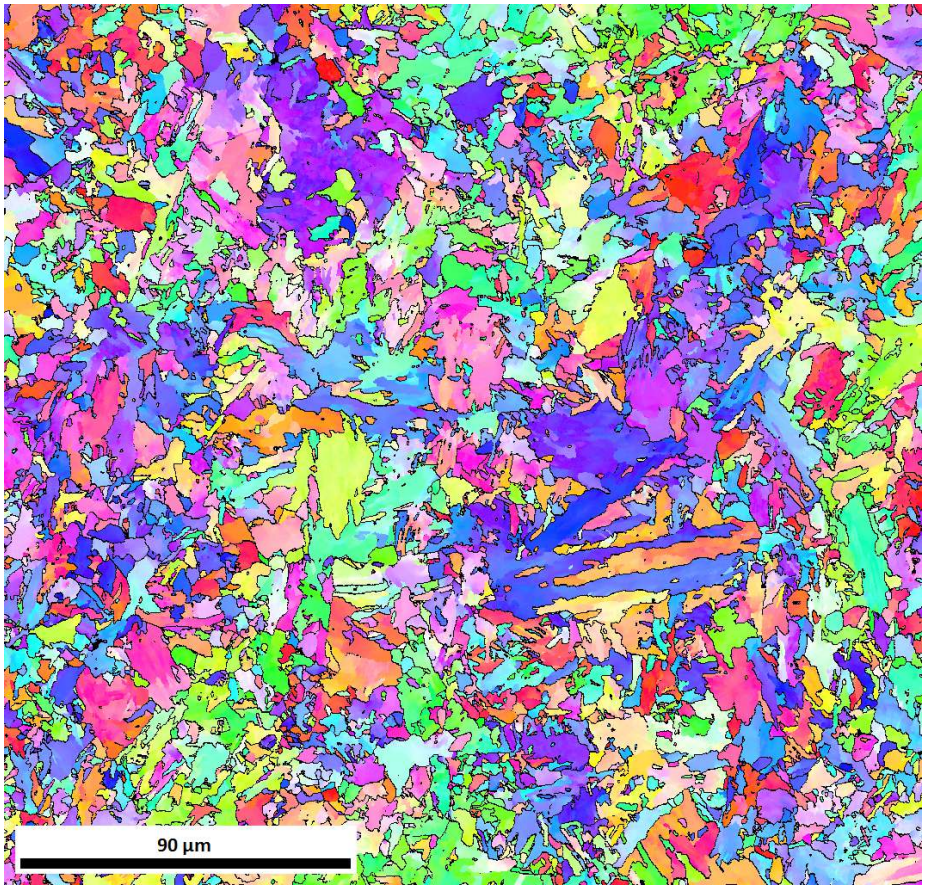

Figure C.15: IPF map of D-LHI-860 with the hagb highlighted as black lines. The colour coding can be found at the beginning of appendix C.